Integrated Environmental Degradation Model for Fe-Ni-Cr Alloys in Irradiated Aqueous Solutions

by

Thomas Todd Pleune

B.S. Nuclear Engineering
University of Illinois, 1995

Submitted to the Department of Nuclear Engineering
in partial fulfillment of the requirements for the degree of

Doctor of Philosophy in Nuclear Engineering
at the
Massachusetts Institute of Technology

September 1999

Author_____
Department of Nuclear Engineering
July 8, 1999

Certified by_____
Ronald G. Ballinger, Sc.D.
Professor of Nuclear Engineering and Materials Science and Engineering
Thesis Supervisor

Certified by_____
Ronald M. Latanision, Ph.D.
Professor of Materials Science and Engineering and Nuclear Engineering
Thesis Reader

Certified by_____
Kenneth C. Russell, Ph.D.
Professor of Materials Science and Engineering and Nuclear Engineering
Thesis Reader

Accepted by_____
Sow-Hsin Chen, Ph.D.
Chairman, Department Committee on Graduate Students

DISCLAIMER NOTICE

The accompanying media item for this thesis is available in the MIT Libraries or Institute Archives.

Thank you.

COMPACT DISC

Integrated Environmental Degradation Model for Fe-Ni-Cr Alloys in Irradiated Aqueous Solutions

by

Thomas Todd Pleune

Submitted to the Department of Nuclear Engineering
on July 8, 1999 in partial fulfillment of the
Requirements for the degree of
Doctor of Philosophy in Nuclear Engineering

Abstract

An integrated model has been developed to evaluate the effect of reactor flux, fluence, and other operating conditions on crack growth rates in austenitic stainless steels in boiling water reactor (BWR) environments. The model evaluates the following in order to account for all factors affecting irradiation assisted stress corrosion cracking.

- water chemistry including radiolysis and hydrogen injection
- radiation induced segregation of the metal
- radiation hardening of the metal
- crack tip strain rate of a growing crack
- dissolution rate at the crack tip following passive film rupture

The results of each of these models are combined to determine the crack advance rate for the given conditions.

Environmentally assisted cracking (EAC) is a phenomenon where a combination of aggressive environment, susceptible material, and significant tensile stress result in accelerated degradation, including stress corrosion cracking (SCC), and hydrogen embrittlement. The EAC model is based on first principles electrochemistry and physical metallurgy. The effect of neutron and gamma radiation dose is included so that irradiation assisted stress corrosion cracking can be studied. By integrating the bulk chemistry with crack tip processes, the crack growth behavior of an aqueous system can be completely characterized. The model integrates chemistry and mechanical behavior to allow the study of EAC in general. EAC phenomena of interest include anodically driven stress corrosion cracking as well as cathodically driven hydrogen embrittlement.

The model is able to predict measured data in the literature with good accuracy and precision. It predicts the effects of dose-rate and accumulated dose on stress corrosion cracking in BWRs. This model contributes to the field of crack growth modeling by creating a complete picture including all the major factors effecting crack growth in irradiated systems.

Thesis Supervisor: Ronald G. Ballinger

Title: Professor of Nuclear Engineering and Materials Science and Engineering

Acknowledgements

I would like to express my sincere appreciation to Professor Ron Ballinger for his guidance, ideas, and support throughout this project. This model could not have been completed without his vision of what it must accomplish. I would like to thank Professor Ron Latanision for being my thesis reader. His insights along the way provided fresh perspective and objectivity. My second reader, Ken Russell, stepped in late to save my chosen defense date. My thesis is better for having added him to my committee.

Because the Department of Energy funded me for all four years, I had the flexibility to select my project, my advisor, and my group. After concluding that metallurgy and corrosion were the areas that interested me most, I set about finding a project. While Professor Ballinger's large choice of projects and enthusiasm were important factors for my choice of research groups, another important factor was the large group of excellent students with whom I would be working. I would like to thank Mark van der Helm, Dave Grundy, Dave Grover, John Chun, and Seung Kee Min who were indispensible with advice on programming, materials science, and graduate school in general. I would like to thank Hiu Au, Doug Kalinouski, Rachelle Hughes, Heather MacLean, Pete Stahl, Barbara Keesler, Bruce Brisson, Seung Jegarl, Celine Fauchon, Anthony Châtelain, Tammy Galen and others for everything from ordinary conversations to life advice. I would like to thank Steve Boerigter for the use of his RIS model and his advice about engagement ring shopping.

Thanks to Sandy Wolfson, my roommate for three years, for sharing his advice, his ideas, and his friends (John Johnson).

My family deserves special thanks for supporting me in this endeavor. Although my plans and goals change almost annually, my family was there to support each decision. Most of all I would like to thank my wife, Heather. While her effort in skillfully editing this manuscript without depth of knowledge in the field was greatly appreciated, her support was even more valuable. Her support from afar, as she completed her schooling was wonderful, but having her here this year has meant the world to me. Without her encouragement and understanding, it is hard to imagine this thesis coming to fruition.

This research was performed under appointment to the U.S. Department of Energy Nuclear Engineering and Health Physics Fellowship Program sponsored by DOE's Office of Nuclear Energy, Science and Technology.

Table of Contents

List of Figures

List of Tables

An integrated model has been developed to evaluate the effect of reactor flux, fluence, and other operating conditions on crack growth rates in austenitic stainless steels in boiling water reactor (BWR) environments. The following are the contributions made here and described in this thesis.

- A fully integrated crack growth model which incorporates the effects of irradiation on the physical and chemical properties of both the metal and reactor coolant.
- Accounting for both anodic and cathodic crack tip processes.
- A radiation hardening model for predicting the long-term effect of radiation on performance of austenitic alloys.
- A correlation between the grain boundary chromium profile and the equivalent EPR value for which the cracking susceptibility is equal to a degree of thermal sensitization.
- Use of a complete deterministic derivation of the slip dissolution/ film rupture model originally developed by Ford and Andresen [1.7, 1.13].
- A Visual Basic graphical user interface.

1. Introduction

Materials developed for high technology applications are increasingly resistant to general corrosion in the environments in which they operate. As resistance to general corrosion increases, these materials often suffer degradation due to localized corrosion. This

is significant in the nuclear power industry. The increase in susceptibility to localized corrosion is exacerbated by higher stresses in engineering materials. This is a result of residual stress from increased use of welding and high operating stress.

Environmentally assisted cracking (EAC) is the most problematic form of localized corrosion. EAC is any phenomenon where a combination of environment, material, and tensile stress result in accelerated degradation, including stress corrosion cracking (SCC), hydrogen embrittlement, and corrosion fatigue. The goal of this research is to develop an integrated EAC model. The primary dependant variable in the model will be the environmentally assisted crack growth rate. Independent variables include chemical, mechanical, and system properties.

As integration is the key factor in the development of the following model, it will be referred to as the Integrated Environmental Degradation Model (IEDM) throughout this work. While some researchers continue to search for one mechanism capable of describing EAC in all situations, most others agree that several separate mechanisms are necessary to explain EAC. Therefore, the IEDM accounts for both anodically driven stress corrosion cracking and cathodically driven hydrogen embrittlement. The IEDM integrates chemistry and mechanical behavior to allow the study of EAC in general. A characterization of crack tip strain is included to properly define the state of stress of the crack. The effect of neutron and gamma radiation dose is completely integrated into the IEDM as well. This includes a model for the radiolysis effect on reactor coolant chemistry, a model for radiation induced segregation of Fe-Ni-Cr alloys and a radiation hardening model.

The following three tasks are accomplished in this dissertation:

- ❖ Development of an integrated crack growth model that incorporates both anodic and cathodic processes at the crack tip and in the bulk system.
- ❖ Coupling the necessary models and correlations to the crack growth model to completely characterize the effect of radiation and chemistry.
- ❖ Utilization of Visual Basic for creation of a graphical user interface

The primary application for this model is EAC in light water reactor systems. The input required for the model includes the following:

- ❖ Thermal-hydraulic data such as flow rate, temperature and pressure
- ❖ Chemical reaction sets for radiolysis products and other present species
- ❖ Reactor power and dose distributions
- ❖ Reactor component dimensions
- ❖ Stress/strain conditions and sensitization data for reactor components

The radiation chemistry analysis loop model by Chun [1.1] and Grover [1.2] has been updated and is incorporated into the IEDM to model coolant chemistry and radiolysis. A radiation induced segregation model by Boerigter has been updated and is used to model the effect of radiation on the sensitization behavior of the metal [1.3]. The output of this model is profile of chromium concentration across the grain boundary. The determination of the degree of sensitization (DOS) by microscopic analysis of the minimum chromium concentration along the grain boundaries is not a simple task. Therefore, a standard method has been designed for nondestructive testing to determine the degree of sensitization. This method is the electrochemical potentiostatic reactivation (EPR) technique [1.4]. In an EPR test, a sample is corroded during a potential scan and the integrated current is measured. This current is then compared to the grain boundary

area to determine the rate of corrosion along the grain boundaries [1.5,1.6]. Because the grain boundary sensitization of most samples discussed in the literature is given as the EPR value, an equation converting the radiation induced segregation profile into an EPR value was developed for this model.

1.1. Crack Advance Mechanisms

The phenomena of environmentally assisted cracking range from those for which mechanical effects dominate to those that are dominated by electrochemical effects. However, EAC can be broadly divided into two types of phenomena: those for which the cathodic crack tip process is responsible for crack advance and those for which the anodic crack tip process is responsible. While the anodic or cathodic process may be ***responsible*** for crack advance, either process may ***control*** the rate of advance. In the local crack tip environment, it is possible for both processes to occur simultaneously. In this section, the cathodic and anodic mechanisms of crack advance is discussed.

1.1.1. Cathodically Driven Environmentally Assisted Degradation

Hydrogen embrittlement is significant at relatively low temperatures in cathodically polarized metals. The requirements for the hydrogen embrittlement mechanism are the following [1.7]:

- A reducible species that contains hydrogen must be present at the crack tip and have access to the metal.
- Hydrogen must be reduced at the crack tip and this reaction must be balanced by an oxidation reaction. The oxidation process need not occur at or near the crack tip.

- ❖ Hydrogen must gain access to the material and be able to migrate to a critical region. This process is a strong function of the properties of the surface film and the concentration of hydrogen and other species in the crack.

The role of hydrogen as an embrittling agent is complex. Consequently, several mechanisms by which hydrogen damage might occur have been suggested. The following are a few of these mechanisms. One mechanism for hydrogen embrittlement involves the reaction of hydrogen atoms with dislocations, voids, or the stress field at the crack tip to decrease the ductility of the metal [1.7]. A second mechanism suggests that the build-up of gas pressure at vacancies and dislocations in the plastic zone at the crack tip results in fracture [1.7]. These accumulating gases can include diatomic hydrogen, methane, and hydrogen sulfide. Another proposal is the decohesion mechanism of Parkins [1.8]. Here, electrons donated from dissolved hydrogen atoms enter the incompletely filled d-bond of transition metals. This increased electron density acts to increase the interatomic spacing of the lattice, which reduces the cohesive strength of the metal. At any location within the metal lattice where hydrogen concentrates, the cohesive strength is reduced causing the metal to become more susceptible to fracture.

1.1.2. Anodic Dissolution Mechanisms

At the other end of the spectrum from hydrogen embrittlement are those mechanisms that result from anodic dissolution of the metal at the crack tip. Stress corrosion cracking can be either intergranular or transgranular. In intergranular stress corrosion cracking (IGSCC), electrochemical heterogeneity results from depletion and/or precipitation of certain species at grain boundaries. This heterogeneity generates a galvanic cell that results in anodic dissolution of the material at the grain boundaries. Additives and

impurities in the metal such as copper, tin, antimony, zinc, nickel, and aluminum affect the susceptibility of the metal to IGSCC by changing the reversible potential of the grain boundaries relative to the bulk material [1.8]. A galvanic cell can be formed due to the presence of passive film on the surface of a material. This film is weakened or does not form where grain boundaries intersect the surface. This is due to diffusion of species from the grain boundary region and/or the precipitation of species at the grain boundary that alter the metal matrix. In thermally treated stainless steels, chromium precipitates, such as $Cr_{23}C_6$, result in a chromium depleted region near the grain boundaries [1.9]. Because the depleted region has a higher passivation potential, the grain boundary will be anodically dissolved at a certain potential [1.10].

Transgranular stress corrosion cracking (TGSCC) also occurs when a galvanic cell exists between an active crack tip and passive crack walls. When agents, such as chloride ions, in the aqueous solution are concentrated in cracks and crevices, they weaken the passive film. The passive film will rupture at the crack tip because it acts as a stress concentrator and the underlying material will corrode anodically. The same agents also encourage crack growth by slowing the formation of a new passive film.

For a passive film to form on the surface of a crack, the electrochemical potential of the aqueous solution must fall within a certain range [1.11]. Species in the water that affect this potential include ions such as metals and halides and radiolysis products such as hydrogen, oxygen, and hydrogen peroxide. The radiolysis products are formed when water molecules are broken apart by ionizing radiation.

The mechanism of crack advance in austenitic materials that has been widely accepted in the stress corrosion cracking literature is the slip dissolution/film rupture model

originally developed by Ford and Andresen [1.7,1.12,1.13]. Crack propagation by the slip dissolution/film rupture mechanism results from a combination of anodic dissolution and stress/strain conditions that result in dislocation motion [1.14]. The tensile stress that is characteristic of all SCC results in a pileup of dislocations at the crack tip because it acts as a stress concentrator. These dislocations cause the protective film to separate in cross slip at the crack tip exposing bare metal to the environment. This bare metal then undergoes rapid anodic dissolution until the metal repassivates. As a result, the new crack tip has advanced into fresh material where dislocations begin to pile up again.

An alternative method, brittle film rupture, considers the separation of the passive film to be due to brittle fracture. In this mechanism, dislocations pile up behind the passive film until it ruptures exposing the bare metal beneath. The former process is more likely to occur when the passive film is thin and coherent with the underlying matrix. The latter process will dominate for a thick incoherent passive film. The dislocations result from a monotonically increasing stress, a cyclic stress, or creep resulting from a high constant stress. Experimental results have supported the slip dissolution/film rupture model because the dissolution rate of bare metal has correlated positively with the SCC propagation rate in a wide range of materials [1.13].

The slip dissolution/film rupture mechanism for stress corrosion cracking occurs because the thermodynamically stable oxide film ruptures due to strain concentrations at the crack tip. The crack advance rate is governed by the oxidation rate of the surface exposed by the fracture of the film, the rate of formation of the new film (repassivation), and the time required for the crack tip strain rate to rupture the oxide film [1.12].

1.1.3. Mixed Mechanisms

Another mechanism that involves brittle cracking of the passive film is the film-induced cleavage or environmentally induced cleavage model [1.12]. This model has been described as a combination of the slip dissolution/film rupture model and the brittle film fracture model [1.7]. Here, the brittle film is ruptured as the stress at the crack tip increases due to the motion of dislocations. The release of energy associated with rupture of the brittle film results in the cleavage of the underlying metal matrix. The amount of cleavage induced in the bulk metal is affected by the coherency between the film and the metal matrix, the thickness and ductility of the film, and the bond strength at the film-metal interface [1.13].

The film-induced cleavage mechanism is supported by experimental results. The rate of crack propagation in anodic environments where hydrogen embrittlement is unlikely to be a factor is often controlled by the dissolution rate of the metal. Crack propagation rates that exceed the anodic dissolution rate support the concept that cleavage occurs in the metal matrix. Fractographic observations of transgranular cracks have also supported the film-induced cleavage mechanism. Specifically, in some cases the sides of cracks match and interlock completely, indicating that neither dissolution nor plasticity contribute greatly to the cracking [1.13]. If the conditions for hydrogen embrittlement are not present, film-induced cleavage is the most reasonable explanation for this fractography.

In the IEDM, the principles of the film-induced cleavage model are used in a novel manner. Rather than using the cleavage component, C, to back into a description of why crack growth rates may be higher than that predicted by the slip dissolution/film

rupture model, the cleavage component has been formulated here to describe the contribution of hydrogen embrittlement to cracking at low potentials. When the hydrogen embrittlement component of cracking is negligible, the additional component of environmentally assisted cleavage, C, is equal to zero. In this case, the cleavage model becomes the slip dissolution/film rupture model. Alternatively, hydrogen embrittlement can dominate cracking at low potentials. In the IEDM the cleavage of the underlying matrix can dominate the crack growth rate.

1.2. Model Flow

The IEDM consists of several models and correlations. Figure 1.1 is a flow chart of the interaction between the various components. In the figure, arrows represent the flow of information from one model or correlation to another. The unframed text alongside the arrows represents the output of one model and the input to the next. The boxes represent the models and major correlations included in the IEDM and the ovals represent direct inputs to each of the various submodels. This data includes mostly physical or chemical properties of the materials involved. The resulting outcome is the pentagon that represents the crack growth rate.

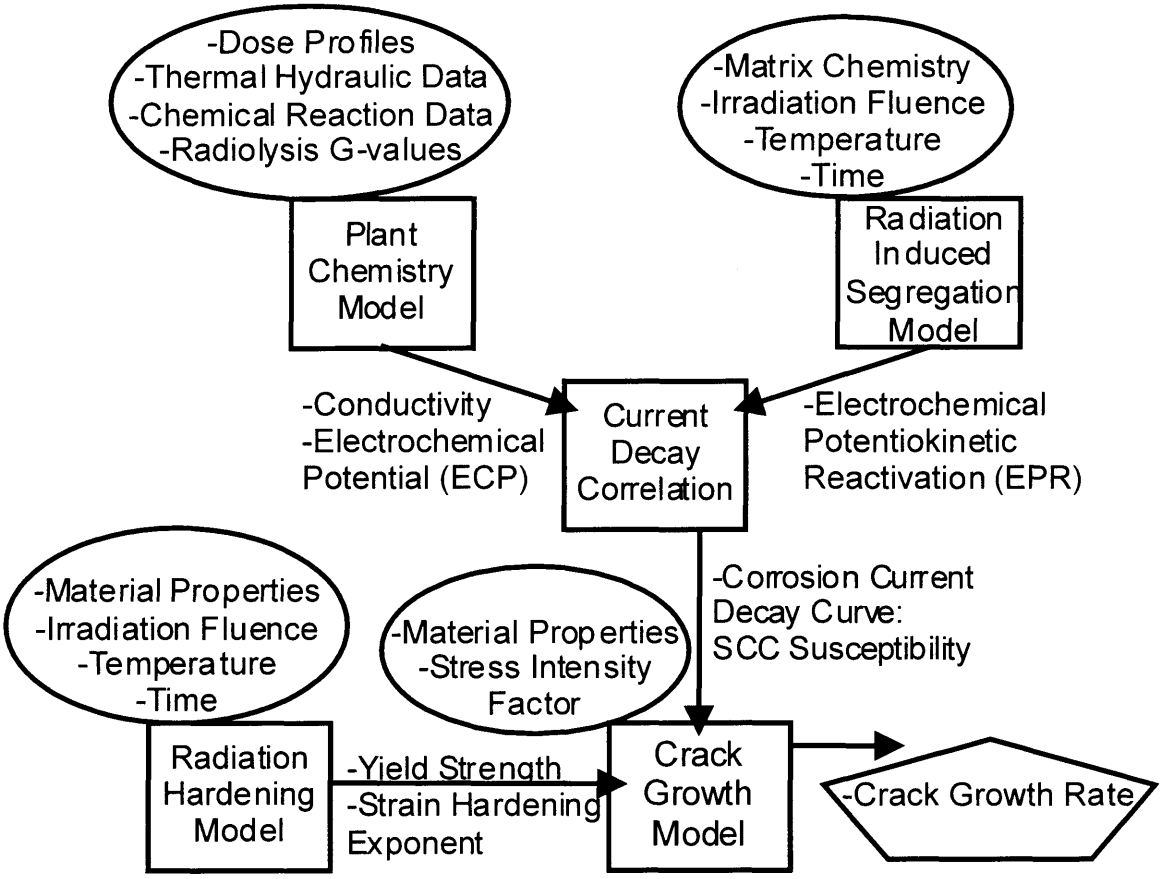

Figure 1.1. Flow chart of the various models and correlations included in the IEDM.

The basis of the IEDM is the crack growth model and its inputs determined the design of the balance of the IEDM. The crack growth model requires two main classes of information: physical properties such as stresses and strengths, and electrochemical properties. The physical properties come from the direct inputs (oval) and the radiation hardening model. The electrochemical properties are summed up in the current decay curve. The current decay curve correlation requires three inputs, the electrochemical potential (ECP), the electrochemical potentiokinetic reactivation value (EPR), and the bulk conductivity. The ECP is determined within the plant chemistry model using the concentrations of O_2, H_2, and H_2O_2 and the flow rate. The conductivity is determined using the concentrations of ions determined by the plant chemistry model. The output

from the radiation induced segregation model is the profile of alloy chemistry at the grain boundary [1.3]. The EPR is determined from the chromium profile using a correlation. Each of these models will be discussed in detail in the appropriate section of this dissertation.

1.3. Previous Modeling Work

According to Macdonald, "two models have emerged as leading candidates for the purpose of estimating crack growth rates in light water reactor coolant circuits" [1.15]. These two are the PLEDGE model of General Electric and his own model, the Coupled Environmental Fracture Model (CEFM). An additional model is in use by the Electric Power Research Institute as part of the BWR Vessel and Internals project (BWRVIP) [1.16]. The CEFM has been utilized in the development of a larger model, the DAMAGE-PREDICTOR [1.17-1.20]. Both the DAMAGE-PREDICTOR and the IEDM include a model for reactor chemistry and radiolysis. These three models, as well as the IEDM developed here share many methods including the slip dissolution/film rupture crack advance mechanism. The following analysis of PLEDGE, the CEFM and DAMAGE PREDICTOR, the BWRVIP, and the IEDM will demonstrate the similarities and differences between these models. Additionally, I will establish that the IEDM is an improvement over all these previous models both in terms of theoretical rigor and level of integration.

A significant issue impacting the utilization and improvement of these models is their availability. Like the CEFM, which was created at Penn State by Macdonald and his graduate students, the IEDM is available to the public. Access to both the PLEDGE

and BWRVIP models is extremely restricted. The General Electric Corporation holds proprietary rights to the PLEDGE model, and the BWRIP model is only available for use by EPRI member utilities. It is apparent that any improvements to models which are largely unavailable will only be through their respective companies, while those models emerging from educational institutions have significantly higher potential for development.

1.3.1. GE's PLEDGE model

The PLEDGE model of General Electric has chiefly been developed by Andresen and Ford [1.7,1.12,1.13]. Few details concerning the empirical correlations used in the PLEDGE model have been published [1.15]. However, many details on the theory behind this model have been included in published works by Ford and Anderson, as well as in EPRI reports [1.13]. Specifically, many of the details of the model and theory were presented at conferences in the late 80s [1.7,1.12,1.21].

Similar to the IEDM, PLEDGE uses the slip dissolution/film rupture mechanism developed by Ford and Andresen. The model presented by Ford and Andresen in 1988 uses the stress, corrosion potential, conductivity, temperature, and other inputs that are not expressly stated. These inputs indicate that their model begins with changing plant parameters that must be measured continuously. This contrasts with the IEDM, which integrates models to evaluate the chemistry and the materials parameters as they change during reactor operation. It is possible that empirical correlations have been developed that add some upstream capabilities to PLEDGE. However, due to the proprietary nature of the model, its scope at the present time cannot be determined. By comparing

conference papers [1.7,1.12,1.21] and EPRI reports [1.13] it appears that the crack is electrochemically modeled only to acquire data for an empirical model rather than modeling the crack tip each time the crack growth rates for a specific set of parameters are desired.

The crack growth model at the core of PLEDGE is rather simple. The following equation is used to find the crack growth rate:

$$\overline{V}_T = A\dot{\varepsilon}_{ct}^{m} \tag{1.1}$$

The crack tip strain rate, ε'_{ct} is determined from experimental parameters or assumptions regarding in core conditions. The slope of the current decay curve slope, m, is then determined from an empirical correlation of the electrochemical potential (ECP), the electrochemical potentiokinetic reactivation (EPR), and the conductivity at 25°C. The current decay curve slope represents the rate at which the corrosion current decreases when bare metal is exposed to conditions that will result in the formation of a passive film. As the passive film develops the corrosion rate decreases exponentially with slope, m. 'A' is a constant replacing several constants from Faraday's Law and other "bulk system parameters such as, carbon content, effective chromium content, heat treatment, dissolved oxygen, flow rate, etc." [1.13]. In actuality, A is determined from m by a second empirical correlation. It was found that for austenitic stainless steels A = $0.0078m^{3.6}$. This relationship is used to find the crack growth rate. Therefore, the rates are based only on m and ε'_{ct}. Another simplification used in this model is to define the crack tip strain rate, ε'_{ct}, as a simple function of stress intensity factor, K [1.13,1.22]:

$$\dot{\varepsilon}_{ct} = 6 \cdot 10^{-14} \cdot K^4 \qquad (1.2)$$

In Ford and Andresen's work, it is emphasized that although this formulation leads to a satisfactory statistical agreement between observed and predicted crack growth rates for a wide range of material and environmental conditions, it is not based on a fundamental knowledge of the dynamics of crack-tip plasticity [1.13].

The crack tip mechanics model in PLEDGE does not reach the level of determinism of the IEDM. In the IEDM, the crack tip strain rate is accurately determined from the crack tip stress intensity factor, while PLEDGE only has a series of simple correlations between the applied strain rate and the crack tip strain rate which differ for various loading types. The IEDM is more accurate when data is extrapolated beyond that used to calibrate the model because it accurately accounts for each factor which effects the crack growth rate.

1.3.2. Coupled Environmental Fracture Model and DAMAGE-PREDICTOR

Developed largely by Macdonald and Urquidi-Macdonald [1.23] at Penn State, the CEFM endeavors to deterministically model the electrochemical processes involved in cracking. This model differs from the other models (including the IEDM) in the method used to account for the relationship between the anodic process of metal dissolution and the cathodic process of oxygen reduction. It requires that the anodic process occur at the crack tip while the cathodic process occurs outside of the crevice on the external surface of the metal [1.23]. While maintaining charge conservation is valid to accurately model the relationship electrochemical reactions, other researchers disagree

with the premise that cathodic processes do not occur within the crack [1.24,1.25]. Like the other models, the CEFM model uses the slip dissolution/film rupture model to describe the cracking process at the crack tip.

Problems with the CEFM have been identified by Ford and Andresen [1.24,1.45] in a series of critiques interspersed by challenges of the PLEDGE model by Macdonald [1.15]. It has been pointed out that the requirement of the CEFM that the current outside the crack equal the crack tip current is inaccurate for several reasons. Primarily, the crack walls (not just the outer surface) can consume the current emanating from the crack tip. In the CEFM, reactions on the crack walls are ignored. Additionally, the flow between the crack tip and outer surface is not likely to control cracking because the coolant within the crack has been experimentally shown to be highly deaerated by the consumption of oxygen along the crack walls. This deaerated condition is not indicated by the CEFM because wall reactions are ignored. If wall reactions were taken into consideration, it would result in low conductivity along the crack length, making coupling between the crack tip and outer surface difficult.

The DAMAGE-PREDICTOR model, developed by Yeh, is actually a combination of the CEFM and a plant chemistry and radiolysis model that is essentially similar to the RadiCAL model used to determine plant chemistry in the IEDM [1.17-1.20]. After calculating the concentrations of hydrogen, oxygen, and hydrogen peroxide, the DAMAGE-PREDICTOR model uses the mixed potential model to deterministically find the electrochemical potential in the coolant. A crack growth rate for a set of standard conditions is then calculated using the CEFM. The DAMAGE-PREDICTOR takes a major step by combining a plant chemistry model with a crack growth model. However,

because this model assumes the conductivity and material properties, it does not reach the level of integration of the IEDM. The DAMAGE-PREDICTOR model is significant because it is highly deterministic. However, the use of the CEFM obviously leads to the same problems previously defined.

A major obstacle for deterministic models is that they focus on crack tip chemistry more than crack tip processes. Put differently, the CEFM assumes that the slip dissolution/film rupture process controls the crack tip. However, the model for current decay due to repassivation at the crack tip does not reflect a first principles understanding. In the CEFM, the repassivation of the crack tip is modeled by assuming that the fraction of the surface that is bare at time, t, after film rupture follows an exponential relation [1.23]. In fact, the film thickens evenly over the whole area of exposed metal. More problematic is the assumption that the slope of the current decay curve is 0.5. It does not seem logical to develop a highly deterministic model for the current in the crack only to assume an average figure for the rate of change of that current during the cracking process. In the IEDM, the slope of the current decay curve follows an empirical correlation of the potential, conductivity, and sensitization of the system.

1.3.3. EPRI's BWRVIP model

There is little published information regarding the model used in the BWR vessel and internals project (BWRVIP). However, because some of the early research by Andresen and Ford, which ultimately became the PLEDGE model, was supported by EPRI, the BWRVIP model is likely a subset of GE's PLEDGE. It is known that the BWRVIP model does not take into account radiation effects [1.26]. The effect of

radiation in terms of water radiolysis, radiation induced segregation, and radiation hardening is not included. This model attempts only to determine corrosion rates for given levels of sensitization, yield strength, and water chemistry, rather than attempting to follow the changes in these parameters over the life cycle and operation cycle of the reactor.

1.4. References

[1.1] Chun, J. H., "Modeling of BWR Water Chemistry." SM thesis, Nuclear Engineering Department, Massachusetts, Institute of Technology, 1990.

[1.2] Grover, D. J., "Modeling Water Chemistry and Electrochemical Corrosion Potentials in Boiling Water Reactors." SM thesis, Nuclear Engineering Department, Massachusetts, Institute of Technology, 1996.

[1.3] Boerigter, S. T., "An Investigation of Neutron-Irradiation Induced Segregation in Austenitic Stainless Steels," ScD theses, Nuclear Engineering Department, Massachusetts, Institute of Technology, 1992.

[1.4] Bruemmer, S. M.; Charlot, L. A.; Arey, B. W., Sensitization Development In Austenitic Stainless Steel: Correlation Between Stem-Eds And Epr Measurements, Corrosion Vol. 44 No. 6 (1988) pp. 328-333.

[1.5] Clarke, W.L., Cowan, R.L., and Walker, W.L., Comparative Methods for Measuring Degree of Sesitization in Stainless Steel, Intergranular Corrosion of Stainless Alloys ASTM STP 656, R. F. Steigerwald, Ed., American Society for Testing and Materials, (1978) p.p. 99-132.

[1.6] Bruemmer, S. M.; Composition-Based Correlations to Predict Sensitization of Austenitic Stainless Steels, Corrosion Vol. 42 No. 1 (1986) pp. 27-35.

[1.7] Ford, F. P., Status of Research on Environmentally Assisted Cracking in LWR Pressure Vessel Steels. Journal of Pressure Vessel Technology V. 110 (May 1988) pp. 113-28.

[1.8] Parkins R. N., Stress Corrosion Cracking, Environmentally-Induced Cracking of Metals, NACE 10, (Oct. 1988) p. 1.

[1.9] Bruemmer, S. M.; Quantitative Modeling of Sensitization Development in Austenitic Stainless Steel, Corrosion Vol. 46 No. 9 (1990) pp. 698-709.

[1.10] Chung, H. M., Ruther, W. E., Sanecki, J. E., Kassner, T. F., Grain Boundary Microchemistry and Intergranualer Cracking of Irradiated Austenitic Stainless Steels. 6th International Symposium on Environmental Degradation of Materials in Nuclear Power Plant-Water Reactors V. 1 (Aug. 1993) pp. 511-19.

[1.11] Staehle, R. W., Understanding "Situation-Dependent Strength": A Fundamental Objective in Assessing the History of Stress Corrosion Cracking, Environmentally-Induced Cracking of Metals, NACE 10, (Oct. 1988) p. 561.

[1.12] Ford F. P., The Crack-Tip System and Its Relevence to the Prediction of Cracking in Aqueous Environments, Environmentally-Induced Cracking of Metals, NACE 10, (Oct. 1988) p. 139.

[1.13] Ford, F. P., Taylor, D. F., Andresen, P. L., Ballinger, R. G. "Corrosion-Assisted Cracking of Stainless and Low-Alloy Steels in LWR Environments", EPRI, NP-5064M, (1987).

[1.14] Ford, F. P., Quantitative Prediction of Environmentally Assisted Cracking. Corrosion. V. 52, N. 5 (1996) pp. 375.

[1.15] Macdonald, D. D., On the Modeling of Stress Corrosion Cracking in Iron and Nickel Base Alloys in High Temperature Aqueous Environments. Corrosion Science V. 38 N. 6 (1996) pp. 1003-10.

[1.16] Bilanin, W. J., Dyle, R. L., BWR Vessel and Internals Project (BWRVIP), American Society of Mechanical Engineers, Pressure Vessels and Piping Division (Publication) PVP Service Experience and Design in Pressure Vessels and Piping Proceedings of the 1996 ASME Pressure Vessels and Piping Conference V. 335 (1996).

[1.17] Yeh, T.-K., Macdonald, D. D., Modeling the Development of Damage in BWR Primary Coolant Circuits. 7th International Symposium on Environmental Degradation of Materials in Nuclear Power Plant-Water Reactors V. 2 (Aug. 1995) pp. 909-920.

[1.18] Yeh, Tsung-Kuang, Macdonald, Digby D., Modeling Water Chemistry, Electrochemical Corrosion Potential, and Crack Growth Rate in the Boiling Water Reactor Heat Transport Circuits -- III: Effect of Reactor Power Level. Nuclear Science and Engineering: The Journal of the American Nuclear Society. V. 123, N. 2 (1996) pp. 305.

[1.19] Yeh, Tsung-Kuang, Macdonald, Digby D., Modeling Water Chemistry, Electrochemical Corrosion Potential, and Crack Growth Rate in the Boiling Water Reactor Heat Transport Circuits -- II Simulation of Operating Reactors. Nuclear Science and Engineering: The Journal of the American Nuclear Society. V. 123, N. 2 (1996) pp. 295.

[1.20] Yeh, Tsung-Kuang, Macdonald, Digby D., Motta, Arthur T., Modeling Water Chemistry, Electrochemical Corrosion Potential, and Crack Growth Rate in the Boiling Water Reactor Heat Transport Circuits -- I: The DAMAGE-PREDICTOR Algorithm. Nuclear Science and Engineering: The Journal of the American Nuclear Society. V. 121, N. 3 (1995) pp. 468.

[1.21] Ford, F. Peter, Andresen, Peter L., Development and Use of a Predictive Model of Crack Propagation in 304/316L, A533/A508 and Inconel 600/182 Alloys in 288 C Water, Environmental Degradation of Materials in Nuclear Power Systems,(`88) p. 789-800.

[1.22] Angeliu, T. M., Andresen, P. L., Effect of Zinc Additions on Oxide Rupture Strain and Repassivation Kinetics of Iron-Based Alloys in 288(Degree)C Water. Corrosion V. 52 (Jan. 1996) pp.28-35.

[1.23] Macdonald, Digby D., Urquidi-Macdonald, Mirna, A Coupled Environment Model for Stress Corrosion Cracking in Sensitized Type 304 Stainless Steel in LWR Environments. Corrosion Science V. 32, N. 1 (1991) pp. 51-81.

[1.24] Andresen, P. L., 'Current' Issues in SCC: Where Does Current Flow in Cracks?

[1.25] Andresen, P. L.; Ford, F. P., Response to "On the Modeling of Stress Corrosion Cracking of Iron and Nickel Base Alloys in High Temperature Aqueous Environments." Corrosion Science. V. 38, N. 6 (1996) pp. 1011.

[1.26] Communication with Ron Ballinger who spoke with Larry Nelson, spring 1999.

2. Effect of Radiation on Stress Corrosion Cracking

2.1.Radiation Effects on Fe-Ni-Cr Alloys

2.1.1. Radiation Induced Segregation

Passivity is the property of a metal in a solution that it corrodes at a very low rate despite being highly active in the electrochemical series relative to the solution [2.1]. A metal becomes passive because its corrosion products form a layer that adheres to the surface of the metal and restricts the rate of further corrosion. In stainless steels, it is the addition of chromium that allows the metal to be passive in a wide range of environments.

Sensitization is the process by which the metal matrix near the grain boundary is depleted in one or more beneficial elements or enriched in one or more detrimental elements resulting in an increased susceptibility to intergranular stress corrosion cracking [2.2]. In stainless steels and nickel alloys, such as Inconel 600, chromium is depleted at the grain boundary. This is significant due to chromium's role in passive film formation. It has been shown that when chromium levels decrease below approximately 13 wt%, passivation breaks down along grain boundaries resulting in enhanced stress corrosion cracking and/or intergranular attack.

For corrosion to take place two half-cell reactions must be operating simultaneously. One of these, the anodic reaction, is the oxidation of the metal. The other one, the cathodic reaction, is the reduction of another species that is in the solution.

The potential and rate at which the reaction takes place are determined by the balance of the currents produced [2.3]. The two reactions must have equal and opposite currents. Polarization curves indicate the relationship between the current and the potential for anodic and cathodic reactions. Figure 2.1 is an illustrative example of polarization curves for stainless steel with various quantities of chromium. The curved lines represent the anodic reaction of metal oxidation and the straight line represents the cathodic reaction. When there is adequate chromium, the intersection of the cathodic and anodic reactions results in low current density. When the chromium content is low, the same cathodic reaction intersects the anodic reaction at a much higher current.

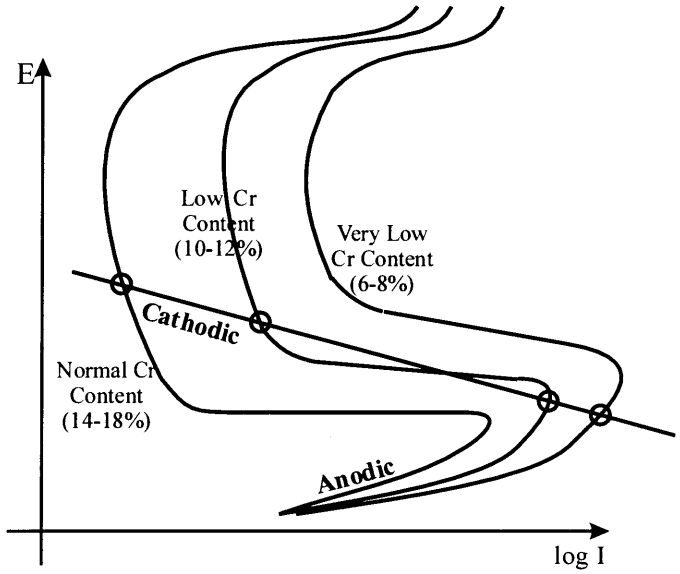

Figure 2.1. Illustration of stainless steel potential curves for varying chromium contents [2.3].

A source of sensitization in irradiated materials is radiation induced segregation (RIS) [2.4]. RIS is the result of preferred transport of atoms of specific alloying elements due to the flux of point defects towards defect sinks (usually grain boundaries). The point defects are vacancies and interstitials in the lattice that are formed when atoms are knocked out of their lattice positions by high-energy particles. In a nuclear reactor the

high-energy radiation responsible for radiation induced segregation is neutrons. Approximately 25 eV are required to displace an atom from its lattice position [2.5]. Therefore, each 1 MeV neutron will result in approximately 40,000 displaced atoms. Several of the displaced atoms will form vacancy defect pairs. This occurs when a displaced atom comes to rest in an interstitial position leaving a lattice position empty. At the grain boundaries, the high stacking fault energy masks stress field of the defect [2.5]. Therefore, it is energetically favorable for defects to be near grain boundaries. In addition to lowering the energy of the system by masking the stress field, defects at grain boundaries recombine. This recombination results in a lower concentration of defects near the grain boundaries. The low concentration of defects results in a defect gradient and the flow of defects toward the grain boundaries.

The directions of segregation, as well as the rates of segregation are controlled by the atomic volume of each species. Atoms that are smaller than average, preferentially migrate with the interstitial flux toward the grain boundaries, while larger atoms migrate against the vacancy flux away from the grain boundaries. As the vacancies and interstitials move towards grain boundaries, nickel, silicon, phosphorus, and sulfur atoms move with them. In response to the defect flux, Chromium, molybdenum, iron, and titanium move away from the grain boundaries [2.5].

The flow of chromium away from grain boundaries leads to chromium depletion. This results in an increase in susceptibility to intergranular stress corrosion cracking as described above. There are two likely mechanisms for RIS. These are the inverse Kirkendall effect and solute-defect binding [2.5]. The inverse Kirkendall effect is based on the movement of vacancies and solute-defect binding is based on the movement of an interstitial and lattice atom pair.

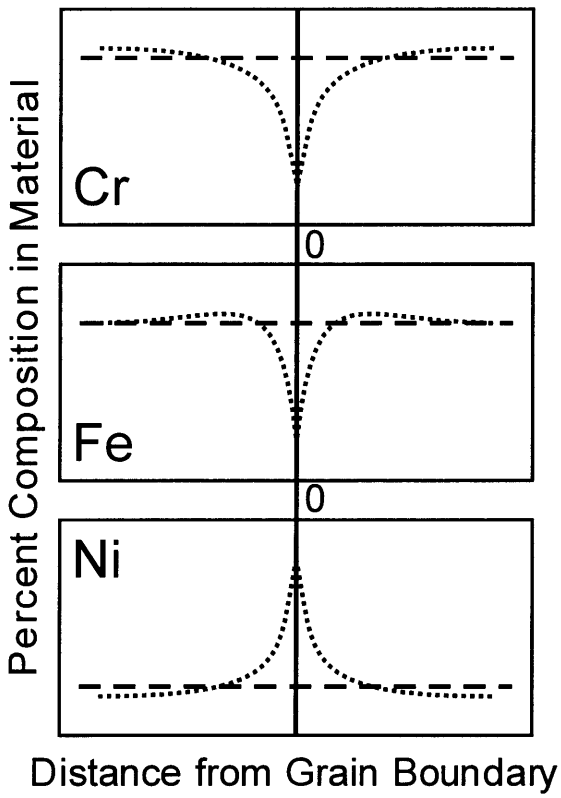

Figure 2.2. Example of profiles for main elements of austenitic alloys.

The inverse Kirkendall effect is the primary mechanism for radiation induced segregation. Figure 2.3 is an illustration of this effect. Vacancies in the metal lattice constantly interchange with lattice atoms. The rate at which atoms move into a vacancy varies with the atomic volume of the atom. Therefore, in a concentration gradient of vacancies faster moving atoms will preferentially move in the direction opposite vacancy motion and, by conservation of mass, slower atoms will move with the vacancies [2.5]. In Figure 2.3, F marks the species that preferentially exchange positions with the vacancies leaving the grain boundary. The slower moving species marked with an S move toward the grain boundaries by mass conservation.

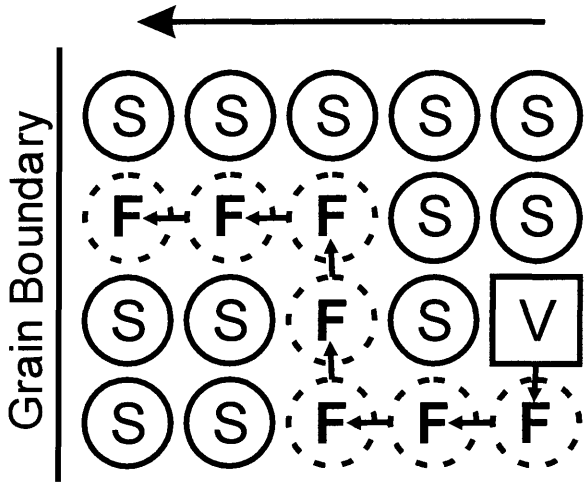

Figure 2.3. Illustration of the inverse Kirkendall effect.

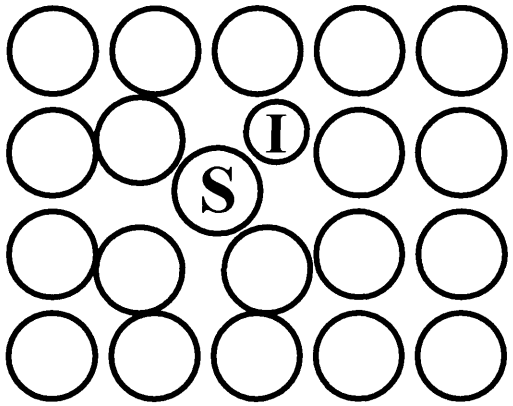

Figure 2.4. Illustration of solute-interstitial pair.

The other mechanism for radiation induced segregation is solute-interstitial binding. Whereas in the inverse Kirkendall effect migration occurs by lattice exchange, here the solute-interstitial pair must have long-range migration as a pair. Because of the likelihood that the pair will separate, the inverse Kirkendall effect is the dominant mechanism of RIS and the solute-interstitial binding mechanism is secondary. The interstitial here is a self-interstitial, not an impurity. Therefore, the smallest atoms are those most likely to form a self-interstitial/solute pair. This is because when the pair is made up of smaller atoms, the likelihood is increased that the migration energy is less than the dissociation energy [2.5]. Therefore, combinations of smaller atoms are more

likely to migrate resulting in a net flux of smaller than average atoms toward defect sinks. This has the same result as the inverse Kirkendall effect where small atoms move toward grain boundaries and larger atoms move away from grain boundaries to conserve lattice positions.

In planning the IEDM, it was determined that the radiation induced segregation had to be modeled to completely characterize the effect of radiation on reactor components. The model chosen was developed and implemented by Boerigter [2.5]. The radiation induced segregation model uses a random alloy model to follow the changing species concentrations in an alloy in the presence of defect fluxes resulting from a neutron flux. The rate of change of the concentration of defect, d, is the negative gradient its flux.

$$\frac{\partial C_d}{\partial t} = -\nabla \cdot \vec{J}_d \tag{2.1}$$

The rate of change of the concentration of vacancies and interstitials equals the negative gradient of the flux plus the net defect production, K_o-L.

$$d = V, I \quad \frac{\partial C_d}{\partial t} = -\nabla \cdot \vec{J}_d + K_0 - L \tag{2.2}$$

Partial diffusion coefficients relate the concentration gradients to the atomic species fluxes.

$$\vec{J}_k = D_k^V \frac{\partial C'_V}{\partial x} + D_k^I \frac{\partial C'_I}{\partial x} + D_k^k \frac{\partial C'_k}{\partial x} + \sum_{j \neq k} D_k^j \frac{\partial C'_j}{\partial x} \tag{2.3}$$

The partial diffusion coefficients, D_k, are computed from experimentally determined defect-species exchange enthalpies, theoretically evaluated correlation factors, local species and defect concentrations, and other factors [2.5]. The set of non-linear parabolic partial differential equations arising from the set of conservation

equations is then solved using the method of lines [2.5]. In this method, the spatial dependence of the problem is approximated by finite-difference methods. Then the remaining non-linear ordinary differential equations are simultaneously solved numerically. Because the concentrations of self-interstitials are very small (20 orders of magnitude) compared to the species concentrations, the system of equations is very stiff and is difficult to solve. The Livermore Solver of Ordinary Differential Equations (LSODE) is used to solve the equations. This same method is used in the radiation chemistry analysis loop model, which will be discussed subsequently [2.6,2.7].

The results of the radiation induced segregation model have been compared to several experimentally measured profiles on alloys exposed to neutron irradiation [2.5]. Select examples of this extensive confirmation can be found in the verification chapter of this thesis. Agreement with published data is excellent. Of particular importance are the chromium concentrations near the grain boundaries that are more accurately modeled as compared to previous RIS modeling efforts in the literature [2.5].

In completing a sensitivity study of the RIS model, Boerigter determined that segregation is highly dependent on the vacancy exchange enthalpies of the species in the metal [2.5]. The vacancy exchange enthalpies are used to determine the rate at which different species exchange lattice positions with defects. Because the exchange enthalpies are not well known, their high sensitivity is the main source of error in the model. The exchange enthalpies must be found experimentally, and the results of this experiment are the limiting factor in the accuracy of the RIS model.

While the majority of the findings from a complete analysis of the RIS model do not bear significantly on how it is used here, one issue is important. Specifically, the issue of flux versus fluence is relevant. Radiation induced segregation experiments are often done at accelerated dose levels to arrive at a fluence comparable to those acquired

after many years of actual reactor service. Figure 2.5 shows the chromium depletion profile for stainless steel 304 (19Cr-9Ni) irradiated at 100 DPA/year for 3.6 days, 1 DPA/year for 1 year and 0.01 DPA/year for 100 years. As the total irradiation time increases, the width and depth of the chromium profile also decreases even while the total fluence is held constant at 1 DPA. This indicates that accelerated tests are not likely to accurately indicate the effect of fluence on grain boundary sensitization.

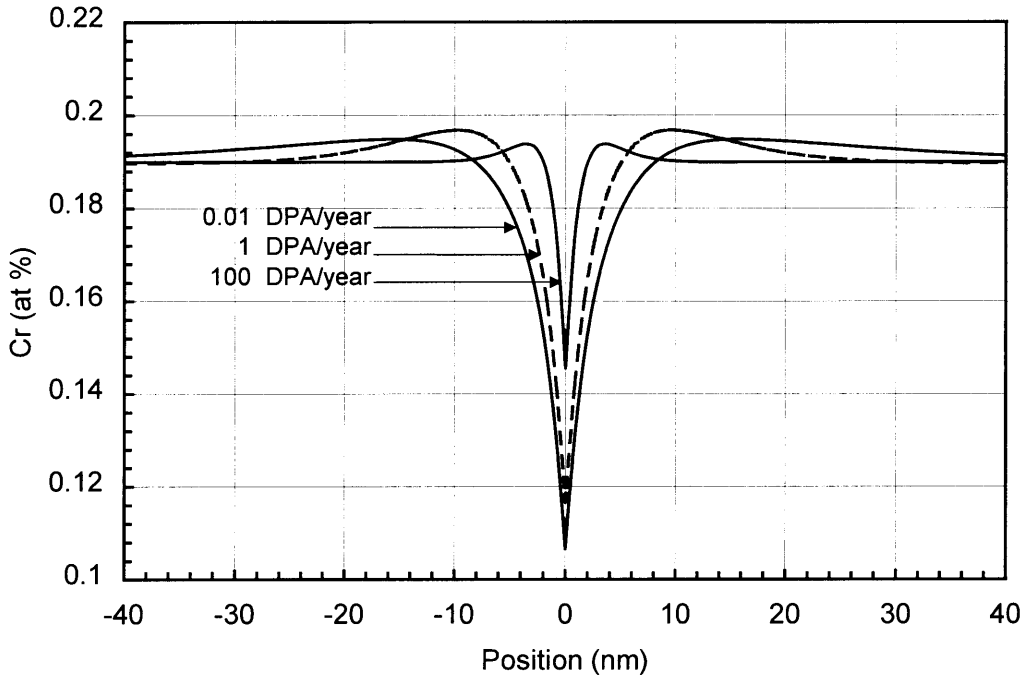

Figure 2.5. Chromium concentration profiles at various dose rates for SS 304 base case at 288C, 1 DPA [2.5].

In order to utilize the RIS model in the IEDM, the chromium profiles must be converted into an electrochemical potentiostatic reactivation (EPR) value. This issue is discussed in detail as the crack growth model is developed subsequently. The EPR value is used in evaluating the variance of susceptibility to grain boundary cracking by determining the shape of the current decay curve.

2.1.2. Radiation Hardening

The central, integrating model of this work is the model for the crack growth rate. This crack growth rate model combines a standard implementation of the slip dissolution/film rupture mechanism and a relationship for the crack tip strain rate. The yield strength of the material is a significant input to the crack tip strain rate correlation. For completeness, the yield strength must be determined by the model (rather than inputted by the user) because it is subject to change as the metal is exposed to radiation. This phenomenon is called radiation hardening. As the metal becomes harder with exposure to neutron bombardment, its ability to harden further is reduced. This leads to the exponential form of the equation which radiation hardening follows, as well as a decrease in the strain hardening exponent. Because the metals investigated here work harden when exposed to high strains, the model for the crack tip strain rate includes the stain hardening exponent which gives the exponential slope of this effect. As the metal becomes harder due to radiation fluence, subsequent strain hardening will be diminished. Therefore, the strain hardening exponent decreases with radiation fluence.

Radiation hardening is not only important because the yield strength is an input to the crack tip strain rate solution, rather it has been shown to correlate with an increased susceptibility to intergranular stress corrosion cracking (IGSCC) [2.8]. In fact, IGSCC has been shown to correlate better with yield strength than with grain boundary chromium depletion [2.8]. In another experiment, samples were irradiated at 200 and 400°C. While Cr depletion was significantly suppressed in 200°C irradiation compared to 400°C irradiation cracking still occurred for both tests. This indicated that radiation hardening correlated with IASCC better than grain boundary chromium depletion [2.9].

Despite these indicators of its importance, the role of radiation hardening remains rather uncertain. Current understanding is inadequate, due partially to radiation hardening following a similar dose dependence to the grain boundary composition evolution [2.9]. Using the radiation hardening model, the IEDM can isolate the effect of yield strength and simulate its effect on the crack growth rate.

The yield strength of the metal changes with time slowly relative to the rate of change of the system chemistry and the time scale for which crack growth rates are determined. Therefore, the yield strength of the metal at a given time can be determined from the reactor operation history independent of the other models used in this study. The model is straightforward so that the input data needed to determine the current and future hardness is easy to obtain. The necessary information includes the initial state of the metal, the initial yield strength, and the total fluence. However, the model was developed so that once the details of the metal at a point in time are known, information before that point is not needed. That is, if the hardness was determined ten years previous and the fluence since that time is known, only the best guess at whether the process that hardened the material before ten years ago was work hardening or irradiation hardening is needed. The yield stress of irradiated metals converge to a saturation level that depends primarily on alloy composition and recent irradiation temperature [2.10, 2.11]. Therefore, the complete operation history of a reactor is not necessary as input for the model.

The majority of radiation hardening research falls into one of two main categories: irradiation assisted stress corrosion cracking (IASCC) of stainless steels and nickel base alloys and embrittlement of the reactor pressure vessel and other low-alloy

steel components. The IASCC of Fe-Ni-Cr alloys is the main thrust of the present work. While a preponderance of the hardening data for stainless steels in the literature is relevent to fast reactors [2.12] or fusion systems where radiation doses are very high [2.13], there is adequate data at the temperatures and dose levels encountered in light water reactors to formulate a useful statistical model.

To evaluate a statistical model for hardening in stainless steels and nickel based alloys the underlying phenomena must be considered. Neutron dose is typically measured in neutrons/cm^2. For damage to materials, displacements per atom (dpa) is also used. The relationship between neutrons/cm^2 and dpa depends on the energy of the neutrons and the energy required to move a metal atom from its lattice position. A typical value for stainless steel in a BWR is approximately 0.7×10^{21} neutrons/cm^2 per dpa for neutron energies > 1 MeV [2.13]. For irradiation hardening at 288°C and a low-dose of less than 5 dpa, atom displacements from their normal lattice positions in metals give rise to the formation of small vacancy and interstitial loops [2.13]. Loop densities and size increase with dose up to a density of about 10^{16}cm^{-3} and a size of about 20nm in diameter [2.8]. Dislocation loops inhibit dislocation source operation and dislocation motion through the matrix, thereby increasing the flow stress of the material [2.8]. These loops can interact to form a dislocation matrix that results in significant hardening and yield strength increases [2.13].

A phenomenon that results from the interaction of small loops and moving dislocations is dislocation channeling. During this process, the initial dislocation annihilates and/or combines with the defects on the slip plane during glide. Subsequent dislocations will glide along the same path, and this will clear out additional defects

creating a defect free path (channel). Channeling occurs at high loop density but is not likely to occur in a dislocation network. Dislocation channels are seen primarily in pure metals. However, there is limited evidence supporting the theory that dislocation channels form in stainless steels [2.8]. An alternative source of ductility in stainless steels is twinning. Twinning is a change in the orientation of the lattice due to shear stresses. Twinning is the dominant deformation mechanism acting at rapid strain rates and low temperature, such as those encountered in a light water reactor. Dislocation channeling is observed at slower strain rates and elevated temperature [2.14]. Both relief mechanisms produce highly localized deformation and large surface slip steps. As this model is developed from hardening data, it is not necessary to determine the source of the ductility.

Neutron fluence in light water reactors increases by up to 10^{20} n/cm^2 per year, depending on the location within the reactor. Yield stress increases significantly for fluence between 10^{21} and 10^{22} n/cm^2 (E > 0.1Mev), or about 1 to 20 dpa [2.12]. The most important factor affecting radiation hardening is the fluence. However, since crack rates have been shown to correlate better to yield strength than to fluence, other factors besides fluence should be used to determine the yield strength [2.13]. These factors include the initial stress state of the material, the alloy composition, and the temperature of irradiation. The temperature of irradiation is an important factor affecting irradiation hardening. However, because this model is for the primary side of light water reactors, the operating temperature will be very near 288°C. Temperature is included in the model for two reasons. First, the model is more versatile because it can predict the effect on cracking when the reactor is operating at different temperatures. Additionally, it is useful

to extrapolate data from other temperatures to extend the size of the database used to calibrate the statistical model.

An alternate method for extending the database size is to include data from sources other than light water reactors. It has been shown that for low irradiation doses, the changes in tensile properties of 316 SS produced by fission reactor neutrons, D-T fusion neutrons and Los Alamos Spallation Radiation Effects Facility (LASREF) neutrons are the same at a given fluence [2.15]. Therefore, data from sources other than light water reactors is useful to calibrate and test the statistical model.

Other factors did not significantly effect the radiation hardening of stainless steels and nickel-based alloys. It has been reported that changes in the reactor flux do not effect the rate of hardening due to a particular fluence. There was no observed influence of flux observed for a damage rate between $1.6x10^{-7}$ to $11x10^{-7}$ dpa/s [2.11]. Also, cracking susceptibilities of the BWR components could not be correlated with segregation of silicon or phosphorus impurities on grain boundaries [2.16].

A possible form of the damage (fluence) dependence is the following equation [2.11]:

$$\sigma(D) = \sigma_0 + (\sigma_\infty - \sigma_0)(1 - e^{\frac{-\ln(2)D}{D_{1/2}}}) \qquad (2.4)$$

Where σ_0 is the initial yield stress, σ_∞ is the plateau yield stress, D is the damage in dpa and a reasonable fit is obtained for $D_{1/2}$ = 2dpa. Elen and Fenici found that σ_∞ = 820MPa for annealled steel and 1040 MPa for cold worked after 6 dpa [2.11]. In a separate experiment, yield stress increased rapidly with fluence up to ~900 MPa at 3x10^21 neutrons/cm2 (~ 4 dpa) [2.13].

The radiation hardening model developed here does not use plateau values because these change with initial cold work, temperature, and alloy content. The model is based on a least squares fit to data in the literature [2.10,2.11,2.15-2.17]. Two separate least squares fits were made, one for annealed material (low initial yield strength) and one for work hardened material (high initial yield strength). If the material is put into service annealed but has a high initial yield stress then the model for annealed data will be used. However, the model will begin at some point along the curve where some irradiation hardening has already occurred. To develop the statistical model, an initial form for the equation was determined based on the general shape of the yield strength versus damage curves:

$$\sigma_y(D) = [\sigma_y]_o + A_1(288 - T) + A_2(D)^{A_3} \tag{2.5}$$

Where $[\sigma_y]_o$ is the initial yield stress, Each A is a different constant, T is the irradiation temperature, and D is the damage in displacements per atom. For the fit to both the annealed and the cold-worked data, A_1 was found to be very close to 1.0. As a result, this constant was removed from the equation. For the annealed data, A_2 is 310 and A_3 is 0.25. For the cold-worked experiments, A_2 equals 120 and A_3 equals 0.35. The following are equations with these parameters:

$$\sigma_y(D) = [\sigma_y]_o + 288 - T + 310(D)^{0.25} \tag{2.6}$$

$$\sigma_y(D) = [\sigma_y]_o + 288 - T + 120(D)^{0.35} \tag{2.7}$$

Several data sets were used to fit the coefficient A_1 [2.10,2.15,2.17]. However, only two data sets for stainless steel 316 [2.11] and 304 [2.16] at reactor coolant

temperature were used to determine the values for A_2 and A_3. In this manner, the remaining data was available to verify the model.

When the material has been annealed prior to service, the model may operate in three different regimes. If the initial yield strength is less that 250 MPa, Equation 2.6, is used without modification to determine the yield strength after irradiation. If the initial yield strength is greater than 350 MPa, then it is assumed that some irradiation hardening has already occurred. In this case, it would not be meaningful to use Equation 2.6 directly to determine the yield strength curve, as the initial steep increase with damage would have already occurred. Instead, the fluence already received by the materials can be determined by reversing the equation:

$$D = \left(\frac{\sigma_y(D) - [\sigma_y]_o - 288 + T}{291} \right)^4 \tag{2.8}$$

Where $\sigma_y(D)$ is the initial yield strength (greater than 350), $[\sigma_y]_o$ is the assumed initial yield strength at the beginning of life, and D is the fluence encountered before the period being modeled. Once the fluence before the period being modeled is determined, it is added to the fluence during the time of interest to determine the final yield strength for the component. If the initial yield strength is between 250 and 350 MPa the weighted average value of the results of these two approaches is used to find the final yield strength.

When the sample has been cold-worked prior to radiation exposure, there are also three regimes that determine the solution technique. If the initial yield stress is greater than 700 MPa then Equation 2.7 for cold-worked materials is used. If the initial yield stress is less than 250 MPa then the equation for annealed materials is used. If the value

is between 250 and 700 then the parameters (constants A_2 and A_3) are adjusted to transition smoothly from insignificantly cold worked to highly cold worked.

Another important effect of irradiation on the properties of these metals is the reduction of the strain hardening exponent. Unfortunately, little research has been completed to date on the effect of radiation on the strain hardening exponent. It has been determined that the strain hardening exponent decreases with increasing neutron irradiation levels [2.18]. It also decreases with increasing yield stress.

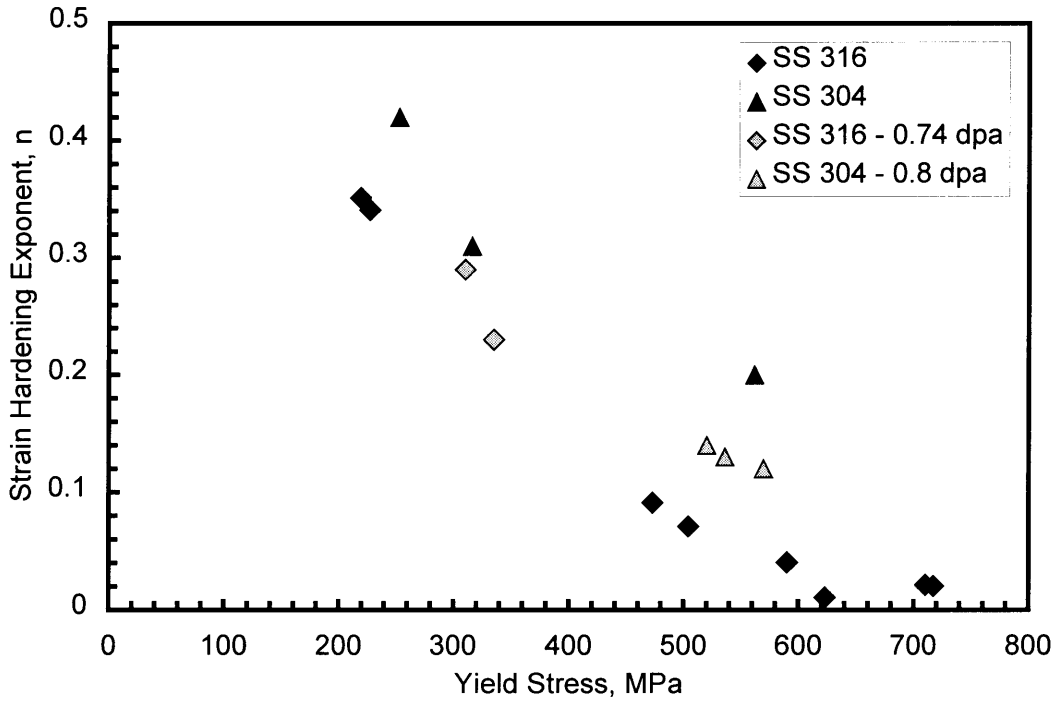

Figure 2.6. Strain hardening exponent versus yield stress data at reactor coolant temperature [2.19,2.20].

The decrease in strain hardening exponent with increasing yield stress is illustrated in Figure 2.6. However, results that separate the effect yield strength has on the strain hardening exponent from the effect of radiation are unavailable in the literature. A combination of yield stress versus exponent data from both Samuel and Hilton (Figure

2.6) indicates that any direct effect of irradiation on the strain hardening exponent cannot be separated from the effect of yield stress [2.19,2.20]. Therefore, the strain hardening exponent relationship in the model is based directly on the yield stress. The equation used in the model comes from a least squares fit of Figure 2.6:

$$n = 2.5 \cdot e^{-0.008 \cdot \sigma_y} + 0.05 \tag{2.9}$$

Where σ_y is the yield strength in MPa. This equation is truncated so that n does not exceed 0.38 for low values of yield stress. While research confirming the relationship between yield stress and crack tip stain rate is lacking, the crack tip strain rate value does not provide a significant source of inaccuracy in the crack growth model. As described in the sensitivity section of the thesis, the crack growth rate does not change greatly over the range of the strain hardening exponent from 0.05 to 0.38.

2.2. Radiation Effects on Coolant Chemistry – The Radiation Chemistry Analysis Loop Model (RadiCAL)

To a large extent the rate at which cracking occurs in a light water reactor is due to the coolant chemistry at the location where the crack is advancing. The most important electrochemical properties of the coolant are the electrochemical potential (ECP) and conductivity. The electrochemical potential determines which metals will be thermodynamically susceptible to dissolution and what dissolution processes will occur. The conductivity is a key factor in determining the rate at which cracking occurs because the current density of the dissolution process is limited by the conductivity of the electrolyte in which cracking is occurring. The MIT Radiation Chemistry Analysis Loop (RadiCAL) is a model that determines the plant chemistry in an irradiated coolant loop.

It has been developed over many years, principally by Simonson [2.21], Chun [2.6], and Grover [2.7]. The model was originally used to model the primary side of a boiling water reactor. Additionally, the model has been used to determine the chemistry of experimental loops, and with new chemistry sets could be easily used to model pressurized water reactor chemistry [2.32].

The model simulates the radiolysis of water as well as the chemical generation and annihilation of hydrogen (H_2), oxygen (O_2), hydrogen peroxide (H_2O_2), and other species. It models the convection of the fluid, the mass transport between liquid and gas phases, and other thermal hydraulic parameters needed to completely characterize the coolant chemistry. The output includes the concentrations of stable species and the ECP at any point along the flow path.

In a BWR, the radiolysis of coolant by gamma and neutron radiation results in dissolved oxygen concentrations of 150 to 300 ppb under normal water chemistry conditions [2.6]. Experimental results have shown that reducing the electrochemical potential (ECP) to below -230 mV, referenced to a standard hydrogen electrode (SHE), corresponding to a dissolved oxygen concentration of less than 20 ppb will effectively protect the system against EAC [2.22].

One method of reducing dissolved oxygen concentration is to inject hydrogen into the reactor feedwater supply. However, excessive hydrogen reacts not only with oxygen but also with nitrogen, including radioactive nitrogen 16. These nitrogen compounds are released into the main steam lines and can increase the radiation levels in the manned operating areas of the plant to unacceptable levels [2.7]. By directly determining the effect of hydrogen water chemistry on crack growth rates, the IEDM can predict the

optimal level of hydrogen addition. In-plant monitoring of water chemistry is generally not sufficient because of chemical changes in the sampling lines, such as the rapid decomposition of hydrogen peroxide at the operating temperature when the water is no longer exposed to the radiation conditions of the primary coolant.

MIT radiolysis modeling was begun in 1988 by Simonson with the MITIRAD code [2.21]. The initial code was used to simulate radiolysis in high level waste packages in underground repositories. In 1990, this model was expanded by Chun to simulate a BWR and renamed RadiCAL, for Radiation Chemistry Analysis Loop code [2.6]. This FORTRAN code models the following processes: radiolysis of water into chemical species, convection of the fluid, mass transport between gas and liquid phases, chemical generation of species, and chemical annihilation of the species. In 1993, improved thermal hydraulic models were added [2.7]. In 1996, the model was expanded and reformulated to allow for variable cross-sectional flow regions that better represent fluid velocities in the primary system [2.7]. Also, an improved ECP model was added to account not only for oxygen concentrations but also liquid velocity, hydrogen peroxide concentration, and hydrogen concentration [2.7].

The RadiCAL model, as it has been modified, takes as input chemical reaction data, g-values, radiation dose rates, and thermal hydraulic parameters. G-values are parameters that give the production rate of radiolysis products from the level of flux incident on water. Each radiolysis product has a two g-values; one each for neutron and gamma radiation. The units of g-values are number of atoms per 100 eV. The model was designed to be completely flexible by requiring all of the physical parameters of the coolant loop and the complete chemical reaction matrix to be included in the input file.

BWR input files have been created for a typical BWR-3, and BWR-4, and a BWR-1 (with no jet pumps).

2.2.1. Theoretical Modeling of Water Chemistry

The concentrations of chemical species in the model are calculated using mass balance equations for each species. These equations are derived for two-phase flow through a differential control volume. The differential equations represent the concentration as a function of position throughout the coolant loop.

To completely model the chemical processes in an irradiated reactor coolant loop the following mechanisms are accounted for:

- Generation of species due to radiolysis by neutron and gamma radiation,
- Generation and annihilation of species due to chemical reactions,
- Convection of the coolant,
- Mass transfer of species between vapor and liquid in two-phase flow.

The differential equations for the concentration of chemical species are derived with respect space rather than time, because, in two-phase flow the vapor and liquid velocities are unequal resulting in slip between the two phases. If the differential equations are taken with respect to time, they will be more complex because the respective masses of the two phases will be in different locations at the same time interval. To solve for the concentration of chemical species in the fluid, a mass balance is developed for the control volume shown in Figure 2.7.

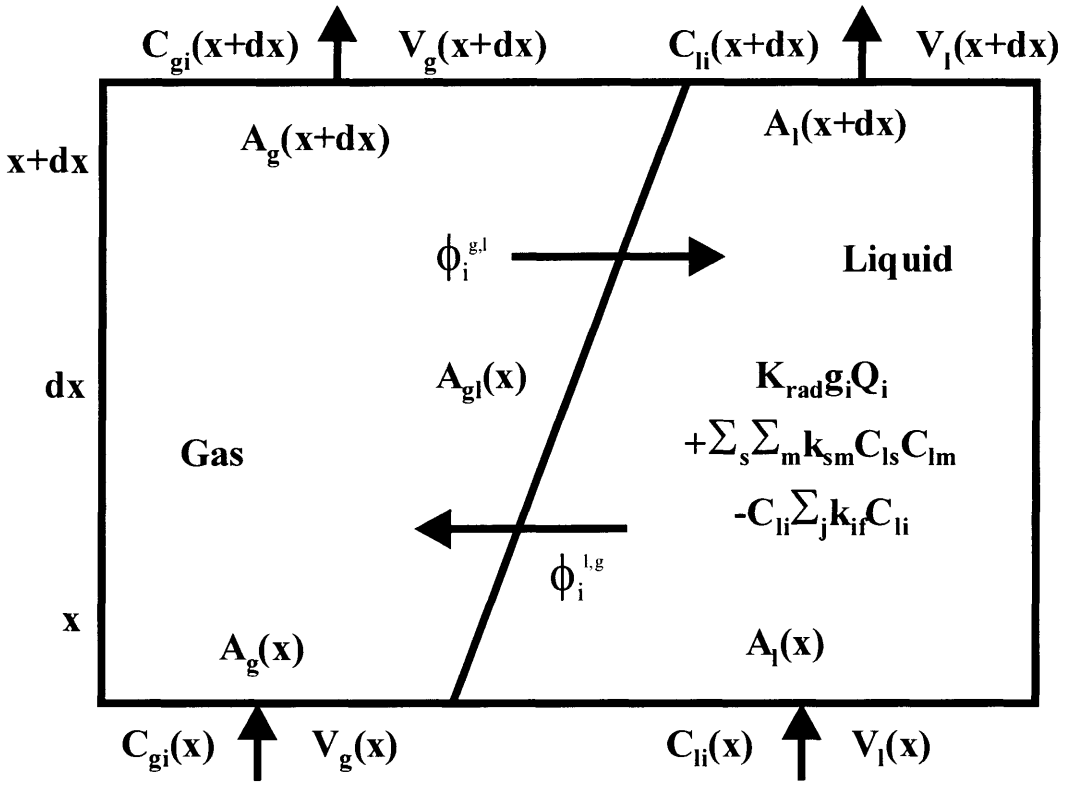

Figure 2.7. Differential Control Volume Element for a Two-Phase Fluid [2.6]

The mass balance for the liquid phase of the differential control volume is given by the following equation.

$$\begin{aligned}\frac{d[C_{li}A_l(x)dx]}{dt} &= A_l(x)dx\left[K_{rad}g_iQ_i + \sum_s\sum_m k_{sm}C_{ls}C_{lm} - C_{li}\sum_j k_{ij}C_{lj}\right] \\ &+ V_l(x)A_l(x)C_{li}(x) - V_l(x+dx)A_l(x+dx)C_{li}(x+dx) \\ &+ A_{gl}(x)\left(\phi_i^{g,l} - \phi_i^{l,g}\right) = 0\end{aligned} \tag{2.10}$$

Where C is the concentration of the given species in mol per liter, A is the cross-sectional area in square centimeters, V is the fluid velocity, K_{rad} is the conversion factor for g-values from #/100eV to mol/liter-Rad, g is the g-value of the given species in #/100eV, Q is the dose rate in Rad/s, ϕ is the concentration flux across the gas-liquid interface, g (subscript) refers to gas phase, l (subscript) refers to liquid phase, i refers to

the i-th chemical species, j refers to the j-th species and m,s refers to alternate species reacting together to form the i-th species. Similarly, the mass balance for the gas phase is given by the following equation:

$$\frac{d\left[C_{gi}A_g(x)dx\right]}{dt} = V_g(x)A_g(x)C_{gi}(x) - V_g(x+dx)A_g(x+dx)C_{gi}(x+dx) + A_{gl}(x)\left(\phi_i^{l,g} - \phi_i^{g,l}\right) = 0 \tag{2.11}$$

Expanding the convection term at x+dx using a Taylor series and neglecting second and higher order terms because the accuracy in the gas phase is adequate with a first order expansion.

$$\begin{aligned} &C_i^l(x+dx)V_l(x+dx)A_l(x+dx) \cong \\ &\left[C_i^l(x) + \frac{\partial C_i^l}{\partial x}dx\right]\left[V_l(x) + \frac{\partial V_l}{\partial x}dx\right]\left[A_l(x) + \frac{\partial A_l}{\partial x}dx\right] \cong \\ &C_i^l(x)V_l(x)A_l(x) + C_i^l(x)V_l(x)\frac{\partial A_l}{\partial x}dx + C_i^l(x)A_l(x)\frac{\partial V_l}{\partial x}dx + \\ &V_l(x)A_l(x)\frac{\partial C_i^l}{\partial x}dx \end{aligned} \tag{2.12}$$

In addition, the relationship between the cross-sectional area of the phases, the total cross-sectional area and the void fraction must be characterized to obtain the final concentration differential equations.

Cross-sectional area and void fraction relationships are used to eliminate the liquid and vapor cross-sectional areas that cannot be adequately characterized otherwise. The void fraction, or area occupied by the vapor phase, can be represented as the product of the void fraction and the total cross-sectional area as in Equation 2.13. Similarly, the product of the total cross-sectional area and the compliment of the void fraction can

represent the area occupied by the liquid phases as in Equation 2.15. Differentiating these equations yields Equation 2.14 and Equation 2.16.

$$A_g(x) = \alpha(x)A_T(x) \tag{2.13}$$

$$\frac{\partial A_g(x)}{\partial x} = A_T(x)\frac{\partial \alpha(x)}{\partial x} + \alpha(x)\frac{\partial A_T(x)}{\partial x} \tag{2.14}$$

$$A_l(x) = [1-\alpha(x)]A_T(x) \tag{2.15}$$

$$\frac{\partial A_l(x)}{\partial x} = -A_T(x)\frac{\partial \alpha(x)}{\partial x} + [1-\alpha(x)]\frac{\partial A_T(x)}{\partial x} \tag{2.16}$$

Radiolysis is the production of chemical species from the destruction of other chemical species by ionizing radiation. When gamma rays and fast neutrons irradiate water, it will dissociate into various radicals, ions, and stable species. In this model only water is considered to undergo radiolysis with the following species being produced:

$$H_2O \rightarrow e_{aq}^-, H^+, H, OH, O, HO_2, H_2, H_2O_2 \tag{2.17}$$

The rate of production of these species is proportional to the amount of energy deposited in the water by the radiation dose. The number of molecules produced per 100 eV is defined as the g-value of the radiation and is determined experimentally for each type of radiation. While g-values for stable species, O_2, H_2, and H_2O_2, can be directly measured, the g-values for short lived chemical radicals, e^-_{aq}, H^+, H, OH, O, O_2^-, and HO_2, must be calculated using a mass balance. Adding to the difficulty of determining these parameters is a temperature dependence that differs between gamma and neutron radiation [2.23]. Table 2.1 gives the G-values for neutron and gamma radiation from several sources in the literature. For neutron dose, the model uses the Burns values,

column A [2.7], and for gamma dose, the Kent and Sims dose values, column E [2.7], are used. These values were chosen at a meeting for that purpose held at MIT in 1992, the MIT radiolysis workshop. The OH g-values are modified to provide a redox balance requiring the others to be modified slightly to provide a stoichiometricly balanced set.

Table 2.1. Summary of Neutron and Gamma Radiation G-values [2.24]

	G-Value (#/100eV)							
	Neutron			Gamma				
Species	A	B	C	A	B	C	D	E
e^-_{aq}	0.93	0.4	0.37	2.7	0.4	2.8	4.15	3.69
H^+	0.93	0.4	0.37	2.7	0.4	2.8	4.15	3.69
H	0.5	0.3	0.36	0.62	0.3	0.55	1.08	0.68
H_2	0.88	2.0	1.2	0.43	2.0	0.45	0.62	0.72
H_2O_2	0.99		0.97	0.62		0.72	1.25	0.28
HO_2	0.04		0.17	0.03				
OH	1.09	0.7	0.46	2.9	0.7	2.7	3.97	4.64
O		2.0			2.0			

A: Burns' values for 25°C

B: Burns' values for high temperatures, 300-410°C

C: Christensen's values based on Forsmark-2

D: Elliot's values for high temperature, 300°C

E: Kent and Sims' values for high temperature, 270°C

The g-values are converted to moles per liter per Rad for use in the model. The production of a species is the product of the modified g-value and the dose in the control volume. Radiolysis is not considered in the vapor phase as the density of this phase is so low that radiolysis produces only a negligible quantity of chemical species.

Chemical reactions are represented by the following relationship [2.25]:

$$\sum_s \sum_m k_{sm} C_{ls} C_{lm} - C_{li} \sum_j k_{ij} C_{lj} \qquad (2.18)$$

The first term represents the production of a chemical species by the interaction of all species that can form this species. The second term represents the annihilation of a chemical species by interactions with all other species with which it can react. There is one such equation for each chemical species.

The following example indicates how reaction kinetics are determined for a first order reaction. For a chemical reaction with two reactants and two products:

$$A + B \rightarrow C + D \tag{2.19}$$

The kinetics for the generation of species C is given by:

$$\frac{d[C]}{dt} = k[A][B] \tag{2.20}$$

The kinetics for the annihilation of species A is given by:

$$\frac{d[A]}{dt} = -k[A][B] \tag{2.21}$$

These equations differ only in the sign of the rate constant, which depends on whether it is a reactant or a product. Therefore, the same rate constant, KOEF, is used for both generation and annihilation of chemical species [2.21]. This new reaction solving method is given by the following relationship:

$$\sum_{j=1}^{NRX} KOEF_{ji} k_j \prod_{m=1}^{3} C_{mi}^{l}(x) \tag{2.22}$$

The product is carried out over all reactions inputted in the reaction set matrix and the species is summed over all the reactions.

The reaction set must include not only reaction sets for all species initially found in the coolant, but also reactions for chemical species produced by radiolysis. For implementation of the model, reaction sets are composed of three parts (1) a symbolic representation of the chemical reaction occurring, (2) the rate constant which governs the rate of the reaction, and (3) the activation energy that determines the energy required to initiate the reaction. In order to model the irradiated water chemistry, these three quantities must be known accurately for radiolysis products. However, there are several different opinions of these values. Current chemical reaction sets for radiolysis products include those listed by Simonsen [2.21], Ibe [2.26], Ruiz [2.27], and Romeo [2.28]. The set currently used was determined by the MIT radiolysis workshop in 1992. In RadiCAL, up to three reactants and four products are accepted for each reaction and only up to second-order kinetics are considered. The current reaction set being used in the model is given in Table 2.1

Table 2.1. Chemical Reaction Sets

RX Name	Reactants		Products			Reaction Rates	Activation Energy
f3	e-	H2O	>H	OH-		1.6e1	12.55
f4	e-	H+	>H			3.5e+11	0.e0
f5	e-	OH	>OH-			2.0e+10	12.55
f6	e-	H2O2	>OH	OH-		1.3e+11	0.e0
f7	H	H	>H2			8.5e10	0.e0
f8	e-	HO2	>HO2-			2.0e10	12.55
f9	e-	O2	>O2-			2.6e11	0.e0
f10	e-	e-	>OH-	OH-	H2	5.e9	12.55
f11	OH	OH	>H2O2			1.7e10	0.e0
f12	H	OH-	>e-	H2O		2.0e7	18.83
f13	H	e-	>H2	OH-		2.5e10	12.55
f14	HO2-	e-	>OH	OH-	OH-	3.5e9	12.55

f15	H	OH	>H2O			5.5e10	0.e0
f16	H2	OH	>H	H2O		4.e7	18.0163
r16	H	H2O	>OH	H2		1.042e-4	85.1695
f17	H	O2	>HO2			8.6e10	0.e0
f18	H	HO2	>H2O2			2.e10	12.55
f19	H	O2-	>HO2-			2.e10	12.55
f20	O2-	e-	>HO2-	OH-		1.3e8	18.83
f21	H	H2O2	>OH	H2O		9.e7	16.61466
f22	H2O2	OH	>H2O	HO2		3.e7	13.01224
f23	HO2	OH	>O2	H2O		8.6e10	0.e0
f24	H2O2	OH-	>HO2-	H2O		1.8e10	12.55
r24	HO2-		>H2O2	OH-		5.7e5	18.83
f25	HO2	HO2	>O2	H2O2		8.5e5	22.82372
f26	HO2		>H+	O2-		2.565e4	12.55
r26	O2-	H+	>HO2			5.e10	12.55
f27	HO2	O2-	>HO2-	O2		5.e9	0.e0
f29	H+	OH-	>H2O			1.44e11	12.55
r29			>H+	OH-		0.79242	12.55
f30	OH	O2-	>O2	OH-		8.6e10	0.e0
tif	1/2O2	1/2O2	>O2			1.e15	0.e0
W32	H2O2		>OH	OH		2.00E-03	0.0
SS	H2O2		>1/2O2	H2O		0.124	0.0

The reaction rates used in the RadiCAL input file are given for a reference temperature of 25°C and adjusted to reactor operating conditions using an Arrhenius law.

Convection is represented by the following relationship with respect to liquid or gas phase:

$$V_{g/l}(x)A_{g/l}(x)C_{g/li}(x) - V_{g/l}(x+dx)A_{g/l}(x+dx)C_{g/li}(x+dx) \qquad (2.23)$$

This relationship represents the time dependent change of concentration across the differential volume as a function of concentration gradient, velocity gradient, and cross-

sectional area gradients. The fluid-phase cross-sectional area gradient is a function of both void fraction and total cross-sectional area.

The flux of chemical species between the gas and liquid phases is represented by the following relationship:

$$A_{gl}(x)\left(\phi_i^{g,l} - \phi_i^{l,g}\right) \tag{2.24}$$

This is the difference between the flux into the phase minus the flux out of the phase multiplied by the boundary surface area A_{gl}. These terms are represented by the following equations [2.26]:

$$A_{gl}(x) = \frac{6\alpha}{d_b} A_T(x)dx \tag{2.25}$$

$$\phi_i^{g,l} = k_i^{g,l}\left(C_{li} - aC_{li}\right) \tag{2.26}$$

$$\phi_i^{l,g} = k_i^{l,g}\left(C_{gi} - bC_{gi}\right) \tag{2.27}$$

The constant, 6, divided by the bubble diameter is constant at a given pressure and is incorporated into a new constant along with the rate constant and the constants a and b. These are proportionality constants used to describe the concentration gradient between the bulk fluid and the fluid at the bubble surface. The new constant (μ) is given by the following expression:

$$\mu_i^{l,g} = \frac{6k_i^{l,g}}{d_b}(1-\alpha) \tag{2.28}$$

$$\mu_i^{g,l} = \frac{6k_i^{g,l}}{d_b}(1-\beta) \tag{2.29}$$

These are referred to as the mass transfer constants, with the values used in the model given in Table 2.3.

Table 2.3. Mass Transfer Constant Values for Use in Radiolysis Models [2.25]

	H2	O2
$\mu_i^{l,g}$, gas release factor	30	23
$\mu_i^{g,l}$, gas absorption factor	9.9	12.4

Incorporating the previously described relationships into Equation 2.10 gives the following differential equation for the concentration in the liquid phase:

$$\frac{dC_{li}(x)}{dx} = \frac{1}{V_l(x)}\left\{\begin{array}{l}\left[K_{rad}g_iQ_i + \sum_{j=1}^{NRX} KOEF_{ji}k_j\prod_{m=1}^{3}C_{mi}^{l}(x)\right] \\ -C_{li}(x)\frac{\partial V_l}{\partial x} + \left(\mu_i^{g,l}C_{gi}(x) - \mu_i^{l,g}C_{li}(x)\right)\frac{\alpha(x)}{1-\alpha(x)} \\ +\frac{C_{li}(x)V_l(x)}{1-\alpha(x)}\frac{\partial\alpha(x)}{\partial x} + \frac{C_{li}(x)V_l(x)}{A_T(x)}\frac{\partial A_T(x)}{\partial x}\end{array}\right\} \tag{2.30}$$

Similarly, the differential equation for the gas phase is:

$$\frac{dC_{gi}(x)}{dx} = \frac{-1}{V_l(x)}\left\{\begin{array}{l}C_{gi}(x)\frac{\partial V_g}{\partial x} + \left(\mu_i^{l,g}C_{li}(x) - \mu_i^{g,l}C_{gi}(x)\right) \\ +\frac{C_{gi}(x)V_g(x)}{\alpha(x)}\frac{\partial\alpha}{\partial x} - \frac{C_{gi}(x)V_g(x)}{A_T(x)}\frac{\partial A_T}{\partial x}\end{array}\right\} \tag{2.31}$$

Again, radiolysis and chemical reactions are neglected in the gas phase because the density of gas phase is approximately five percent that of the liquid phase. These two equations describe the concentration of various species produced by radiolysis and chemical reactions.

In addition to these equations, thermal-hydraulics describes the properties of the fluid in the boiling region of the system. Thermal-hydraulic effects are determined using one of two correlations, either Bankoff's or the Chexal-Lellouche [2.7], depending on which input parameters are available.

The void fraction and fluid velocities are calculated using Bankoff's correlation's [2.29]:

$$\alpha(x) = \frac{1}{C_0} \frac{1}{1 + \left(\frac{1-\chi(x)}{\chi(x)} \right) \frac{\rho_v}{\rho_l}} \qquad (2.32)$$

$$\frac{1}{C_o} = 0.833 + 0.0001P(psi)$$

Where χ is the fluid quality and ρ is the density of the phases. The quality of the fluid is a function of the power dissipated in the reactor core [2.26].

$$\chi(x) = \begin{cases} 0, (x < x_b) \\ \frac{q_t}{2h_{fg}} - \frac{h_f - h_i}{h_{fg}} - \frac{q_t}{2h_{fg}} \cos\left(\frac{\pi x}{h_L} \right), (x \geq x_b) \end{cases} \qquad (2.33)$$

$$q_t = h_f + \chi_e h_{fg} - h_i \qquad (2.34)$$

$$x_b = \frac{h_L}{\pi} \cos^{-1}\left(\frac{h_i + \chi_e h_{fg} - h_f}{h_f + \chi_e h_{fg} - h_i} \right) \qquad (2.35)$$

Where i is the value at the core inlet, e is the value at the core outlet, L is the core length, x_b is the point in the reactor where boiling initiates and h is the enthalpy. In addition to solving the void fraction in terms of operational parameters of the primary

system, the expressions that give the gas and liquid velocities in terms of the operating parameters are determined by defining the slip ratio:

$$S(x) = \frac{V_g}{V_l} = \frac{1-\alpha(x)}{\frac{1}{C_0} - \alpha(x)} \tag{2.36}$$

The gas and liquid velocities are calculated from the fluid average velocity using the following equations:

$$\alpha\rho_g V_g + (1-\alpha)\rho_l V_l = \rho_l V_o \tag{2.37}$$

$$V_l = \frac{\rho_l V_o}{\rho_g \alpha S + \rho_l (1-\alpha)} \tag{2.38}$$

$$V_g = SV_l \tag{2.39}$$

The fluid average velocity is given by the definition of mass flow rate in the input to the model:

$$V_o = \frac{\dot{m}}{A_T \rho_l} \tag{2.40}$$

These equations are sufficient to calculate the concentration of chemical species in the regions of the reactor containing two-phase flow: the boiling channel of the core, the upper plenum, and the 2-phase region of the steam separator.

The Chexal-Lellouche correlations [2.7] use the following equations to represent fluid velocities.

$$V_l(x) = \frac{\dot{m}}{A_T(x)\rho_l(x)} \frac{(1-\chi(x))}{(1-\alpha(x))} \tag{2.41}$$

$$V_g(x) = \frac{\dot{m}\chi(x)}{A_T(x)\rho_g(x)\alpha(x)} \tag{2.42}$$

The thermodynamic quantities are calculated using the Chexal-Lellouche thermodynamic subroutines by inputting the initial temperature, pressure, and power input for the 2-phase region.

The electrochemical potential (ECP) and concentration of each species at all points in a reactor coolant loop is determined by computationally traversing each node in the coolant flow path until a specified number of cycles are complete or convergence criteria are met. At each interval along the coolant path the concentration equations, 2.30 and 2.31 are solved. There are **N** simultaneous differential equations to solve, one for each chemical species being considered. To solve these equations the model uses a standardized non-linear differential equation solver, Livermore solver for ordinary differential equations (LSODE). LSODE was developed by Hindmarsh at Lawrence Livermore National Laboratory [2.30].

2.2.2. Modeling of Electrochemical Corrosion Potential

Experimental studies have shown that reducing the ECP to below -230 mV (SHE) will significantly reduce or eliminate intergranular stress corrosion cracking in stainless steel [2.22]. In some previous work, such as a study showing that -230 mV SHE corresponded to an approximate oxygen concentration of 20 ppb, ECP has been described as a function only of oxygen concentration [2.22,2.31]. However, the corrosion potential is due not only to the reduction of oxygen and oxidation of stainless steel, but also to the reduction of hydrogen peroxide and the oxidation of hydrogen. Flow velocity has also

been shown to effect the ECP. A mixed potential ECP model by Lin is used by the RadiCAL model to calculate ECP [2.31].

The corrosion of BWR primary coolant systems is due to the oxidation of hydrogen and stainless steel coupled with the reduction of hydrogen peroxide and oxygen. The equilibrium potentials for each of these reactions are given by the Nernst equation:

$$E = E_0 + \frac{2.3RT}{zF} \log \frac{a_{oxid}}{a_{red}} \tag{2.43}$$

Where E is the cell potential, E_0 is the standard cell potential, R is the universal gas constant, T is the temperature in Kelvin, z is the number of electrons transferred in the reaction, F is Faraday's number, a_{oxid} is the activity of the oxidized species, and a_{red} is the activity of the reduced species.

The cell potential defines the potential at which the forward and reverse reactions are in equilibrium. The corrosion potential and associated corrosion rate can be determined using mixed potential theory. The current densities for all oxidation reactions are summed forming the total oxidation current. The sum of the currents due to multiple reduction species are summed as well. The corrosion potential is the point where the summed oxidation and reduction currents are equal and opposite.

To determine the corrosion potential for a BWR primary system the current associated with each half-cell reaction would have to be determined. Additionally, the effect of fluid flow on the limiting current density of each oxidizing species would be required. Because the determination of these currents by predicting the state of the

system is not practical, an empirical model has been developed from experimental measurements [2.31].

The ECP model used here was developed by measuring ECP under simulated BWR coolant chemistry conditions using a rotating cylinder electrode (RCE) [2.31]. The model developed accounts for fluid velocity, hydrogen concentration, and either oxygen or hydrogen peroxide concentration. There are two ECP values, one for oxygen the other for hydrogen peroxide. The ECP correlation is given by the following equation and is valid for both oxidants:

$$ECP = C_1 \tanh\left[\frac{\log(Conc) - C_2}{C_3}\right] + C_4 \log(Conc) + C_5 \tag{2.44}$$

Where Conc is the oxidant concentration, O_2 or H_2O_2 in ppb and the ECP is relative to the given oxidant in mV (SHE). The five constants determine the shape of the curve using different constants for oxygen and hydrogen peroxide. The constants for the hydrogen peroxide relationship are

$$C_1 = C_5 + 510 \tag{2.45}$$

$$C_2 = 0.00574\left[Conc_{H_2}\right]^{0.772} - 0.00754\sqrt{V_{RCE}} + 0.811 \tag{2.46}$$

$$C_3 = 0.569 \tag{2.47}$$

$$C_4 = 25.33 \tag{2.48}$$

$$C_5 = \frac{-4.62\left[Conc_{H_2}\right]^{0.808}}{e^{0.00280\left[Conc_{H_2}\right]}} + 1.50\sqrt{V_{RCE}} - 192.0 \tag{2.49}$$

and the constants for the oxygen relationship are

$$C_1 = C_5 + 510 \tag{2.50}$$

$$C_2 = 0.00531\left[Conc_{H_2}\right]^{0.772} - 0.0111\sqrt{V_{RCE}} + 1.78 \tag{2.51}$$

$$C_3 = 1.02 \tag{2.52}$$

$$C_4 = 18.7 \tag{2.53}$$

$$C_5 = -18.6\left[Conc_{H_2}\right]^{0.264} - 177.0 \tag{2.54}$$

Where $Conc_{H2}$ is the hydrogen concentration in ppb and V_{RCE} is the velocity of the rotating cylinder electrode. The linear velocity in the BWR primary coolant path is converted to RCE by the following equation:

$$V_{RCE} = 3.01e^{\left[0.425+1.25\ln\left(V_{pipe}\right)-0.179\ln\left(d_{pipe}\right)\right]} \tag{2.55}$$

Once the ECP is calculated for both oxygen and hydrogen peroxide the two are combined to yield one ECP value for the region modeled. This is done by comparing the values for each oxidant and selecting the larger. This value is then used to determine an equivalent concentration of the other oxidant necessary to produce this ECP value (using the other set of constants). Since the ECP model is not an easily invertable function, the equivalent concentration is determined iteratively. The equivalent concentration is then added to the original concentration that yielded the lower ECP value. This new oxidant concentration is then used to calculate a final ECP for the region.

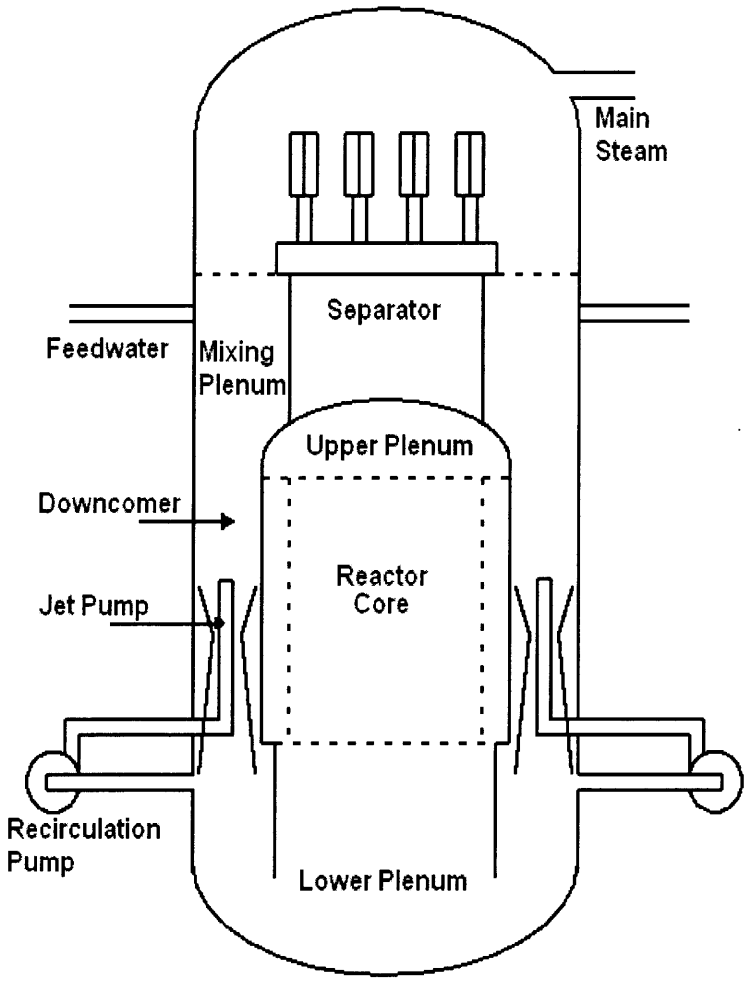

Figure 2.8. Boiling water reactor vessel schematic.

2.2.3. Modeling a Boiling Water Reactor

Boiling Water Reactors (BWR) make up about one third of the nuclear reactors currently operating worldwide [2.6]. The operational parameters of a BWR are a pressure of approximately 7.0 MPa and a temperature of approximately 300°C. In a BWR, the steam that drives the turbine is produced in the reactor vessel. Therefore, BWRs do not require the secondary steam generator loop found in pressurized water reactors (PWR). The direct steam cycle of a BWR simplifies the design and increases the

thermodynamic efficiency. The disadvantage, however, is that the steam, which has passed through the reactor core, contains radioactive gases. This results in higher radiation dose rates in the balance of plant requiring shielding of the piping and turbines.

Figure 2.8 illustrates the major components of a BWR reactor vessel. The outer shell consists of the pressure vessel and the recirculation system. Inside the pressure vessel the core shroud separates the core in the inside and an annular region referred to as the downcomer between the pressure vessel and the shroud. Above the core is the upper plenum, which is capped by the core head dome. The steam separator assemblies are mounted on the core head and the steam dryers are above the separators. The region around the steam separators is referred to as the mixing plenum because it is where the feedwater enters the pressure vessel. The region beneath the core is called the lower plenum. To circulate the water, part of the water flows through the recirculation pumps and is forced through the narrow jet pump region drawing water from the downcomer into the lower plenum.

The flow path of the primary coolant through the BWR pressure vessel and recirculation system begins with the feedwater inlet. The feedwater enters the mixing plenum and mixes with the saturated liquid from the moisture separator. The coolant then enters the downcomer region and passes through the jet pump into the lower plenum. Some fraction of the flow is diverted into the recirculation line to power the jet pump. From the lower plenum the coolant enters the core. In the core, some of the liquid is boiled resulting in a two-phase mixture. The flow continues through the upper plenum and into the moisture separator. The saturated vapor is separated and is transported via

the main steam lines to the turbines and condensers back to the feedwater inlet. The saturated liquid is transported directly to the mixing plenum.

To model chemical concentrations and electrochemical corrosion potential along the BWR flow path, thermal-hydraulic conditions and radiation dose profiles are required. To accurately model the reactor, any region along the BWR primary coolant loop where these parameters change substantially is modeled individually. These individual regions are referred to as components in the RadiCAL model. The model for a BWR-3 type reactor uses 30 components joined at 18 nodes as shown in Figure 2.9.

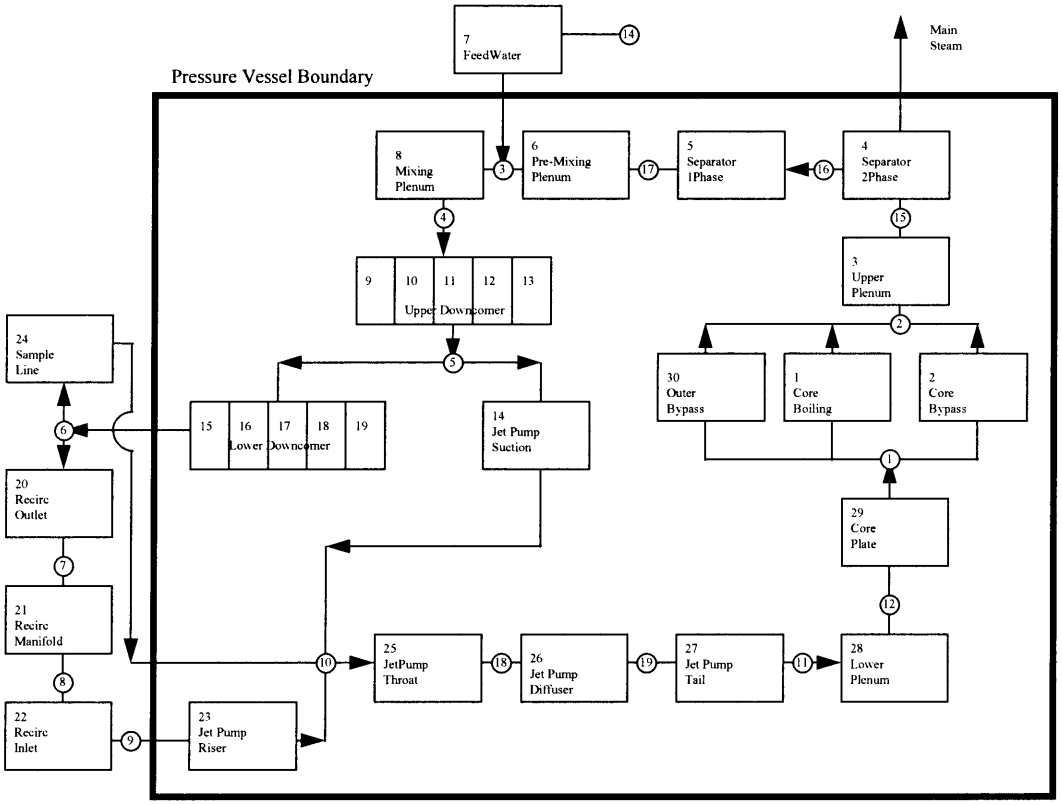

Figure 2.9. BWR Component Schematic [2.7].

The various components correlating to the nodes in Figure 2.9 are shown on the detailed reactor schematic in Figure 2.10.

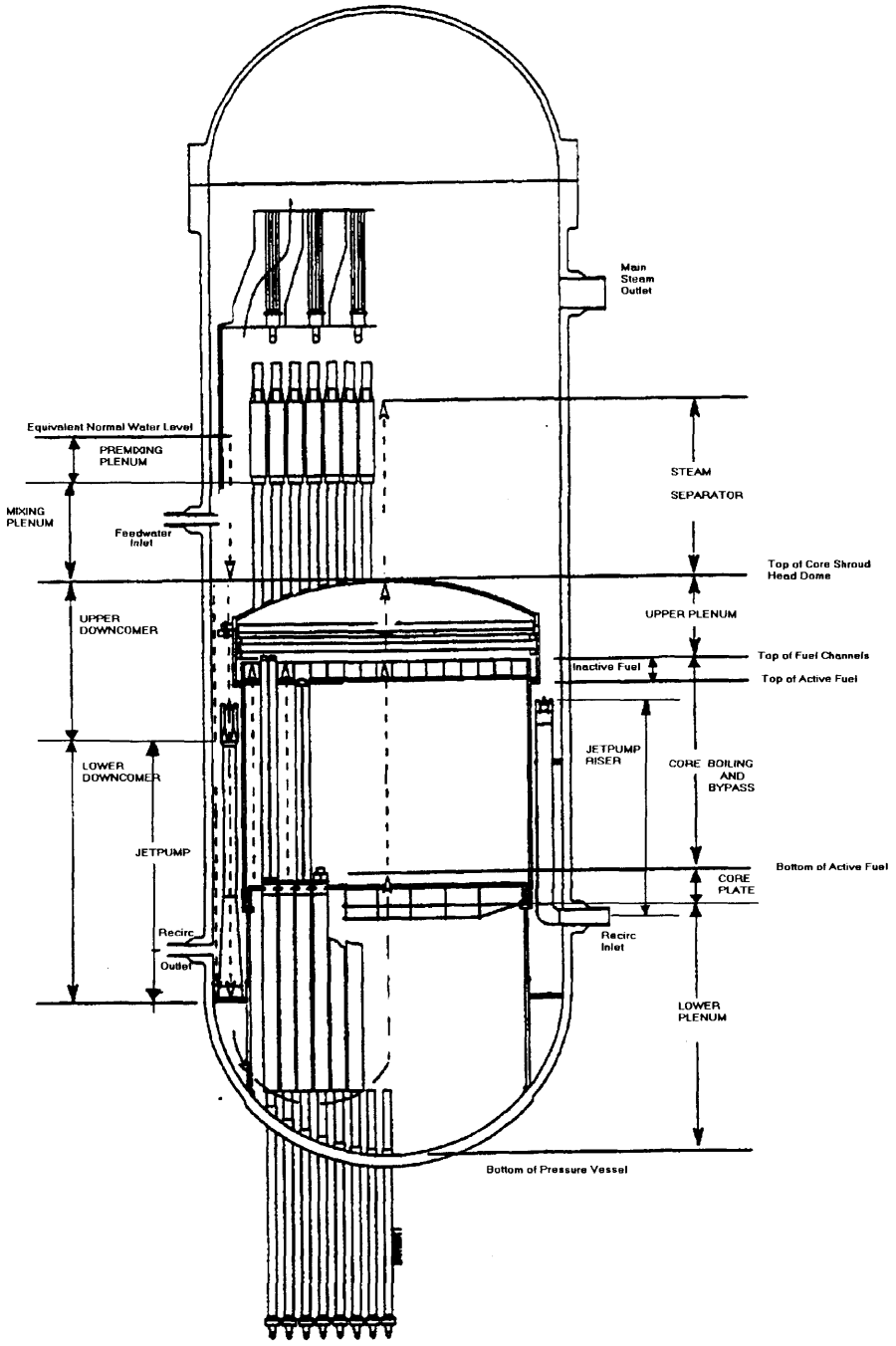

Figure 2.10. Location of Components within the BWR Pressure Vessel

2.3. References

[2.1] Uhlig, H. H., Revie, R. W., Corrosion and Corrosion Control, John Wiley and Sons, Inc. (1985).

[2.2] Gaudett, M.A. and Scully, J.R., Applicability of bond percolation theory to intergranular stress-corrosion cracking of sensitized AISI 304 stainless steel, Metallurgical Transactions A (Physical Metallurgy and Materials Science), Vol. 25A No. 4 (1994) pp. 775-787.

[2.3] Jones, Denny A., Principles and Prevention of Corrosion, Prentice Hall, (1992).

[2.4] Flores, C. D. Evaluation of Radiation Induced Segregation in Fe-Ni-Cr Alloys, M.S. thesis, Nuclear Engineering Department, Massachusetts, Institute of Technology, 1994.

[2.5] Boerigter, S. T., "An Investigation of Neutron-Irradiation Induced Segregation in Austenitic Stainless Steels," ScD theses, Nuclear Engineering Department, Massachusetts, Institute of Technology, 1992.

[2.6] Chun, J. H., "Modeling of BWR Water Chemistry." SM thesis, Nuclear Engineering Department, Massachusetts, Institute of Technology, 1990.

[2.7] Grover, D. J., "Modeling Water Chemistry and Electrochemical Corrosion Potentials in Boiling Water Reactors." SM thesis, Nuclear Engineering Department, Massachusetts, Institute of Technology, 1996.

[2.8] Bruemmer, S. M., Cole, J. I., Brimhall, J. L., Carter, R. D., and Was, G. S., "Radiation Hardening Effects on Localized Deformation and Stress Corrosion Cracking of Stainless Steels," Proceedings of the Sixth International Symposium on Environmental Degradation of Materials in Nuclear Power Systems-Water Reactors, (Aug. 1993) pp. 537-546.

[2.9] Cookson, J. M., Damcott, D. L., Was, G. S., and Andresen, P. L., "Role of Microchemical and Microstructural Effects in the IASCC of High Purity Austenitic Stainless Steels," Proceedings of the Sixth International Symposium on Environmental Degradation of Materials in Nuclear Power Systems-Water Reactors, (Aug. 1993) pp. 573-581.

[2.10] Garner, F. A., Hamilton, M. L., Greenwood, L. R., Stubbins, J. F., and Oliver, B. M., "Isotopic Tailoring with 59Ni to Study Helium Generation Rates and Their Effect on Tensile Properties of Neutron-Irradiated Fe-Cr-Ni Alloys," Effects of Radiation Materials: 16th International Symposium, ASTM STP 1175, (Jun. 1992) pp. 921-939.

[2.11] Elen, J. D., Fenici P., "Fast-Neutron Irradiation Hardening Of Austenitic Stainless-Steel At 250°C," Journal of Nuclear Materials, V. 191, (Sep. 1992) pp. 766-770.

[2.12] Scott, P., "A Review of Irradiation Assisted Stress Corrosion Cracking," Journal of Nuclear Materials, V. 211 N. 2, (Aug. 1994) pp. 101-122.

[2.13] Bruemmer, S. M. and Simonen, E. P., "Radiation Hardening and Radiation-Induced Chromium Depletion Effects on Intergranular Stress Corrosion Cracking in Austenitic Stainless Steels," Corrosion, V. 50 (Dec. 1994) pp. 940-946.

[2.14] Bruemmer, S. M.; Cole, J. I.; Carter, R. D.; Was, G. S., "Defect Microstructures and Deformation Mechanisms in Irradiated Austenitic Stainless Steels," Materials Research Society Symposium Proceedings Microstructure Evolution During Irradiation Proceedings of the 1996 MRS Fall Symposium, V. 439 (Dec. 1996) pp. 437-444.

[2.15] Heinisch, H. L., Hamilton, M. L., Sommer, W. F., and Ferguson, P. D., "Tensile Property Changes of Metals Irradiated to Low-Doses with Fission, Fusion and Spallation Neutrons," Journal of Nuclear Materials, V. 191 (Sep. 1992) pp. 1177-1182.

[2.16] Chung, H. M., Ruther, W. E., Sanecki, J. E., Hins, A. G., and Kassner, T. F., "Stress Corrosion Cracking Susceptibility of Irradiated Type 304 Stainless Steels," Effects of Radiation on Materials: 16th International Symposium, ASTM STP 1175, (Jun. 1992) pp. 851-869.

[2.17] Marmy, P. and Victoria, M., "The Tensile and Fatigue Properties of Din 1.4914 Martensitic Stainless-Steel After 590 Mev Proton Irradiation," Journal of Nuclear Materials, V. 191 (Sep. 1992) pp. 862-867.

[2.18] James, L.A., Ramberg-Osgood strain hardening characterization of an ASTM A302-B steel. Journal of Pressure Cessel Technology, V. 117 N 4 (Nov. 1995) pp. 341-345.

[2.19] Hilton, Bruce A., "Irradiation Assisted Stress Corrosion Cracking Susceptibility of Low Fluence Stainless Steels Evaluated by In-Flux Slow Strain Rate Tests." PhD thesis, Nuclear Engineering Department, Massachusetts, Institute of Technology, 1992.

[2.20] Samuel, K.G., Mannan, S.L., Radhakrichnan, V.M., The Influence of Temperature and Prior Cold Work on the Strain Hardening Parameters of a Type 316 LN Stainless Steel., International Journal of Pressure Vessels and Piping. V. 52, N. 2 (1992) pp.151-157.

[2.21] Simonson, S.A., "Modeling of Radiation Effects of Nuclear Waste Package Materials," Ph.D. Thesis, Department of Nuclear Engineering, Massachusetts Institute of Technology, 1988.

[2.22] Cowan, R. L. et. al., Recent Developments in BWR Water Chemistry Control, 2nd International Topical Meeting on Nuclear Power Plant Themal Hydraulics and Operations, Tokyo, Japan, (1986).

[2.23] Ruiz, C. P. et. al., Modeling Hydrogen Water Chemistry for BWR Applications, EPRI Report NP-6386, (1989).

[2.24] Ibe, E. et. al.; Parameter identification of waste radiolysis in BWR primary systems, Proc. 5th Int. Conf. Water Chemistry of Nuclear Reactor Systems, No. 5 BNES, Bournemouth, England, (1989).

[2.25] Ibe, E., Uchida, S., A Water Radiolysis Model in a Circulating Flow System with a Boiling Region and Its Application to Hydrogen Alternative Water Chemistry of Boiling Water Reactors, Nuclear Science and Engineering, **89**, (1985) pp. 140-157.

[2.26] Ibe, E., Sakagami, M., Uchida, S., Theoretical Model Analyses for Effects of Hydrogen Injection on Radiolysis of Coolant Water in BWR, J. Nuclear Science and Technology, Vol. 23 No. 1, (1986) pp. 11-28.

[2.27] Ruiz, C. P. Modeling Hydrogen Water Chemistry for BWR Applications Program Description and Status, Presentation, (1993).

[2.28] Romeo, G., et. al., BWR Vessels and Internals Project, Modeling Hydrogen Water Chemistry for BWR Applications-New Results (BWRVIP-13), EPRI Report TR-106068, (1995).

[2.29] Todreas, N. E., Kazimi , M. S.; Nuclear Systems I, Hemisphere Publishing Corp., New York, (1990).

[2.30] Hindmarsh, A. C., ODEPACK, A Systematized Collection of ODE Solvers, Scientific Computing, R. Stepleman, ed., North-Holland Publishing Co., (1983) pp.55-64.

[2.31] Lin C. C., Kim, Y.J., Niedrach, L.W., Ramp, K. S., "Electrochemical Corrosion Potential Models for Boiling Water Reactor Applications, Corrosion. Vol. 52 No. 8 (1986) pp. 618-625

[2.32] Rozier, Robert, Modification and Operation of an In-Pile Loop for BWR Chemistry Studies. SM thesis, Nuclear Engineering Department, Massachusetts, Institute of Technology, 1992.

3. Crack Growth Model

In this section of the thesis, the crack growth model, which comprises the core of IEDM, will be discussed. In this chapter, the sources of data used in the model will be discussed and the reason for these choices will be described. Additional information about the choices made for various parameters can be found in the sensitivity section at the end of this chapter.

3.1. Mechanical Aspects of the Crack Tip Strain

3.1.1. Crack tip strain distributions

An essential aspect that sets the crack growth model used in the IEDM apart from other models is the incorporation of a more rigorous determination of the strain distribution at the crack tip. A great deal of effort has gone into the analytical determination of strain functions. Conditions of significance in the continuum theory of cracking include whether the cracks are stationary or growing, whether or not the material experiences strain hardening, and whether the cracking is under plane-stress (thin) or plane-strain (thick) conditions [3.1]. Stress corrosion cracks in nuclear reactors are in plane strain because the dimensions along which cracks grow are thick such as pipes, bolts, etc. The following equations are the analytical distributions for the strain at a distance r from the crack tip under plane-strain conditions [3.2]. Here the plastic strain, ε_p, is given as a function of the plastic zone size, R_p, and the distance from the crack tip, r.

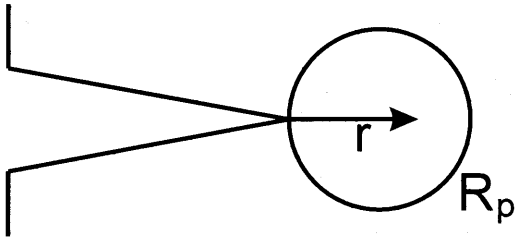

Figure 3.1. Crack tip indicating distance, r, and plastic zone size, Rp.

For stationary cracks, the distribution assuming elastic, ideally plastic conditions is the following:

$$\varepsilon_p = \frac{\sigma_{ys}}{E}\left(\frac{R_p}{r} - 1\right) \tag{3.1}$$

Where σ_{ys} is the yield strength and E is the Young's modulus. With strain hardening this equation becomes:

$$\varepsilon_p = \alpha\frac{\sigma_{ys}}{E}\left[\left(\frac{R_p}{r}\right)^{\frac{1}{n+1}} - 1\right] \tag{3.2}$$

Where α is a constant and n is the strain hardening exponent. For growing cracks and elastic, ideally plastic conditions the analytical strain distribution is the following:

$$\varepsilon_p = \beta\frac{\sigma_{ys}}{E}\left[\ln\left(\frac{R_p}{r}\right)\right] \tag{3.3}$$

Where β is a constant. With strain hardening the following equation applies:

$$\varepsilon_p = \beta\frac{\sigma_{ys}}{E}\left[\ln\left(\frac{R_p}{r}\right)\right]^{\frac{1}{1-n}} \tag{3.4}$$

In the above equations the plastic zone size for plane strain conditions is determined using the following equation:

$$R_p = \frac{K_I^2}{3\pi\sigma_{ys}^2} \tag{3.5}$$

Where K_I is the stress intensity factor for a mode I crack.

Figure 3.2 plots actual experimental data for a crack growing in single crystal Fe-3wt%Si at a stress intensity factor, K=13 MPa/m$^{1/2}$ along with the equations for a stationary crack in strain hardening material and a growing crack in both ideally plastic and strain hardening materials. For the plot, α equals 1, β equals 5.46, σ_{ys} is 270 MPa/m$^{1/2}$, E is 120 GPa, and n is 0.38.

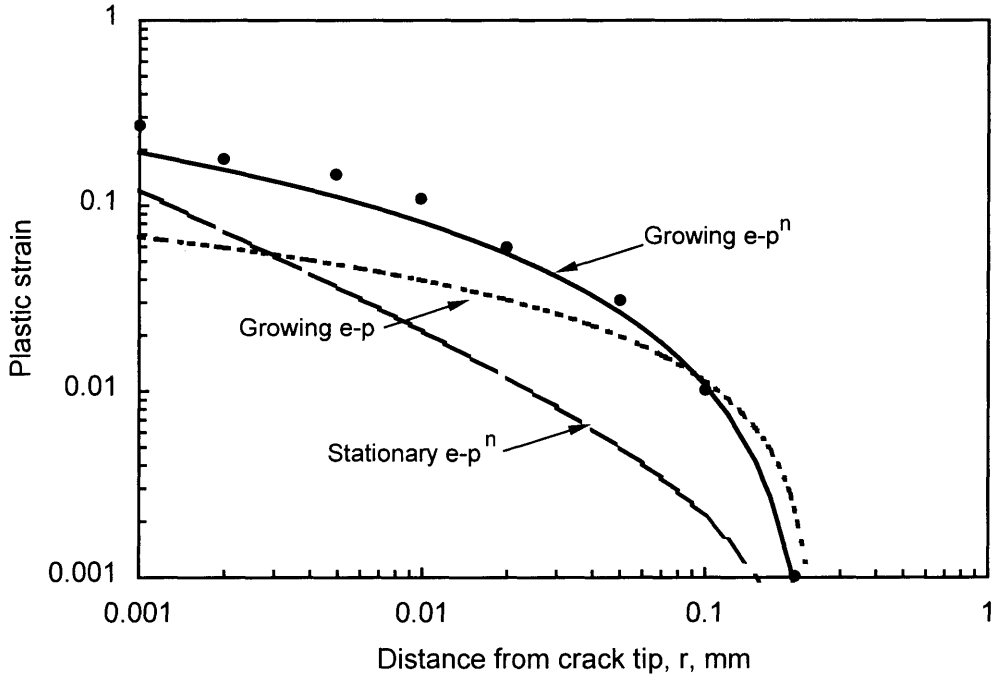

Figure 3.2. Strain distributions for subcritical crack growth measured normal to the crack plane. Points are data from the fatigue of Fe-3wt%Si fatigued in 1 atmosphere dry H2 [3.2].

The analytical distribution for a growing crack in a strain hardening material fits the experimental data well down to within 1μm of the crack tip. Thus the validity of Equation 3.4 is illustrated.

3.1.2. Crack Tip Strain Rate

The crack growth model that is central to the IEDM is advanced because it uses this more accurate strain hardening model for a growing crack originally derived by Gao and Hwang [3.3] and verified experimentally by Gerberich et. al. [3.1]. The following derivation of the crack tip strain rate is similar to that of Shoji et. al. [3.4].

The crack tip strain distribution is for an existing and growing crack. The distribution for a growing crack is chosen because if the crack is not growing we do not need to worry about it. That the crack exists is important as well. We have assumed that a crack has initiated in the metal. Therefore, a failure prediction made with the model is conservative because it ignores the time to initiate a crack. The time to initiate a crack in a defect on the metal surface is likely to be short compared to the design life of the component [3.5]. Therefore, this model assumes that a crack has already been initiated and attempts to find the conditions where propagation will occur and the rate at which the crack will propagate.

We begin with the analytical strain distribution for a growing plane strain crack with strain hardening [3.1]:

$$\varepsilon = \beta \frac{\sigma_y}{E} \left[\ln\left(\frac{R_p}{r} \right) \right]^{\frac{1}{1-n}} \tag{3.6}$$

Where β is a dimensionless constant between 4.3 and 5.8, accepted to be 5.5 [3.1]. R_p is the plastic zone size for a plane strain crack:

$$R_p = \frac{1}{3\pi}\left(\frac{K}{\sigma_y}\right)^2 \tag{3.7}$$

K is the stress intensity factor at the crack tip, equal to the plane tensile stress at the crack tip, σ, multiplied by the square root of the crack length, a, times π:

$$K = \sigma\sqrt{\pi \cdot a} \tag{3.8}$$

To determine the crack tip strain rate we must find the time derivative of the crack tip strain. The derivative is found noting that the strain is a function of stress intensity factor, K, and distance, r, and the K is a function of the stress, σ, and the crack length, a.

$$\frac{d\varepsilon}{dt} = \frac{d\varepsilon}{dK}\cdot\frac{dK}{d\sigma}\cdot\frac{d\sigma}{dt} + \frac{d\varepsilon}{dK}\cdot\frac{dK}{da}\cdot\frac{da}{dt} + \frac{d\varepsilon}{dr}\cdot\frac{dr}{dt} \tag{3.9}$$

First, the equation is simplified by assuming that the stress is not changing significantly. Therefore, the equation becomes the following:

$$\frac{d\varepsilon}{dt} = \frac{d\varepsilon}{dK}\cdot\frac{dK}{da}\cdot\frac{da}{dt} + \frac{d\varepsilon}{dr}\cdot\frac{dr}{dt} \tag{3.10}$$

Figure 3.3 illustrates the relationship between the crack length, a, and r. It is clear from the figure that for a time step, dt, the change in length, r, is the opposite of the change in length, a.

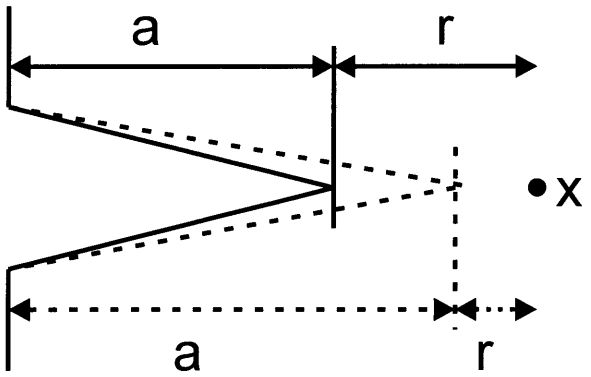

Figure 3.3. Illustration of relationship between crack length and the distance r to some point in the material.

Therefore, the following equation applies:

$$\frac{da}{dt} = -\frac{dr}{dt} \tag{3.11}$$

Which simplifies Equation 3.10 to:

$$\frac{d\varepsilon}{dt} = \left(\frac{d\varepsilon}{dK}\cdot\frac{dK}{da} - \frac{d\varepsilon}{dr}\right)\cdot\frac{da}{dt} \tag{3.12}$$

This equation can be solved analytically by taking the derivative of the crack tip strain distribution in terms of K and r. The first term is the following:

$$\frac{d\varepsilon}{dK}\cdot\frac{dK}{da} = -2\cdot\beta\frac{\sigma_y}{E}\cdot\frac{1}{K(n-1)}\left[\ln\left(\frac{\frac{1}{3\cdot\pi}\left(\frac{K}{\sigma_y}\right)^2}{r}\right)\right]^{\frac{n}{1-n}}\cdot\frac{dK}{da} \tag{3.13}$$

The second term is simply the derivative of the strain with respect to r:

$$\frac{d\varepsilon}{dr} = \beta \frac{\sigma_y}{E} \cdot \frac{1}{r(n-1)} \left[\ln \left(\frac{\frac{1}{3 \cdot \pi} \left(\frac{K}{\sigma_y} \right)^2}{r} \right) \right]^{\frac{n}{1-n}} \tag{3.14}$$

Combining like terms from these last two equations (3.13 and 3.14) and multiplying by da/dt gives a relationship for the rate of change of strain with time at some point a distance r from the crack tip:

$$\frac{d\varepsilon}{dt} = \beta \frac{\sigma_y}{E} \cdot \frac{1}{n-1} \cdot \left[\ln \left(\frac{\frac{1}{3 \cdot \pi} \left(\frac{K}{\sigma_y} \right)^2}{r} \right) \right]^{\frac{n}{1-n}} \left(-2 \cdot \frac{1}{K} \cdot \frac{dK}{da} - \frac{1}{r} \right) \frac{da}{dt} \tag{3.15}$$

Moving the negative sign out of the last terms and reversing 1-n to n-1:

$$\frac{d\varepsilon}{dt} = \beta \frac{\sigma_y}{E} \cdot \frac{1}{1-n} \cdot \left[\ln \left(\frac{\frac{1}{3 \cdot \pi} \left(\frac{K}{\sigma_y} \right)^2}{r} \right) \right]^{\frac{n}{1-n}} \left(2 \cdot \frac{1}{K} \cdot \frac{dK}{da} + \frac{1}{r} \right) \frac{da}{dt} \tag{3.16}$$

Representing derivatives with respect to time with a dot over the variable and distributing da/dt:

$$\dot{\varepsilon} = \beta \frac{\sigma_y}{E} \cdot \frac{1}{1-n} \cdot \left[\ln \left[\frac{1}{3 \cdot \pi} \cdot \left(\frac{K}{\sigma_y} \right)^2 \right] \right]^{\frac{n}{1-n}} \left(2 \frac{\dot{K}}{K} + \frac{\dot{a}}{r} \right) \tag{3.17}$$

This is the equation for the strain rate for a growing crack. To find the stress intensity factor at the tip of crack the crack length and tensile stress must be known. Either the stress condition at the position of the reactor being studied must be provided as an input to the model or some reasonable stress can be assumed.

3.1.3. Sources of Data for Crack Tip Train Rate

In this section the reasons for the particular value assigned to each variable in the crack tip strain rate relationship is described. Some of these reasons are also revisited when the sensitivity of each variable is discussed subsequently.

The first term, β, is the proportionality constant of the analytical strain distribution for a growing plane strain crack. Because there are other uncertain values in the equation it is difficult to use a fit to data to find a reasonable value for β. Values for beta have ranged from 4.28 [3.6] to 5.81 [3.7]. Gerberich determined that the most accepted value is 5.46 [3.2]. Here the beta value chosen is 5.5 to avoid a false sense of accuracy cause by using three significant digits

The proportionality constant for the plastic zone size for plane strain, is given as $1/(3\pi)$ as by Gerberich [3.1]. However, this value, known as lambda for simplicity in other parts of this paper, could vary based on different representations of the plastic zone size for different cracking modes. Like beta, lambda is kept constant because the certainty of other parameters is not sufficient to allow calibration.

The next term is the ratio of yield strength, σ_y, to elastic modulus or Young's modulus, E. The elastic modulus is a constant for the metal. In the user interface, E can be supplied to the user based on a choice of default metals, or the user can supply it to the

model. The default elastic modulus used here for stainless steel 304 is 22000 kg/mm^2. The yield strength can be supplied by the user, a default value can be used (annealed only) or it can be determined by the hardening model. The hardening model uses the same default annealed value or a value supplied by the user, and calculates the contribution from radiation hardening. The default yield strength for annealed SS 304 is 20 kg/mm^2. For other common metals that undergo irradiation assisted stress corrosion cracking data is compiled in Table 3.1.

Table 3.1. Approximate Properties of Austenitic Materials [3.8]

AISI Type	SS 304	SS 316	SS 347	Inconel 600
Yield strength (kg/mm^2)	21	21	21	32
Modulus of elasticity (kg/mm^2)	20000	20000	20000	21700

The strain hardening exponent, n, defines the extent to which a material work hardens as it is being strained. As the yield strength increases due to cold work or irradiation hardening, the strain hardening exponent decreases. The strain hardening exponent, n, can also be determined by the user, the default metal choice, or the radiation hardening model. If it is determined by the hardening model, the value will be between 0.38 and 0.05 depending on the yield strength. For annealed materials the default value is 0.33. This value was chosen because of good fit with experimental data (subsequent section).

The stress intensity factor, K, and its rate of change, K', must be input by the user. $K \propto \sigma\sqrt{\pi a}$, where σ is the far field stress and 'a' is the crack length. This equation represents proportionality but the constant is nearly one in the cracking mode likely to be found here [3.9]. It might appear that the model would better define the crack using

inputs for the crack length and stress. However, for actual reactor condition it is no easier to make assumptions about the stress than it is to make assumptions about the stress intensity factor. Likely values for K are between 30 and 150 $kg/mm^{3/2}$. Many experiments have been conducted at 88.6 $kg/mm^{3/2}$ (25 ksi $in^{1/2}$) [3.9-3.11].

Using the model on actual measured data revealed the importance of the stress intensity factor rate of change and the term that relates it to K (K'/K). Without this term added to the term a'/r, the crack growth model overpredicts high crack growth rates and underpredicts low crack growth rates. This occurs because the crack growth rate is a variable in the crack tip strain rate equation and vice versa. The stress intensity factor rate of change, K', that best fits the data used to verify the crack growth model is 0.0001 $kg/mm^{3/2}s$.

The distance from the growing crack tip, r, represents the position where the crack tip strain is defined and evaluated [3.12] Put differently, the strain at the crack tip acts over some portion of the material at the crack tip whose characteristic length is r. The choice of r determines the magnitude of the crack tip strain. Therefore, this value is chosen such that the value for the crack tip strain produces accurate results for the crack growth rate. The value for r is best determined **last**, after all the other values are correct and reasonable. For the data used to verify the crack growth model, the best fit was attained with r = 0.04mm.

3.2. Slip Dissolution/Film Rupture Model

Previous work by Ford and Andresen [3.9-3.11] and others has shown that crack advance in austenitic stainless steels at anodic potentials can be modeled accurately by the

slip dissolution/ film rupture mechanism. In this mechanism, the local buildup of stress at the crack tip results in rupture of the passive film. Following this rupture event, the exposed metal repassivates replacing the film at the crack tip. During repassivation, some metal at the crack tip is consumed by oxidation. The rate at which oxidation occurs, decreases exponentially as the film thickness increases to steady state. This dissolution of the metal at the crack tip results in crack advance. Following formation of the new passive film at the crack tip, local stresses begin to build up leading to film rupture at the crack tip. This cyclical process continues as long as conditions are appropriate for cracking.

For a passive film to form on the surface of a crack the electrochemical potential of the aqueous solution must fall within a certain range. Species in the water that affect this potential include ions such as metals and halides and radiolysis products such as hydrogen, oxygen, and hydrogen peroxide. The radiolysis products are formed when water molecules are broken apart by ionizing radiation.

Crack propagation by the slip dissolution mechanism results from a combination of anodic dissolution and stress/strain conditions that result in dislocation motion [3.13]. Dislocations at the crack tip cause the protective film to separate at the crack tip exposing bare metal to the environment. During rapid anodic dissolution of the bare metal a new passive film is formed where dislocations can again pile up. Two slightly different mechanisms describe the rupture of the passive film. In cross slip, slip bands emanating from the crack tip result in exposure of the underlying metals. For brittle fracture of the film, dislocations pile up behind the passive film until it ruptures exposing the bare metal beneath. The former case is more likely when the passive film is thin and coherent with the underlying matrix. The latter case will occur for a thick incoherent passive film. The

dislocations result from a monatonically increasing stress, a cyclic stress, or creep resulting from a high constant stress. Experimental results have supported the slip dissolution model because the dissolution rate of bare metal has correlated with the SCC propagation rate in a wide range of materials [3.11]. Both methods of brittle film separation are illustrated in Figure 3.4.

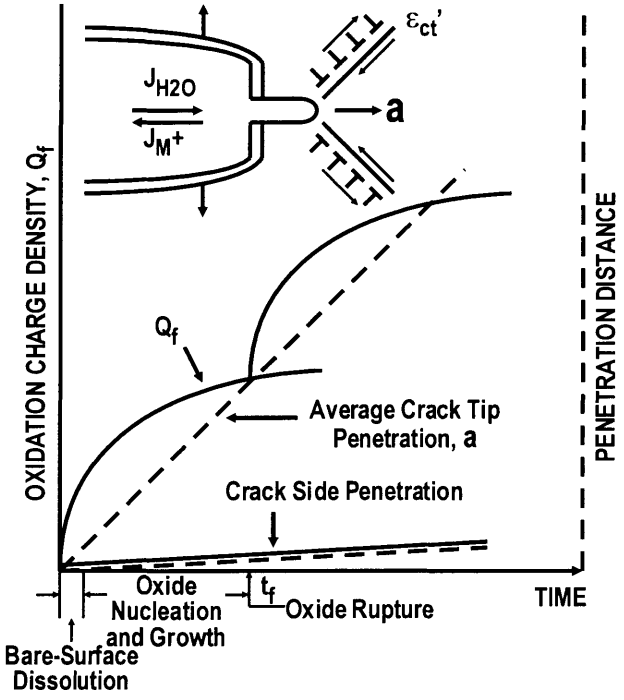

Figure 3.4. Schematic of slip dissolution/ film rupture mechanism and oxidation charge density versus time [3.13]

In Figure 3.4, the equations that will be discussed subsequently are displayed graphically. Q_f is the dissolution charge density. It represents the rate of current and decreases as the passive film forms at the crack tip. The two curves, Q_f, represent the flow of current during each film rupture and repassivation event. Additionally, the top of the diagram shows how plasticity (the motion of dislocations) contributes to film rupture at the crack tip. The slip dissolution/film rupture mechanism for stress corrosion cracking occurs because the thermodynamically stable oxide film ruptures due to strain

concentrations at the crack tip. The crack advance rate is governed by the rate of oxidation of the surface exposed by the fracture of the film, the rate of formation of the new film (repassivation), and the time required for the crack tip strain rate to rupture the oxide film [3.14]. Faraday's law is used to define the crack growth rate in terms of the metal dissolution rate:

$$a' = \frac{M}{z \cdot \rho \cdot F} \cdot \frac{Q_f}{t_f} \tag{3.18}$$

Where M is the atomic mass of the metal, z is the charge quantity of the dissolution process, ρ is the metal density, F is Faraday's constant, Q_f is the dissolution charge density passed during t_f, a period of film rupture [3.11]. The period of film rupture can be found by dividing the fracture strain of the film, ε_f, by the crack tip strain rate, ε'_{ct}:

$$t_f = \frac{\varepsilon_f}{\varepsilon'_{ct}} \tag{3.19}$$

Thus the slip dissolution/film rupture model is described by the following equation.

$$a' = \frac{M}{z \cdot \rho \cdot F} \cdot \frac{Q_f}{\varepsilon_f} \varepsilon'_{ct} \tag{3.20}$$

Another model has been developed that has been described as a combination of the slip dissolution model and the brittle film fracture model [3.11]. In this model, the brittle film is ruptured as the stress at the crack tip increases due to the motion of dislocations. The release of energy associated with rupture of the brittle film results in the cleavage of the underlying metal matrix. The vertical portion of the solid line in

Figure 3.5 represents the cleavage component of crack advance, C. Following this cleavage the underlying metal matrix may undergo rapid anodic dissolution as in the slip dissolution model or may quickly repassivate. If the film forms quickly with little crack advance caused by dissolution, the rate of crack advance will be controlled by the cleavage event. In this situation, the solid line in Figure 3.5 will look like steps because the bare surface dissolution component would be nearly horizontal on the plot indicating little crack advance. The amount of cleavage induced in the bulk metal is affected by the coherency between the film and the metal matrix, the thickness and ductility of the film, and the bond strength at the film-metal interface.

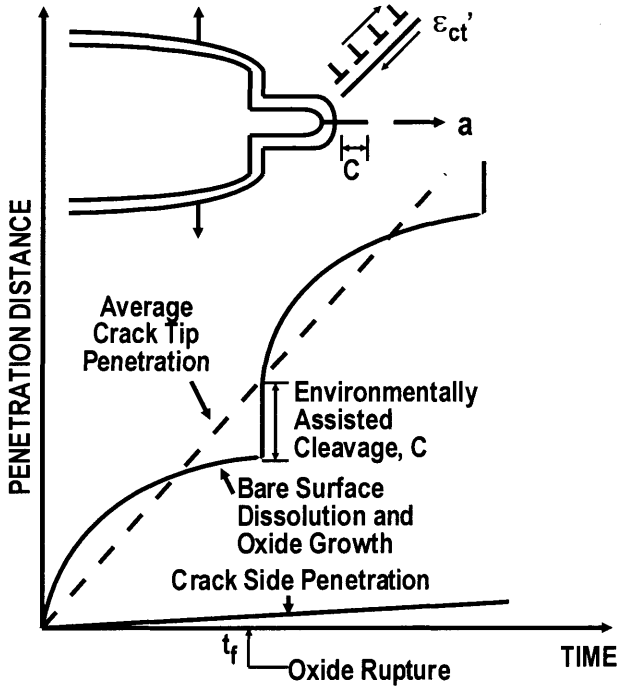

Figure 3.5. Schematic of film induced cleavage mechanism and penetration distance versus time [3.14]

Equation 3.21 is similar to Equation 3.20 but includes the effect of an additive cleavage term, C.

$$a' = \left(\frac{M}{z \cdot \rho \cdot F} \cdot Q_f + C \right) \frac{\varepsilon'_{ct}}{\varepsilon_f} \tag{3.21}$$

The film-induced cleavage model is mentioned here because it is well suited for the integration of multiple crack growth models. When the additional component of environmentally assisted cleavage, C, is equal to zero the cleavage model becomes the slip dissolution/film rupture model. Alternatively, the cleavage of the underlying matrix can dominate the crack growth. Here a novel approach is taken by correlating the magnitude of the cleavage term C, with the level of hydrogen embrittlement predicted to be present in the metal matrix at the crack tip. With the cleavage controlled by hydrogen embrittlement, the additional C term can be determined from cathodic measurements.

In order to determine Q_f, the current passed during the dissolution and repassivation process must be determined. As the film forms at the crack tip it becomes thicker and the rate of oxidation of the underlying metal decreases exponentially. The following equation gives the oxidation current, i(t), at time t as it decreases from a maximum current, i_o [3.14]:

$$i(t) = i_o \left(\frac{t}{t_o} \right)^{-m} \tag{3.22}$$

Where i_o is the oxidation current of the bare surface of the metal, t_o is formation time constant of the passivation film, and m is the slope of the current decay curve. The shape of this equation is shown in Figure 3.6 for times greater than 0.1 seconds.

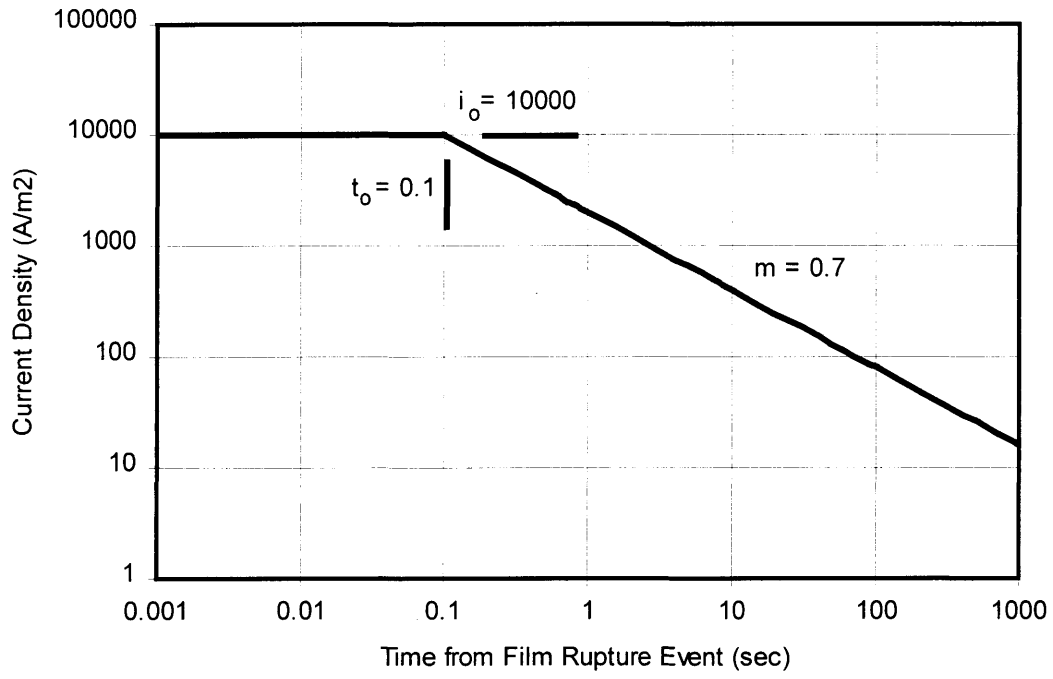

Figure 3.6. Current density versus time example plot.

The total dissolution charge density, Q_f, is equal to the area underneath the curve in Figure 3.6. Up to t_o, the area simply equals the product of i_o and t_o. Above t_o, the area equals the integral of Equation 3.22 from t_o to the time of next rupture event t_f.

$$Q_f = i_o \cdot t_o + \int_{t_o}^{t_f} i(t)dt \tag{3.23}$$

$$Q_f = i_o \cdot t_o + \frac{i_o \cdot t_o^m}{1-m}\left[\left(\frac{\varepsilon_f}{\varepsilon'_{ct}}\right)^{1-m} - t_0^{1-m}\right] \tag{3.24}$$

Notice that the ratio of film rupture strain, ε_f, to crack tip strain rate, ε'_{ct}, is equal to the final time. The model must then be simplified for low crack growth rates. Low crack growth rate means the ratio of the passivation film rupture strain to the crack tip

strain rate of change is much greater than the time to begin repassivating the crack tip ($\varepsilon_f/\varepsilon`_{ct} >> t_o$). The current decay constant is the time at which crack tip repassivation begins. This value has been found experimentally to be close to 0.1 seconds. This simplification is valid and necessary because the slip dissolution / film rupture model is not meaningful if the strain is so high that the crack tip advances continuously. This results in the following:

$$Q_f = i_o \cdot t_o + \frac{i_o \cdot t_o^m}{1-m}\left(\frac{\varepsilon_f}{\varepsilon'_{ct}}\right)^{1-m} \tag{3.25}$$

Substituting Q_f back into the Equation (3.21) for Faraday's law results in the rate of advance of the crack tip, a':

$$a' = \left(\frac{M}{z \cdot \rho \cdot F}\left(i_o \cdot t_o + \frac{i_o \cdot t_o^m}{1-m}\left(\frac{\varepsilon_f}{\varepsilon'_{ct}}\right)^{1-m}\right) + C\right)\frac{\varepsilon'_{ct}}{\varepsilon_f} \tag{3.26}$$

3.2.1. Sources of Data for Crack Tip Train Rate

In this section, the reasons for the selection of each particular variable in Equation 3.26 are described. The variables come from three sources. They are either known properties of the system, experimentally obtained values, or values received from model upstream to the crack growth model. Some of the reasons for selecting certain values are also revisited when the sensitivity of each variable and the validity of the models are discussed subsequently.

Faraday's constant, F, is the charge of one mole of electrons: 96485 Coulombs/ mole. Using Faraday's constant, the metal's atomic mass, M, oxidation state, z, and

density, ρ, the volume of material removed per Coulomb of current transferred at the crack tip can be determined. Table 3.2 gives the values of these three parameters for some common austenitic alloys [3.8].

Table 3.2. Properties of austenitic materials. Data in parenthesis is the value used for the base case or as defaults in the model [3.8]

AISI Type	SS 304	SS 316	SS 347	Inconel 600
Atomic mass (g/mol)	55.9-56.1 (56)	56.6-57.2 (57)	55.3-55.5	58
Oxidation state	2.18-2.20 (2)	2.16-2.18 (2)	2.17-2.19	2.16
Density (kg/m^3)	~7900 (8000)	~8000 (8000)	7900	8500
Fe content (wt.%)	Balance (72)	Balance (71)	Balance	8
Ni content (wt.%)	8-11 (10)	10-14 (12)	9-12	Balance
Cr content (wt.%)	18-20 (18)	16-18 (17)	17-19	16
Other content (wt.%)		2-3 Mo	~1 Nb	1 Mn, 2-3 Mo

The values used for the base case for SS 304, M = 56g/mol, z = 2, r = 8000, are reasonable based on this data. Rounding z to 2 may seem like an unnecessary simplification. However, the oxidation state is not certain because the stoichiometry of dissolution is not known accurately. Additionally, cracking occurs at the grain boundary because of chromium depletion. Therefore, even if dissolution has the same stoichiometry as the metal, the oxidation state will be higher because the material at the crack tip has less chromium.

The passive film rupture strain, ε_f, has been reported with values ranging from 0.001 to 0.015 [3.15]. In the crack growth model used here, a value of 0.007 is used for the chromium rich passive film that protects austenitic Fe-Ni-Cr alloys. This value was measured experimentally for type 304L stainless steel at 288°C in high purity water [3.15].

The time constant for current decay, t_o, is the time at which the passive film begins to form at the crack tip decreasing the current density. In Figure 3.6, this value is found at the position where the slope of the current decay curve changes from 0 to –m. For most experimentally determined current density versus time curves, t_o is approximately 0.1 seconds. This value is used in this model.

The oxidation current density of the bare surface, i_o, is a parameter which can be satisfactorily determined from corrosion theory. As has been described in previous sections, stainless steels form a protective passive layer above a critical potential. However, when the passive film is ruptured at the crack tip the metal momentarily acts as though it is not passivating. For high potentials, oxidation will initially occur at the limiting current density as the metal begins to repassivate. The two reduction half-cell reactions that result in oxidation of the metal are listed here along with their reversible potentials for a neutral solution:

$$H_2O_2 + 2H^+ + 2e^- \rightarrow 2H_2O \qquad 1776 \text{ mV (SHE)} \qquad (3.27)$$

$$O_2 + 2H_2O + 4e^- \rightarrow 4OH^- \qquad 820 \text{ mV (SHE)} \qquad (3.28)$$

The limiting current density can be found using the following equation [3.16]:

$$i_L = \frac{D \cdot z \cdot F \cdot C_B}{\delta} \qquad (3.29)$$

Where D is the diffusivity of the reacting species (cm^2/s), z is the oxidation state change, or number of equivalents exchanged, F is Faraday's number (96,500 C/mol), C_B is the bulk concentration of the reacting species (mol/liter), and δ is the diffusion layer thickness (dm). Decimeters are used for the diffusion layer so that the resulting units for

the limiting current density are A/m^2. At 300°C, the diffusivity, D, for either O2 or H2O2 is 0.0004 cm^2/s [3.17]. The number of equivalents exchanged is 4 for the O_2 reaction and 2 for the H_2O_2 reaction. In the BWR coolant system, the concentration of O2 varies between 3 and 6 x 10^{-6} mol/liter and the H2O2 varies between 3 and 10 x 10^{-6} mol/liter. The boundary layer thickness, δ, is approximately 0.01 cm [3.18]. Assuming an oxygen concentration of 4 x 10^{-6} mol/liter, the limiting current density for O2 is 0.6 A/m^2. Assuming an H2O2 concentration of 6 x 10^{-6} mol/liter, the limiting current density for H2O2 is 0.5 A/m^2. Summing these two values gives a limiting current density for the oxidation of the metal: 1 A/m^2. This represents the maximum rate of electrons consumed by the reduction of oxygen and hydrogen peroxide. Electrons produced by the anodic dissolution of the metal must be consumed by oxidation. Therefore, this places a limit on the dissolution rate of the metal based on a current balance with the reduction rate.

While reduction of oxygen and hydrogen peroxide can occur anywhere on the crack walls or outer surface, oxidation of the metal is occurring predominantly at the crack tip where the passive film is ruptured. Therefore, the area over which the reduction is occurring is much larger than the area at the crack tip. The limiting current density for the crack tip is based on the limiting current of the reducible species because at the crack tip, when the surface is bare, there is no scarcity of available metal atoms to oxidize. The current at the anode must balance with that at the cathode. Therefore, the current densities must differ by the area ratio between the anode and cathode. The crack wall and relevant external surface areas are between 1000 and 10,000 times the area of the crack tip. Therefore, the limiting current density at the crack tip is 1000 to 10,000 times the limiting current density of the cathodic reaction. Experimental verification of the model

has determined that a factor of 10,000 is most appropriate for stress corrosion cracks. Therefore, the limiting current density at the crack tip is 10,000 A/m^2.

The anodic half-cell reactions are the dissolution of iron, nickel, and chrome. The following is a list of these reactions and their reversible potentials.

$$Fe \rightarrow 2e^- + Fe^{2+} \qquad -440 \text{ mV (SHE)} \qquad (3.30)$$

$$Ni \rightarrow 2e^- + Ni^{2+} \qquad -250 \text{ mV (SHE)} \qquad (3.31)$$

$$Cr \rightarrow 2e^- + Cr^{2+} \qquad -744 \text{ mV (SHE)} \qquad (3.32)$$

In order to find the reversible potential for stainless steel, these three potentials must be combined based on stoichiometry of the metal. For stainless steel 304 with 18% chrome and 10% nickel the reversible potential is -475 mV SHE. At the crack tip, grain boundary segregation will have resulted in nickel enrichment and iron and chromium depletion. This results in a reversible potential of about -450 mV SHE. At this potential, the current density of the metal dissolution is at the exchange current density: 10^{-2} A/m^2. This current increases with rising potential along the Tafel slope until the limiting current density is reached. The following plot indicates how the current densities change.

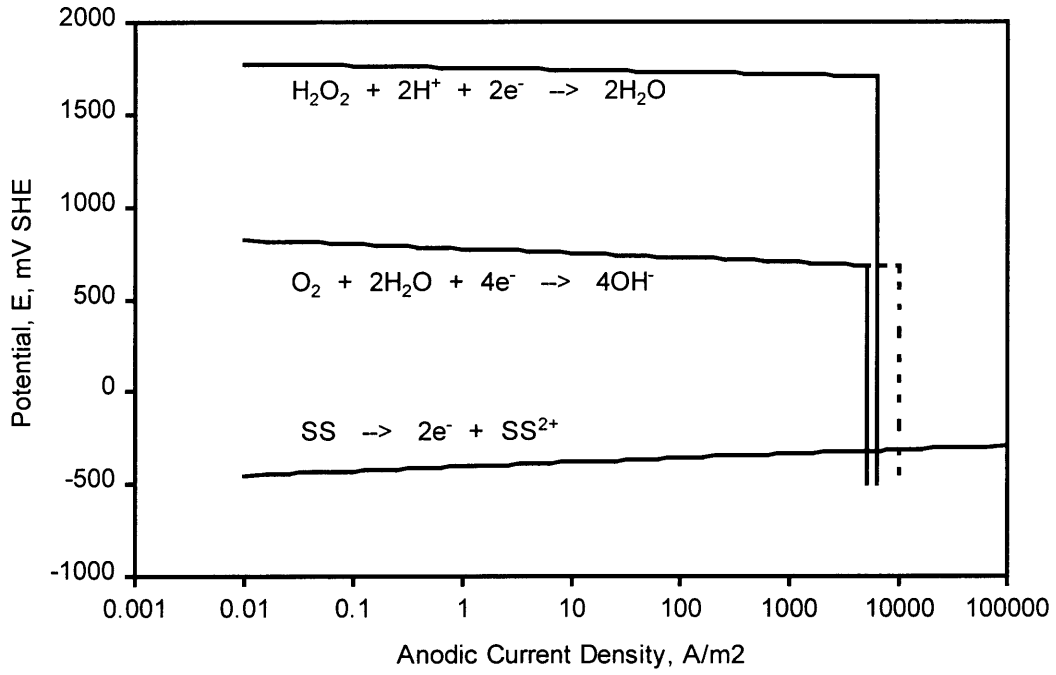

Figure 3.7. Current density versus potential for oxygen, hydrogen peroxide and stainless steel half cell reactions.

The Tafel region of the curve is defined by the following equation:

$$\eta = \beta \log\left(\frac{i}{i_o}\right) = \frac{RT}{\alpha zF} \log\left(\frac{i}{i_o}\right) \tag{3.33}$$

Where R is the universal gas constant, T is the temperature in Kelvin, z and F are as above and α is the transfer coefficient. The transfer coefficient is approximately unity. At a temperature 561K, the oxygen half cell reaction has a Tafel slope of 24.2 mV, the H_2O_2 half cell reaction has a Tafel slope of 12.1 mV and the stainless steel half cell reaction has a Tafel slope of 22.6 mV. The Tafel slopes of the cathodic reactions are not needed here because the limiting current density is reached at potentials much higher than that encountered in BWR coolant systems. The tafel slope for stainless steel is approximately 25 mV per decade. A closer look at the intersection of the stainless steel

current potential relationship and the limiting current density provides the final information to completely characterize the bare surface current density.

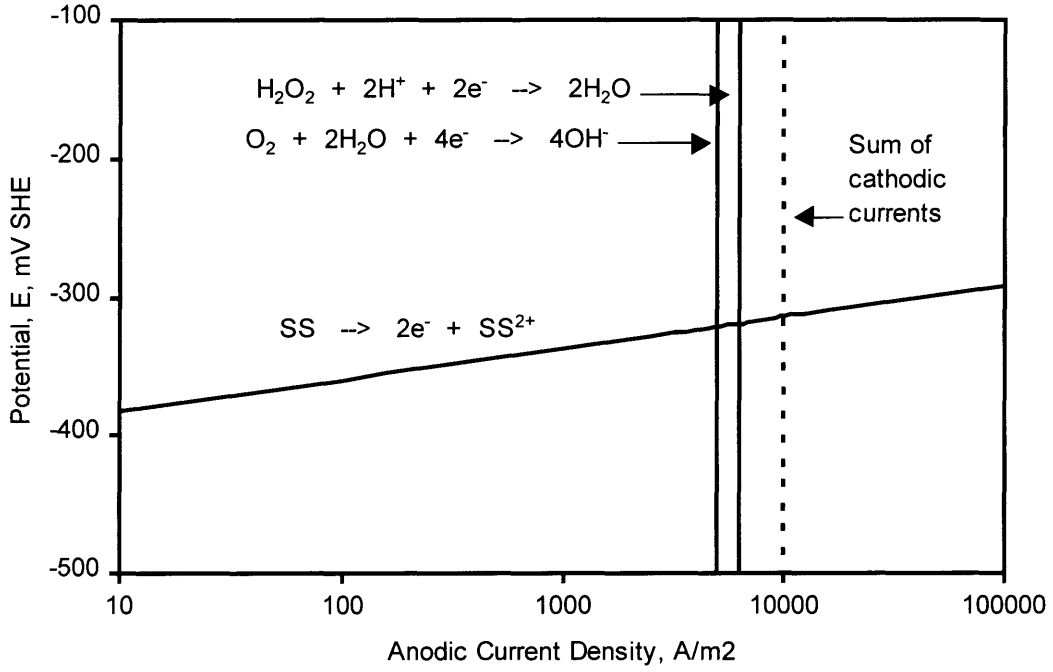

Figure 3.8. Current density versus potential for oxygen, hydrogen peroxide and stainless steel half cell reactions indicating intersection of total cathodic and anodic currents.

Therefore the current density rises between -450 and -300 and then is fixed at the limiting current density for the remainder of the potential range.

Revisiting the choice of 10,000 as the ratio between the anode and the cathode area, we refer to crack growth rate data. Figure 3.9 is a plot of data where the crack tip strain rate is known [3.19]. In this case, only the slip dissolution/film rupture model is being used. In Equation 3.26, all the values are known as described above except the current decay curve slope, m , and the bare surface oxidation density, i_o. The current decay curve slope is found, using the correlation described in the next section, to be 0.47.

The bare surface oxidation density, i_o, was then found to be 10000 A/m2 for the best fit to the data.

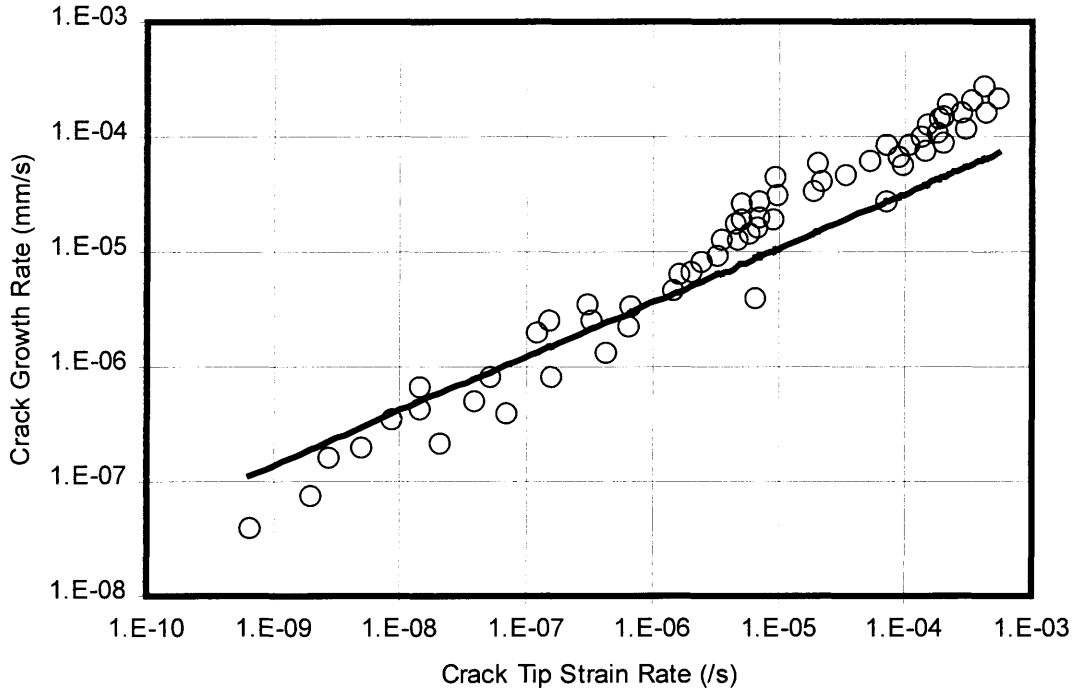

Figure 3.9. Crack tip strain versus crack growth rate for sensitized sstainless steel at high conductivity and high potential [3.19].

The sources of the remaining values, the current decay curve slope and the hydrogen embrittlement cleavage factor, are described in the next two sections. First, the current decay curve slope correlation is described. Then the implementation of hydrogen embrittlement used here is described.

3.2.2. Current Decay Curve Correlation

The slip dissolution/film rupture model is based on the repetitive cracking and repassivation at the crack tip. Each electrochemical parameter required for the crack growth model is part of the current decay curve. However, the decay of current cannot be

modeled deterministically because there is no clear understanding (much less theoretical basis) for passivation kinetics as a function of the water and metal chemistry at the crack tip [3.20]. Thus, measurements must be made to determine the effect of solution chemistry and metal properties on the rate at which the exposed metal is passivated. These experiments are conducted by rapidly stressing wires to break the passive film, or by rapidly changing the polarization from a very low potential where corrosion does not occur to the potential for which passivation is being investigated. From these tests the time constant, current constant and the slope of the current decay curve can be determined. As mentioned previously the time constant, t_o, is approximately 0.1. Additionally, the best fit value for the limiting current at the crack tip has been shown here to be electrochemically valid, placing the bare surface dissolution rate at 10,000 A/m^2. Therefore, the current decay correlation is relied upon only to determine the current decay curve slope. Examples of current decay curve data reported by Ford and Andresen are shown in Figure 3.10 [3.21].

This plot shows steel data from bare surface dissolution tests conducted in a flowing solution of deaerated 0.01 mNa2SO4 at 288°C with a pH of 6.3. The test was conducted by rapidly changing the potential from –1520 mV SHE to –20 mV SHE. The current decay correlation used in this model is a completely empirical correlation made from experimental measurements such as this one. The measured data was developed into the correlation used in the IEDM by Ford and Andresen [3.11, 3.14, 3.21]. This correlation is used as is rather than creating a new correlation for the model because the battery of experiments necessary to create the correlation is proprietary and difficult to

reproduce. The correlation depends on the conductivity and potential (ECP) of the coolant and on the degree of sensitization of the metal as represented by the EPR value.

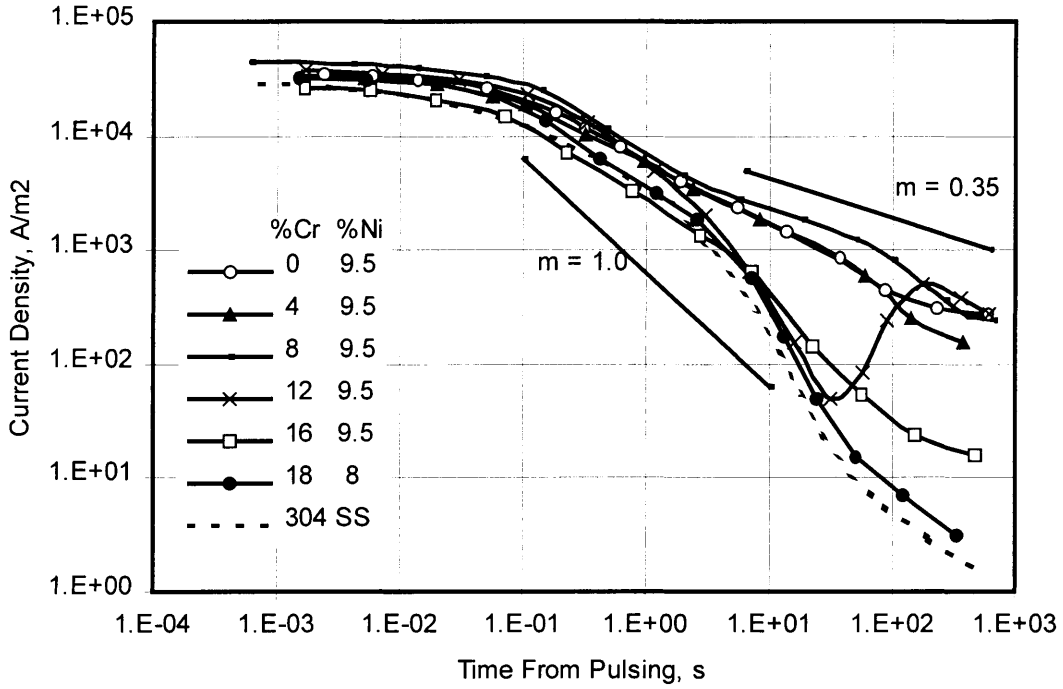

Figure 3.10. Oxidation current density versus time for bared surface Fe-Ni-Cr alloys in 0.01 M Na_2SO_4 at 288°C.

The following equation is the statistical formulation developed to fit the bare surface oxidation data [3.14].

$$m = \left\{ \frac{e^{f(Cond+EPR)}}{e^{f(Cond+EPR)} + e^{f(ECP)}} \right\}^{f(EPR)} \tag{3.34}$$

The functional forms of the dependencies of these equations are proprietary. Therefore, a lookup table was made from plots of the data [3.11]. These plots are shown in Figure 3.11 [3.11].

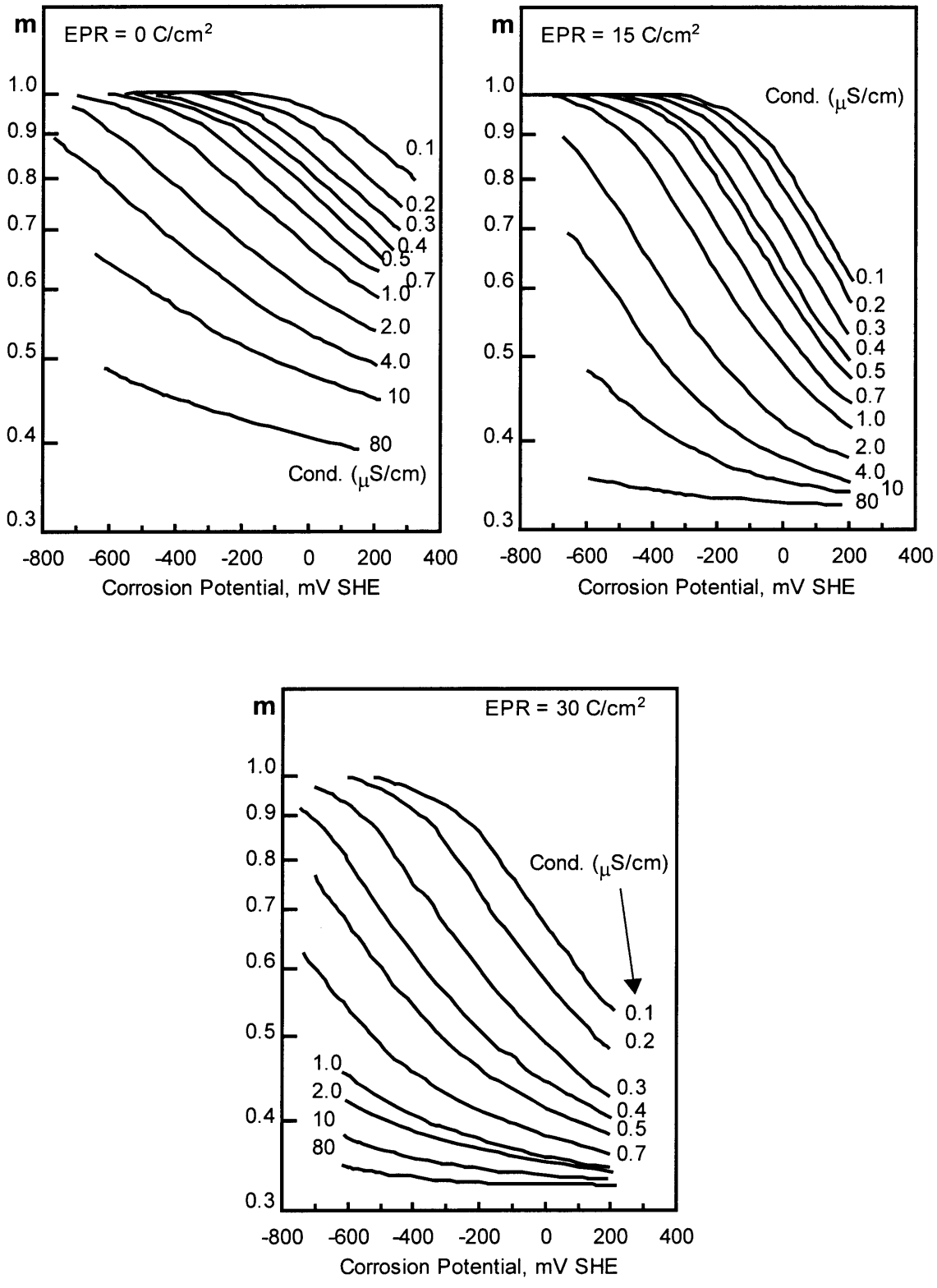

Figure 3.11. Current decay curve slope, m, in terms of ECP and conductivity (at 25C) for stainless steel at three different EPR values [3.11].

The electrochemical potential is an output of the bulk chemistry model and the EPR value comes from the radiation induced segregation model. The conductivity is determined from the output concentrations from the bulk chemistry model and reactor parameters input by the user.

3.2.3. Conductivity

One of the three inputs necessary to the current decay correlation is the conductivity. The conductivity is an essential factor in determining the rate at which cracking occurs because the current density of the dissolution process is limited by the conductivity of the electrolyte. In order for corrosion to occur, two half-cell processes must be occurring simultaneously. The electrochemical potential of the system is the combination of the potential difference between the water and the metal and the potential drop across the water between the side of the anodic and cathodic half-cell reactions. When the conductivity is high, the potential difference at the surface of the metal is maximized because the potential drop in the water is minimized. Low conductivity increases the potential drop in the water decreasing the potential at the metal surface.

Some possible impurity species that could be present in a BWR are chlorides, hydroxides, nitrates, phosphates, sulfates, thiosulfate, Pb2+, Cu2+, Fe2+, Ni2+, Zn2+, I-, and I2. These species arise from corrosion products, contaminants in the feedwater, or in the case of iodine, fission products [3.22]. Feedwater contaminants result from intrusions of demineralizer resins, seawater from condenser leaks, and other failures in the coolant system [3.23].

While this model assumes that cracking increases with conductivity, some evidence indicates that, this may not be the case. Specifically power plants that have reported higher aqueous conductivity do not necessarily have higher rates of pipe cracking [3.23]. Additionally, experiments have shown that the specific salt used to produce a conductive electrolyte gave different IGSCC results in controlled electrochemical potential tests [3.23]. Given this evidence, one might conclude that assuming an increase in cracking with increasing conductivity would be invalid. However, two logical and reasonable assumptions are made in order to validate the effect of conductivity. The first is that salts that result in elevated conductivity in a BWR do not vary greatly from one reactor to another. That is, the conductivity in excess of that of pure water will be due to iron ions, chlorides, sulfides, radiolysis products and other ions which result from the corrosion of reactor components and do not vary greatly between reactors. The second assumption is that differences in cracking between reactors with different conductivities are not valid controlled experiments. Since no two reactors are identical and many parameters effect the cracking rates of reactors, it is not significant that reactors with different conductivities have different rates of intergranular stress corrosion cracking.

In order to calculate the conductivity of the water Equation 3.35 is used:

$$\kappa = \frac{F^2}{RT}\sum_i |z_i| C_i D_i \tag{3.35}$$

Where F is Faraday's number, R is the gas constant, T is the temperature in Kelvin, z is the charge of ionic species i, C is the conductivity and D is the diffusion coefficient. Additionally, Equation 3.36 can be used to describe the conductivity:

$$\kappa = F^2 \sum_i |z_i| C_i u_i \tag{3.36}$$

Where u = D/RT.

Table 3.3 gives the diffusion coefficients and mobilities for H^+ and OH^- (found in all water) and HO_2^- and O_2^- (which are radiolysis products).

Table 3.3. Diffusion coefficients and mobilities [3.17, 3.24].

25°C, D, cm^2/s	25°C, u, cm^2mol/Js	300°C, D, cm^2/s	300°C, u, cm^2mol/Js
$D_{H+} = 0.0000931$	$u_{H+} = 3.76E\text{-}8$	$D_{H+} = 0.00176$	$u_{H+} = 3.7E\text{-}7$
$D_{OH-} = 0.0000527$	$u_{OH-} = 2.13E\text{-}8$	$D_{OH-} = 0.00098$	$u_{OH-} = 2.1E\text{-}7$
$D_{H02-} = 0.00002$	$u_{H02-} = 0.00002$	$D_{H02-} = 0.0002$	$u_{H02-} = 0.00002$
$D_{02-} = 0.00002$	$u_{02-} = 0.00002$	$D_{02-} = 0.0002$	$u_{02-} = 0.00002$

The correlation used to determine the parameters of the current decay curve requires the conductivity at 25°C as input. It would seem logical to have the correlation based on the actual conductivity at 300°C rather than that at room temperature. However, in actual reactor operation only the conductivity of samples that are removed from the reactor and cooled to 25°C has been reported. Therefore, the correlation uses the 25°C conductivity value in order to facilitate verification of the result and to increase the utility of the correlation. Completely pure water has a conductivity of 0.055 μS/cm at 25°C. At 300°C the conductivity of pure water is 13 μS/cm. The reason for this huge increase is twofold. The first reason is that both mobilities and diffusion coefficents increase with temperature as indicated in Table 3.3. The second reason is that the minimum conductivity of pure water is determined by the concentration of OH^- and H^+, which increases with increasing temperature. The sum of the pH and pOH of water at 25°C is

14. Therefore, at neutral pH the concentration of both H+ and OH- are 10^{-7} moles per liter. At 300°C, the sum of the pH and pOH of water is 11.3. Therefore, at 300°C and neutral pH the concentration of H+ and OH- are $2.24*10^{-6}$ moles per liter.

Because the chemistry set used with the plant chemistry model is based on radiolysis and only accounts for compounds made up of hydrogen and oxygen, impurity concentrations, which result in higher conductivity, are not determined by the model. One solution to this problem would be enlarging the chemistry set. However, while an increase in the size of the chemistry set would allow monitoring the effect of corrosion products in the coolant, it would still not account for impurities introduced from fission products or in the feedwater. It would also greatly increase the time required to run the model. Because of these issues, the baseline conductivity, which is the conductivity of a neutral (pH =7) coolant sample at 25°C, must be provided to the model. This value is a common parameter measured at reactors. It is requested by the graphical user interface before the current decay correlation is used to ensure that all sources of conductivity are accounted for. Inputting this figure directly is a valuable feature because the effect of conductivity transients can be studied using the IEDM.

Since the conductivity of a solution is the sum of the contribution of each ionic species, the effect of OH^- and H^+ on the baseline conductivity can be subtracted and then the total conductivity based on all oxygen and hydrogen species can be added back. The conductivity of neutral pure water (0.055μs/cm) is subtracted from the baseline conductivity. Then, the conductivity due to ionic radiolysis products, as well as H+ and OH- concentration, which may not be neutral, will be added. This results in the

conductivity that is used by the current decay curve correlation to find the slope of current decay, m.

3.3. Hydrogen Embrittlement

The final parameter in the slip dissolution/film rupture relationship is C, the cleavage contribution due to hydrogen embrittlement. Like other forms of environmentally induced cracking, hydrogen embrittlement cracking requires the combination of a susceptible material, a sufficiently aggressive environment, and a tensile crack tip stress. The crack tip stress is the same as that resulting in dissolution based stress corrosion cracking. The material and environment conditions, however, are quite different.

Hydrogen embrittlement is an important factor in cracking for body-centered cubic (BCC) iron alloys due to the restricted slip capabilities found in these alloys [3.16]. The austenitic alloys (which include the stainless steel alloys studied here) have face centered cubic (FCC) crystal structures. This structure has an increased resistance to hydrogen embrittlement due to its high ductility and lower hydrogen diffusivity. However, both resistance to embrittlement and low diffusivity diminish when the metal is highly cold worked [3.16]. The dislocation density produced by radiation hardening leads to the same conditions as cold work; an increased hydrogen diffusivity and decreased ductility. Therefore, in terms of material, it is somewhat likely that hydrogen embrittlement will be relevant for the conditions relevant to the IEDM.

The hydrogen embrittlement effects are included in the IEDM because of their applicability to materials other than austenitic stainless steels. Hydrogen embrittlement

effects are more severe in high strength materials [3.16]. While hydrogen embrittlement does not significantly affect common stainless steels, problems are more frequently experienced with the use of high strength superalloys. Precipitation-strengthened Ni-Fe-Cr alloys are widely used as light water reactor core internal structural materials [3.25]. Therefore, the hydrogen embrittlement contribution is important in allowing the model to be adapted for evaluation of superalloys and other high strength metals.

In addition to a susceptible material and significant tensile stress, the environment in which hydrogen embrittlement is likely to occur must also be considered. In order for hydrogen embrittlement to occur, the electrochemical potential of the system must be low enough that the reduction of hydrogen is a dominant cathodic reaction. Since the measurement scheme for potential is based on the reversible potential for hydrogen, the ECP of the system must be less than 0 mV vs. SHE. At 0 mV SHE no net reduction of hydrogen occurs, rather the reduction and oxidation of hydrogen are balanced and each reaction occurs at the exchange current density. Therefore, the potential must be further reduced before the reduction of hydrogen in a crack becomes significant.

As a result, the factor C depends on the metal and the environment. For a given metal, C increases with hardness, which signifies a decrease in ductility and an increase in the diffusivity of hydrogen through the material. Additionally, the diffusivity varies with alloy content of the metal. Looking at environmental factors, C increases with hydrogen reduction in the crack. Hydrogen reduction occurs when the potential is between the reversible potential of hydrogen (0 mV SHE) and the reversible potential of the metal (-450 mV SHE for stainless steel). Hydrogen reduction increases with the amount of H^+ ion in the system, which is signified by lower pH. The change in pH is not

significant in boiling water reactors, as the coolant is nearly neutral. Another environmental effect is temperature. Hydrogen embrittlement increases in severity at temperatures where the diffusivity of hydrogen is high enough to carry the hydrogen to the crack tip but not so high that it will diffuse out of the crack tip region.

A logical step in the development of any model is to select a mechanism. However, a multitude of proposed mechanisms have been suggested. While many of these have not stood up to critical examination, several mechanisms have been deemed viable [3.26]. It is possible that several of the remaining failure mechanisms are valid and that different mechanisms operate for varying conditions. The following three requirements must be met to provide hydrogen to the crack tip [3.14]:

(1) A species which contains reducible hydrogen must be present at the crack tip due to diffusion along the crack tip or high concentration in solution.

(2) The hydrogen must be reduced at the crack tip and this reaction must be balanced by an oxidation reaction. The oxidation process need not occur at or near the crack tip.

(3) The hydrogen on the surface of the metal must diffuse to the crack tip region within the metal.

Five mechanisms will be outlined in the following paragraphs to indicate the wide range of mechanisms developed to describe hydrogen embrittlement. One mechanism for hydrogen embrittlement purports that the reaction of hydrogen atoms with dislocations, voids, or the stress field at the crack tip to decrease the ductility of the metal [3.21]. In this mechanism, hydrogen diffusing through the metal matrix congregates at positions where the

interstitial spacing is greater. This includes areas such as just behind the crack tip where there is significant triaxial tensile stress, as well as dislocations and voids. The accumulation of hydrogen atoms restricts the flow of dislocations resulting in embrittlement of the metal.

Another mechanism purports that the build-up of gas pressure at vacancies and dislocations in the plastic zone at the crack tip results in fracture [3.21]. Accumulating gases include diatomic hydrogen, methane, and hydrogen sulfide. This mechanism might explain the effect which carbon and sulfur have on intergranular cracking. This mechanism contrasts the previous mechanism in that the gases result in increased stresses in the material rather than limiting plastic deformation.

Another mechanism is the atomic decohesion theory [3.27]. Electrons donated from dissolved hydrogen atoms enter the incompletely filled d-bond of transition metals. The increased electron density acts to increase the interatomic spacing of the lattice, which reduces the cohesive strength of the metal. At any location within the metal lattice where hydrogen concentrates, the cohesive strength is reduced, and the metal becomes more susceptible to SCC.

In a mechanism developed by Jani, et al., the stacking fault energy of the crystal is lowered in the hydrogen affected region [3.28]. This restricts cross-slip, allowing only planar slip to occur. Lomer-Cotrell supersessile dislocations then form, reducing slip further and causing high stresses to result. Like the first model, where hydrogen acts interstitially, or the decohesion model, the Jani model predicts decreased plasticity. This contrasts the final model that I will mention which predicts that plasticity is enhanced.

This model supposes that hydrogen reduces the shear stress required for dislocation motion at the crack tip [3.41]. Because of the reduction in sheer stress, the local plastic-flow process associated with crack propagation is eased. This model works in combination with another mechanism such as the slip dissolution-film rupture model. Dislocation motion to the crack tip is aided allowing the stresses required to break the passive film at the crack tip to acquire more quickly.

Given that it is not even clear whether plasticity is enhanced or reduced by hydrogen embrittlement, it is obvious why deterministically accounting for hydrogen embrittlement is difficult. The solution to this problem is to account for hydrogen embrittlement empirically knowing that it increases with hardness, crack tip hydrogen availability and optimal temperature.

3.4. Correlation between RIS and EPR

Sensitization is the process by which the metal matrix near the grain boundary is depleted in one or more beneficial elements or enriched in one or more detrimental elements resulting in an increased susceptibility to intergranular stress corrosion cracking [3.29]. In austenitic alloys, the main element that is depleted at the grain boundary is chromium. Due to chromium's role in passive film formation, its depletion at grain boundaries results in increased vulnerability to cracking. The radiation induced segregation discussed previously can cause sensitization during reactor operation. An additional source of sensitization that develops during construction of the reactor and preparation of the materials is thermal sensitization.

Thermal sensitization results from heat treatment or the cooling process following welding. Thermal sensitization is caused by the precipitation of chromium rich carbides $(Fe,Cr)_{23}C_6$ along the grain boundary [3.16]. Because precipitation occurs at grain boundaries and the carbides are very high in chromium, the metal matrix near the grain boundaries is depleted of chromium. Precipitation of chromium carbides occurs between 425°C and 815°C. Below 425°C, the diffusion rate of chromium is not sufficient for carbide formation; above 815°C, the chromium remains in solution. One might ask, if thermal sensitization is an important cause of irradiation assisted SCC in nuclear Reactor environments, why is there no model here for thermal sensitization? A model or correlation for thermal sensitization is feasible. However, it is more likely that an operating reactor would have estimates of the sensitization of various components than the exact thermal history before and during construction. Therefore, thermal sensitization is taken as an input while radiation induced segregation can be determined over the lifetime of the plant.

It is important to note that in addition to chromium, excess carbon is required to form the species whose precipitation results in thermal sensitization. Therefore, one method to reduce sensitization is to reduce the carbon content of the steel. In 304L and 316L steels, the 'L' stands for low carbon; these alloys were developed to prevent sensitization.

In addition to measuring the degree of sensitization (DOS) by microscopic analysis of the minimum chromium concentration along the grain boundaries, a standard method has been designed for nondestructive testing and has become widely used to describe the degree of sensitization. This method is the electrochemical potentiokinetic

reactivation (EPR) technique. EPR tests allow rapid in-situ testing of DOS [3.30]. The standard single-loop EPR technique was developed by Striecher et al. and is advantageous relative to previous methods of testing IGSCC susceptability because it is sensitive, quantitative and nondestructive [Striecher]. To conduct a single-loop EPR test, first the sample is polished to a 1-μm diamond finish. The test is conducted by forming a passive film on the specimen surface by exposing the sample to a sufficiently high potential, usually 200 mV vs. SCE [3.31]. Following, a two minute hold the reactivation scan begins and the potential is reduced at a rate of 6V per hour. The current passed as the metal oxidizes in the active region is measured to quantify the film breakdown and grain boundary attack [3.32]. The standard electrolyte for this test is 0.5 M H_2SO_4 + 0.01 M KSCN at 30°C [3.33]. The reactivation charge, Q, measured in coulombs must be normalized for the specimen area and grain size. Therefore, the standard single-loop EPR value, P_a, is given by dividing Q by the grain boundary area. P_a has units of Coulombs per square centimeter.

A modification to the standard EPR test is the double-loop EPR test [3.34, 3.35]. In this test, an anodic scan rather than a passivation hold precedes the reactivation scan. During the anodic scan, the electrochemical potential of the system is increasing. The anodic scan has a higher maximum current than the reactivation scan and the results of double-loop test are reported as the ratio of the maximum currents during the reactivation scan and the anodic scan [3.35]. The advantages of the double-loop test are that the result is a ratio and therefore need not be normalized and that the metal does not need to be polished as finely.

The effect of radiation induced sensitization following thermal sensitization is not well understood because little research in this area has been conducted. The depletion profile for radiation induced segregation is narrower (usually 5-10 nm [3.36]) than that due to thermal segregation (50-100 nm). Therefore, RIS is unlikely to greatly effect sensitized materials. In the model, either an input value is provided for the EPR due to thermal sensitization or the RIS model is used to determine an equivalent EPR due to radiation induced segregation. The most accurate method, given the differences between the two processes and the resulting depletion profiles, is to use whichever EPR value is greater.

The fact that radiation induced segregation tends to result in a narrower chromium depleted region than that due to thermal sensitization is an important consideration. The reactivation current in the standard EPR test depends mainly on the width of chromium depletion where the grain boundary intersect the specimen surface [3.35, 3.37]. EPR has been used and has even come to define degree of sensitization in thermally sensitized steels [3.35]. That EPR and degree of sensitization have come to be interchangable can be seen as a problem because the outcome of an EPR test depends on what test is conducted. That is, EPR and therefore DOS is defined in terms of the EPR test conducted whether it is a single-loop, double-loop or modified EPR test. Therefore, sensitization is a relative term and the relationship between susceptibility to IGSCC and EPR must be determined for each type of EPR test and each type of metal being studied. By changing the electrolyte in which the EPR test takes place the test can be made to be more sensitive to the depth of the chromium depletion rather than the width [3.37]. These differences are significant when comparing EPR data to IGSCC susceptibility. In the

IEDM, the EPR is not correlated directly with IGSCC. Instead the equivalent EPR value for a standard single-loop test is determined from chromium depletion profile following radiation induced segregation or a value is provided to the model. Then the EPR value is used only to determine the electrochemical behavior of the metal following rupture of the passive film protecting the metal at the crack tip. This is reasonable because like the EPR test, the current decay following a repassivation event also depends on the electrochemical response to changing potential.

Having determined that EPR will be useful in the model, we must now look at how to determine the EPR. There are correlations between EPR test results and IGSCC susceptibility in the literature. However, they have been designed for thermally sensitized materials and may not be adequate for RIS. The following paragraphs describe the development of an EPR correlation for thermally sensitized materials with known chromium profiles.

The output of the RIS model which is most relevent to IGSCC susceptibility is the chromium profile. However, the input to the current decay correlation which gives the metal chemistry is the EPR value. The EPR value is the result of an electrochemical test of grain boundary dissolution kinetics. In order to utilize data from the RIS model in the current decay curve correlation, an intermediate correlation is needed. This correlation must estimate the EPR value from the chromium profile. Breummer has developed a correlation to estimate the EPR value of a metal specimen based on the shape and size of the chromium profile. The correlation uses the volume depletion parameter originally formulated by Was [3.38]. The volume depletion parameter is a measure of the cross

sectional area of metal that has a chromium concentration below a certain value. Equation 3.37 is the equation for the volume depletion parameter:

$$VDP = \frac{(Cr_{crit} - Cr_{min})W_{crit}}{2Cr_{crit}} \tag{3.37}$$

Where Cr_{crit} is the critical chromium concentration, Cr_{min} is the minimum chromium concentration and W_{crit} is the width of the profile at the critical concentration. The source of these variables is shown in Figure 3.12. The equation is divided by two because the area represents a triangle. This term is irrelevent but is maintained because of its use by Was and later Bruemmer. The equation is divided by the critical chromium concentration simply to normalize the units. For a given correlation between VDP and EPR, Cr_{crit} will be constant. By dividing by Cr_{crit} the units of concentration are removed allowing the use of percentages or fractions by weight or atom.

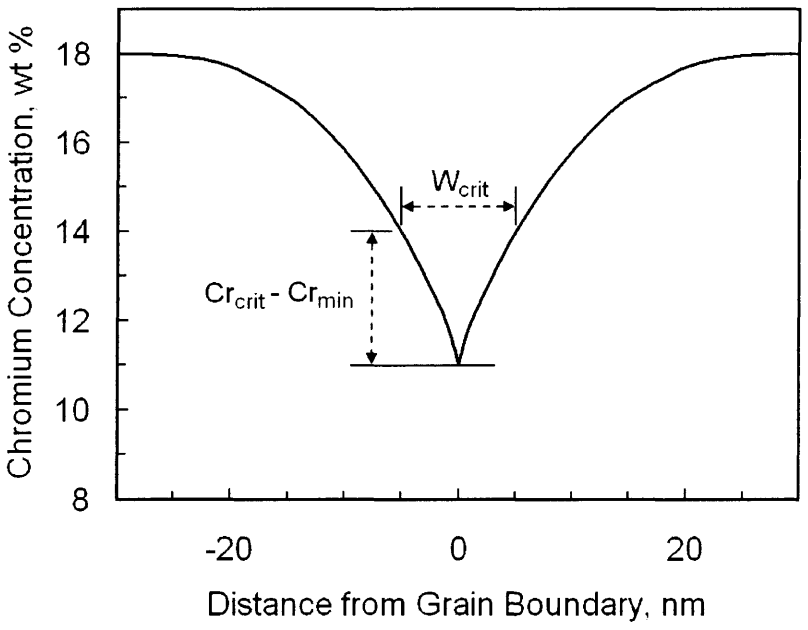

Figure 3.12. Example of volume depletion parameter from the chromium profile.

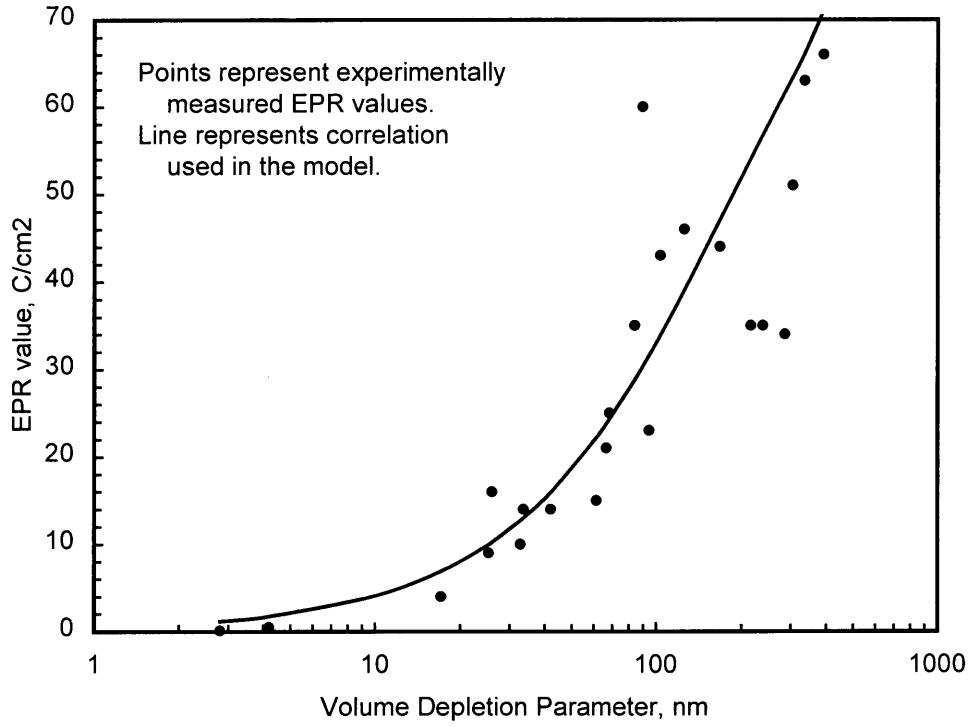

Figure 3.13. Correlation between volume depletion parameter and the electrochemical potentiokinetic reactivation (EPR) for a critical chromium value of 14%.

Figure 3.13 is a plot of most of the data used to calibrate a correlation between the volume depletion parameter and the measured EPR. Notice that the scatter of the data is not severe. This plot is much tighter than either a plot of minumum chromium concentration versus EPR, or a plot of the profile width at the the critical concentration (W_{crit}) versus EPR. The following is the equation for the solid line on the plot.

$$EPR = 0.42(VDP) - 0.001(VDP)^2 + 1 \cdot 10^{-6}(VDP)^3 \qquad (3.38)$$

While this equation is valid for thermal segregation, the model does not evaluate chromium profiles for thermal segregation. Rather, it determines and evaluates chromium profiles for radiation induced segregation. Therefore, the volume depletion

parameter must be correlated with experiments from the literature on the effect of RIS on crack growth rate.

The most complete battery of experiments to determine the effect of RIS on crack growth rate is that of Jenssen and Ljungberg [3.39]. This battery of experiments has been used to determine a reasonable fit between the volume depletion parameter and the equivalent EPR for RIS. This battery of compact extension rate tests studies SS 304 and 316 over a wide range fluences. Compact extension rate tests were conducted to determine crack growth rates. The test conditions were similar to BWR conditions and those conditions used to verify the crack growth model. The samples were tested in reactor feedwater with a conductivity of 0.2μS/cm and potential between 100 and 200 mV SHE. Therefore, it is reasonable to use this data to "back out" a relationship for RIS.

A major problem with this data was that it was taken from linear plots. The crack growth rates were shown on a scale from 0 to 2 x 10^{-6} mm/s. Therefore, growth rates below 10^{-8} mm/s are shown as 0 mm/s. Another problem was a lack of clarity in terms of the irradiation scheme. The samples were irradiated in a reactor for 1, 2 and 5 reactor cycles, at fluxes ranging from 1 to 4 DPA per year [3.39]. While the fluence is given explicitly for each data point, irradiation times of 1, 2 or 5 cycles is excrutiatingly vague. This is especially significant because the susceptibilty varies with time for the same fluence as indicated by the figure at the end of the section describing the RIS model. It was assumed that a cycle was 6 months; because this made the choice of 1, 2 and 5 cycles reasonable given the relationship between the fluxes and fluences.

A best fit to the data with two sets of output from the crack growth model (ECP = 100 mV SHE & 200 mV SHE) yielded the following relationship between the volume depletion parameter.

$$EPR = 135 \cdot VDP - 7.0 \tag{3.39}$$

This relationship was found to minimize the error in the highly scattered Jenssen data for stainless steel 304. Figure 3.14 is a plot showing the data and the model predictions. This plot is shown with a linear y axis for similarity to the data in Jenssen.

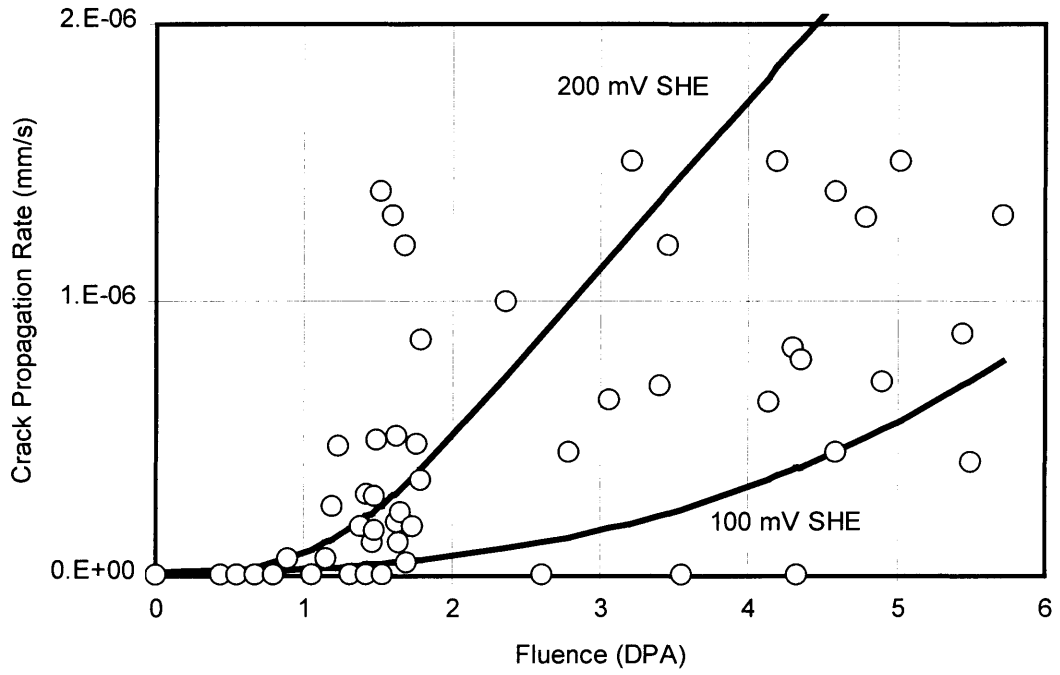

Figure 3.14. Fluence versus DPA for stainless steel 304 in oxidizing conditions, Circles: experimental data; lines: model output.

This plot indicates the source of some of the scatter exhibited in the Jenssen data. The variation in potential leads to large variation in the output data. The following plot shows the same data with the crack growth rate plotted logarithmicly. On this plot the zero values are plotted at 10^{-8} mm/s.

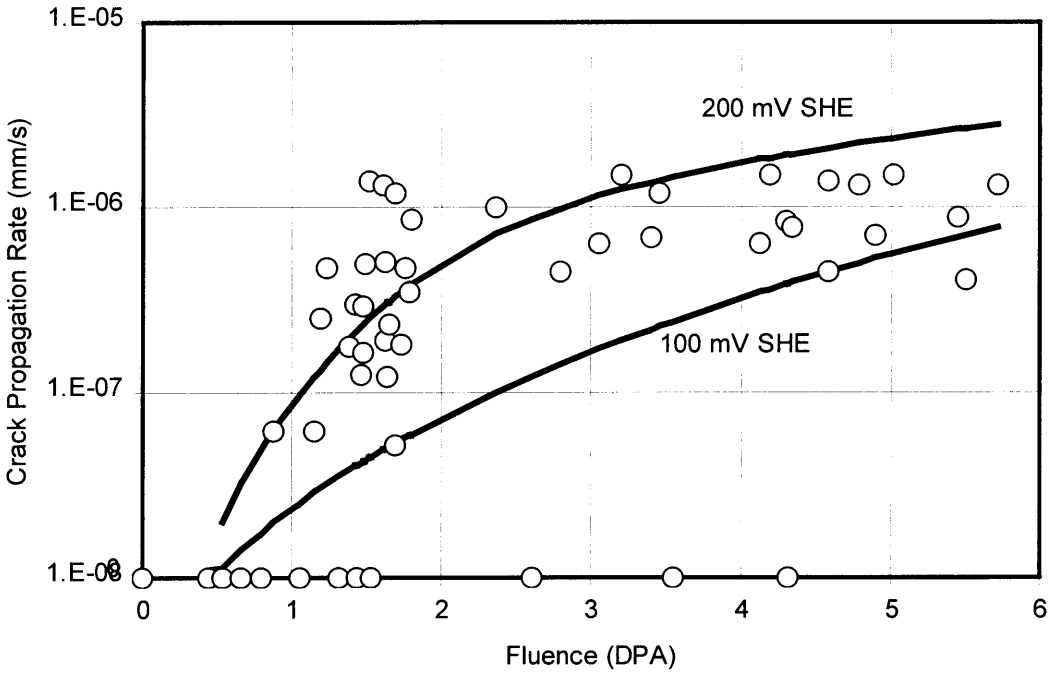

Figure 3.15. Fluence versus DPA for stainless steel 304 in oxidizing conditions. Circles: experimental data; lines: model output.

For 316 stainless steel the following equation correlates the volume depletion parameter with an equivalent EPR for radiation induced segregation.

$$EPR = 57 \cdot VDP - 5.2 \tag{3.40}$$

This value shows agreement similar to that found for stainless steel 304. However, less data was available in the paper to define this relationship.

IGSCC of sensitized Alloy 600 has been demonstrated to be most severe in samples with narrow but deep chromium-depleted zones [3.34] The mechanism of IGSCC in Alloy 600 in nuclear reactor environments is not well understood. When more data is available a correlation for Alloy 600 can be added to model. Until such a time that data is available to determine an equivalent EPR for the volume depletion parameter of

Alloy 600, an EPR value will have to assumed in order to model the cracking susceptibility.

3.5. Sensitivity Analysis

This section describes the sensitivity of the various parameters used by the crack growth model. It has been developed from a parametric study. It is important to understand which values have the greatest effect on the crack growth model. This way special attention can be paid to parameters that have a large effect on the crack growth rate and are difficult to determine with great accuracy. For each variable a rate of change factor is determined and listed in Table 3.5 at the end of this section. Additionally, the precision by which this value is likely to be known is also given in the table. The following table indicates the base case for cracking used for the sensitivity analysis.

Table 3.4. Base case values for sensitivity analysis.

Variable	Base Case Value
λ, Plastic zone size constant	$1/(3\pi)$, 0.106
β, Analytical strain distribution constant	5.5
M, Metal atomic mass	56 g/mole
ρ, Metal density	8000 kg/m^3
z, Oxidation state of dissolution	2
ε_f, Passive film rupture strain	0.007
E, Young's modulus	22000 kg/mm^2
σ_y, Yield strength	20 kg/mm^2
n, Strain hardening exponent	0.33
K, Stress intensity factor	80 $Kgmm^{1/2}/mm^2$
K', Stress intensity factor rate of change	0.0001 $Kg/mm^{3/2}s$
r, Distance from growing crack tip	0.04 mm
C, Hydrogen embrittlement cleavage factor	0 mm
m, Oxidation current decay curve slope	0.7
t_o, Time constant for current decay	0.1 s
i_o, Oxidation current density of bare surface	10000 A/m^2

First the sensitivity of constants that are fixed in the model (λ, β) were evaluated. Then parameters which are determined directly from the metal (M, z, ρ, ε_f, E) were studied. Additionally, the sensitivity of the two materials parameters which may be determined by the irradiation hardening model (σ_y, n) were evaluated. Next the stress intensity factor (K), its rate of change (K'), and the distance from the crack tip at which the strain is acting (r) were varied. The effect of the hydrogen embrittlement term (C) was evaluated next. The sensitivities of the electrochemical parameters (m, to, io) were determined. Additionally, the sensitivity of the values used in the current decay curve slope correlation (Conductivity, ECP, EPR) were assessed.

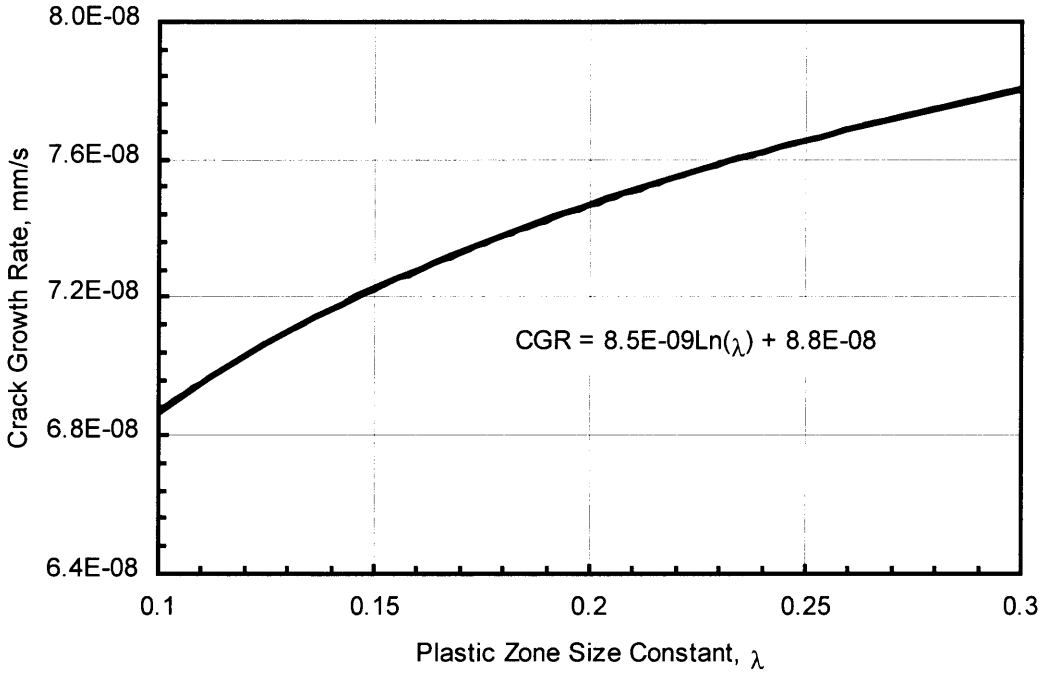

Figure 3.16. Crack growth rate versus plastic zone size constant for the base case parameters.

Lambda is the proportionality constant for the plastic zone size. For plane strain, it is given as $1/(3\pi)$ by Gerberich [3.1]. Lambda could vary based on different representations of the plastic zone size for different cracking modes. As Figure 3.16 indicates, the crack growth rate increases with rising plastic zone size constant with a dimensionless slope of 0.12 (% rise/% run) at 0.106. The crack growth rate does not change significantly over the range of lambda.

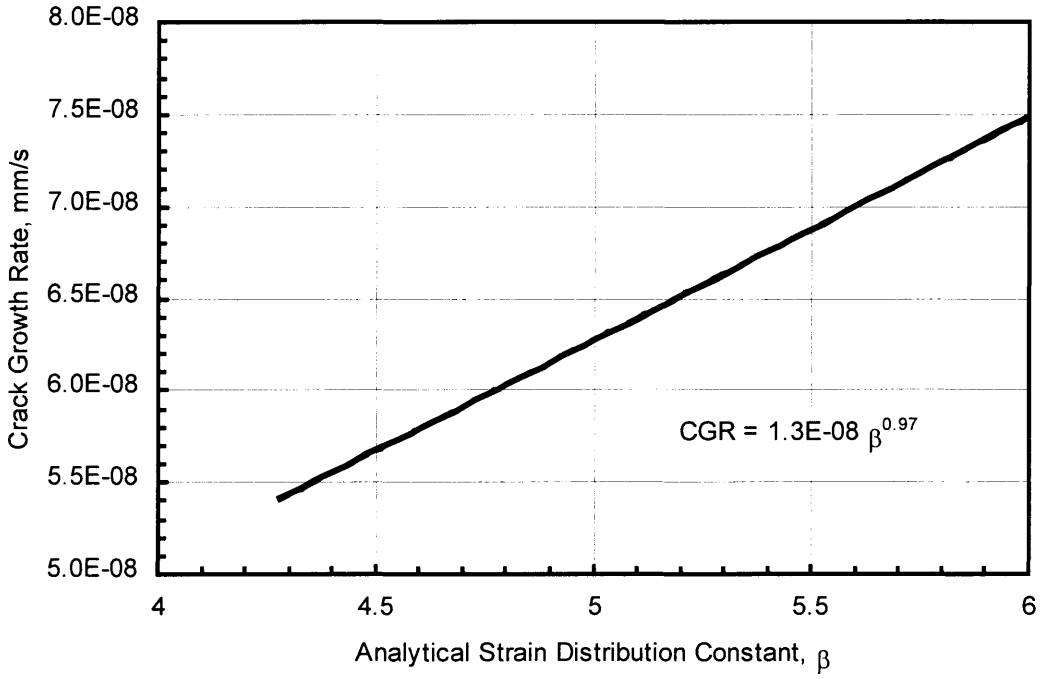

Figure 3.17. Crack growth rate versus analytical strain distribution constant for the base case parameters.

Beta is the proportionality constant of the analytical strain distribution for a growing plane strain crack. Values for beta have ranged from 4.28 to 5.81 with 5.5 being used here [3.2]. As Figure 3.17 shows, the crack growth rate increases with rising analytical strain distribution constant with a dimensionless slope of approximately 1. The crack growth rate does not change significantly over the likely range of Beta.

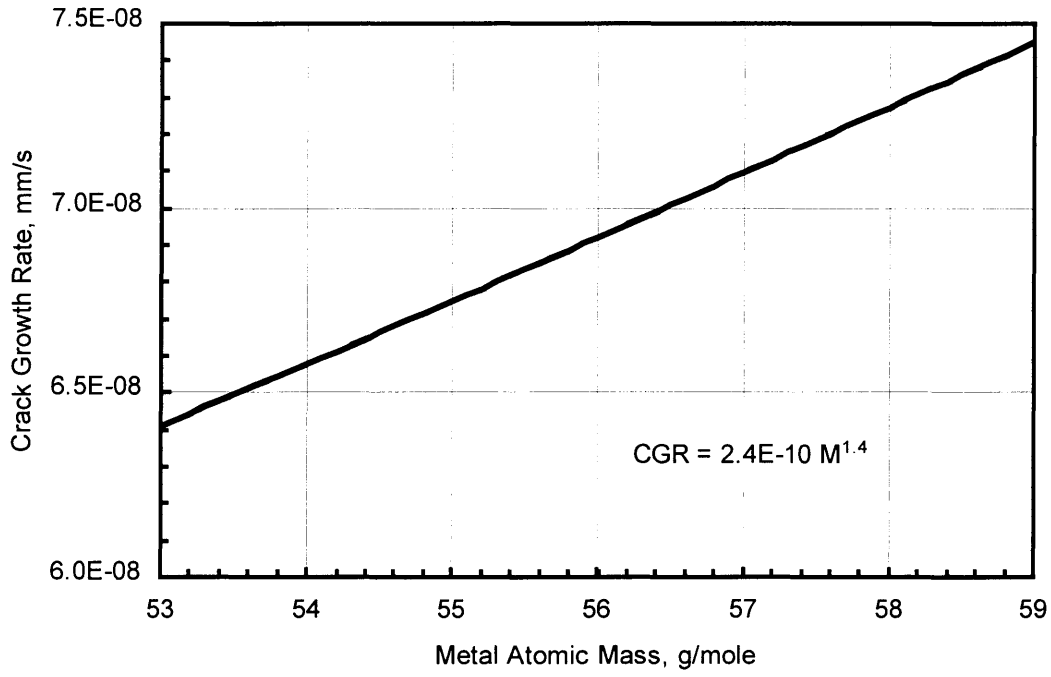

Figure 3.18. Crack growth rate versus metal atomic mass for the base case parameters.

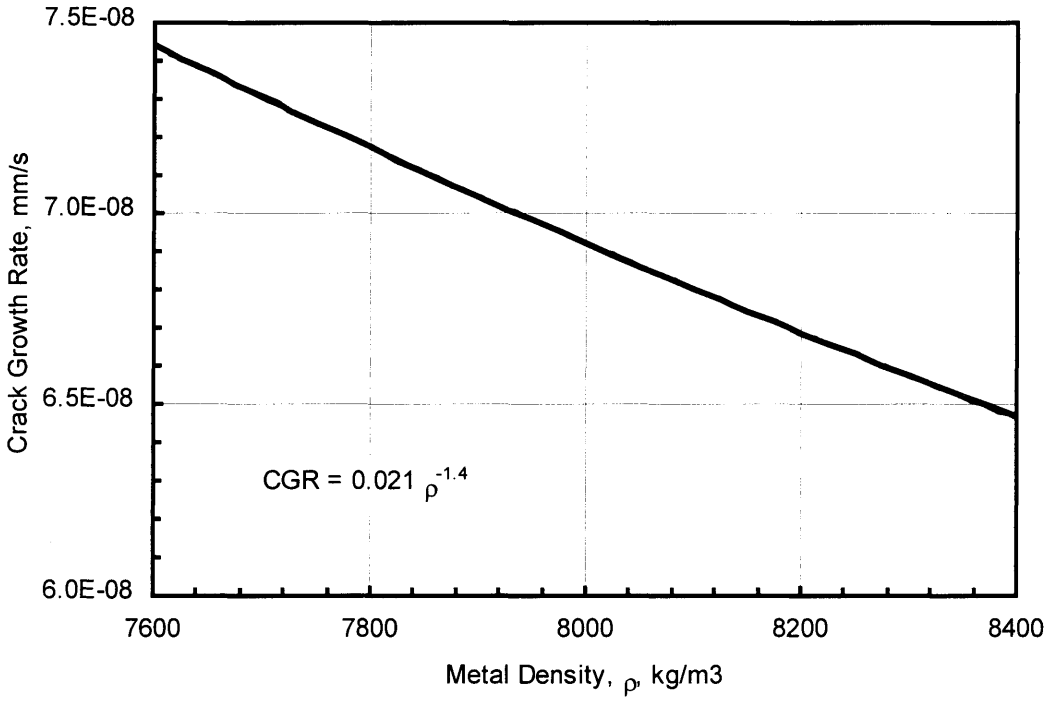

Figure 3.19. Crack growth rate versus metal density for the base case parameters.

The metal atomic mass and metal density are obviously constant for a given metal. These are used to calibrate Faraday's relationship in the model. Therefore, they are simple multiplicative factors in the model. However, their effects on the crack growth rate are still interesting. They have the opposite effect of one another. As Figure 3.18 shows, the crack growth rate increases with rising atomic mass (slope = 1.4 at 56 g/mole). In Figure 3.19, the crack growth rate is decreasing with increasing metal density (slope = -1.4 at 8000 kg/m^3).

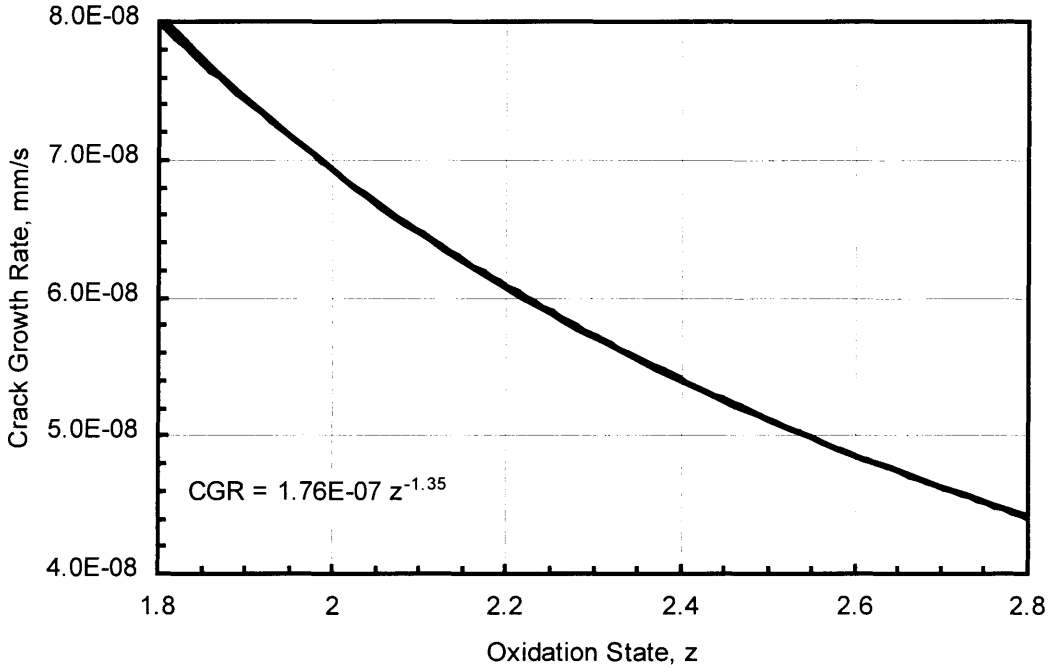

Figure 3.20. Crack growth rate versus oxidation state for the base case parameters.

The oxiadation state of dissolution is considered a property of the metal but it is actually more complicated than that. It depends on the alloy content of the metal (locally), on which alloy components dissolve during the corrosion event, and on what the oxidation states of the oxidized metals are. The value used here is 2 because most of the corrosion at the crack tip is iron and nickel which both have an oxidation state of 2.

However, some chromium may also corrode with an oxidation state of 3. Therefore, this value may be higher than 2. Figure 3.20 indicates that the crack growth rate decreases with increasing oxidation state with a slope of -1.4 at z = 2. The crack growth rate does not change greatly over the likely range of oxidation states relative to other sources of error.

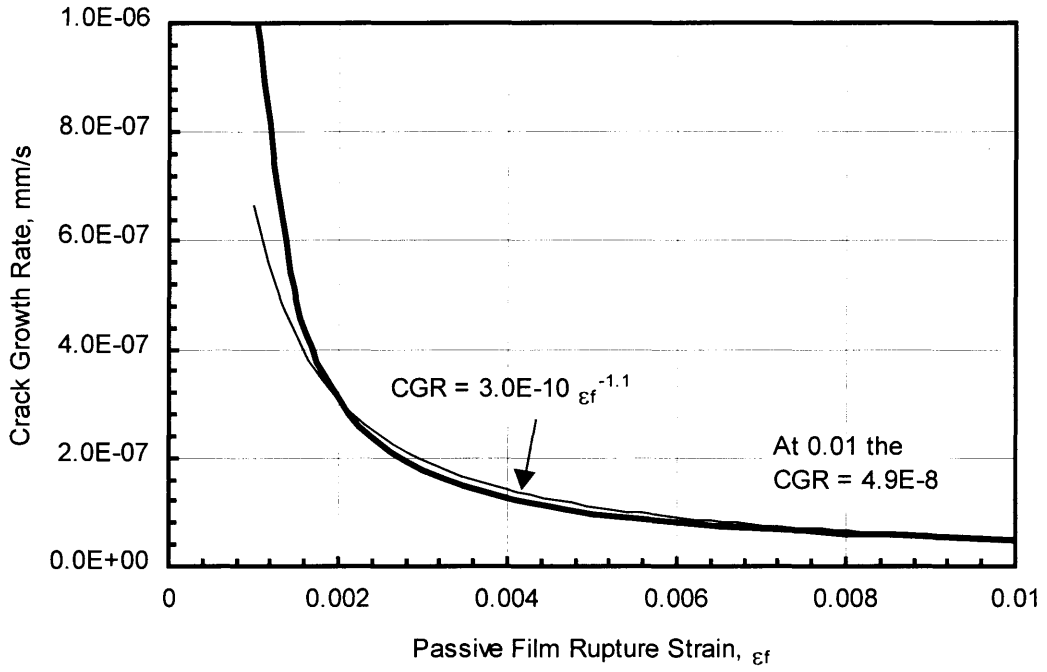

Figure 3.21. Crack growth rate versus passive film rupture strain for the base case parameters.

The passive film rupture strain has been reported with values ranging from 0.001 to 0.015 [3.15]. In the crack growth model used here, a value of 0.007 is used for the chromium rich passive film that protects austenitic Fe-Ni-Cr alloys based on experimental measurement [3.15]. Figure 3.21 shows the effect of the passive film rupture strain on the crack growth rate for the base case. At 0.007 the crack growth rate is decreasing with a dimensionless slope of -0.9. As the passive film rupture strain

increases by one order of magnitude, the crack growth rate decreases by an order of magnitude. This is significant because the passive film rupture strain is uncertain within the range from 0.001 to 0.01.

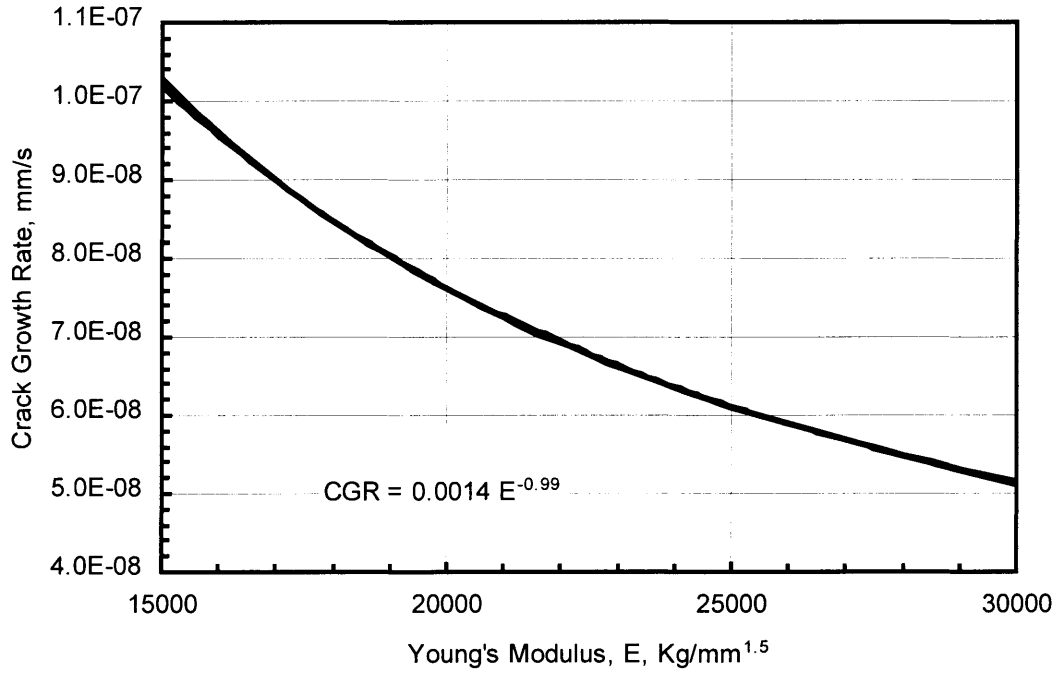

Figure 3.22. Crack growth rate versus Young's modulus for the base case parameters.

The Young's modulus is a property of the metal that does not change appreciably with irradiation or temperature in the temperature range of model validity. Figure 3.22 shows that the crack growth rate decreases with increasing Young's modulus with a dimensionless slope of -1. Because the Young's modulus is known with better than10% accuracy, it does not contribute significantly to error in the result.

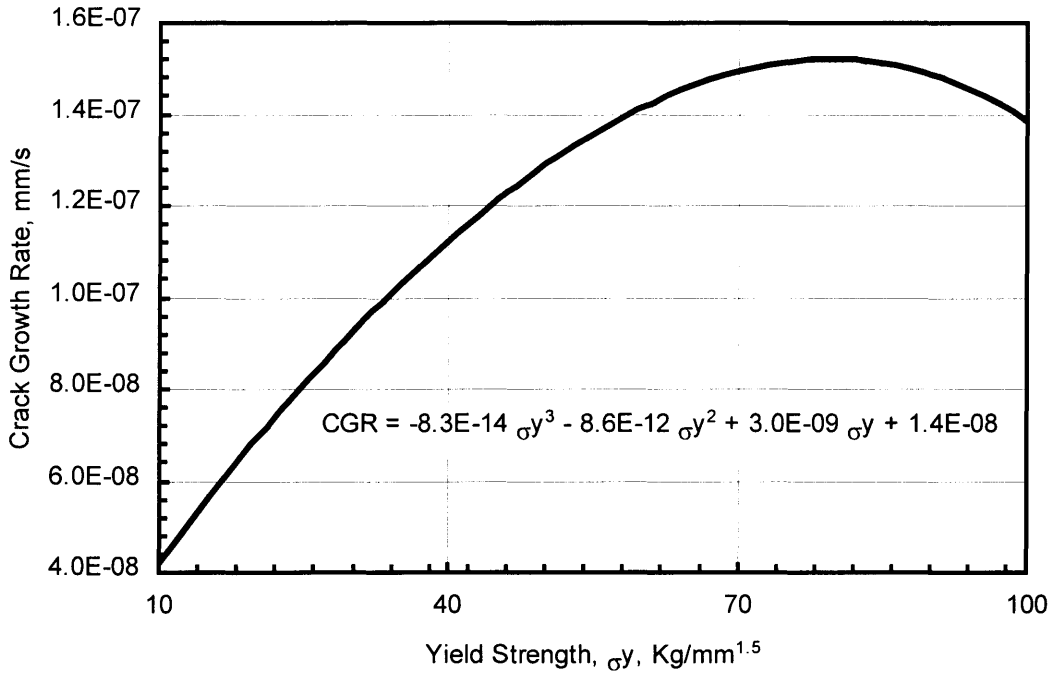

Figure 3.23. Crack growth rate versus yield strength for the base case parameters.

The yield strength of the metal is an important parameter in the determination of the crack trip strain distribution. Figure 3.23 indicates its effect of the crack growth rate. Its uncertainty is high due to radiation hardening. It is found in both the numerator and the denominator, and therefore the crack growth rate increases for low strength value and decreases with increasing strength for high strength values. The peak value occurs when the yield strength is equal to the stress intensity factor. Despite the high uncertainty of the yield strength, the variance in crack growth rate is low. For the input values studied here the crack growth rate only changes by a factor of two over the entire range of yield strength.

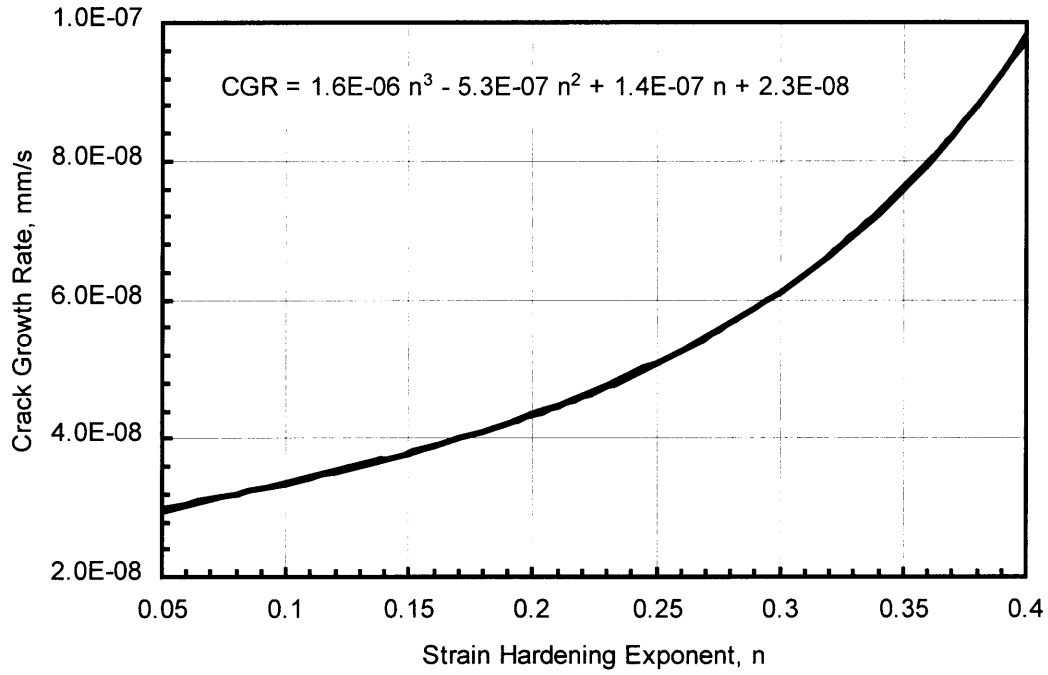

Figure 3.24. Crack growth rate versus strain hardening exponent for the base case parameters.

The strain hardening exponent, n, defines the extent to which a material work hardens as it is being strained. As the yield strength increases due to cold work or irradiation hardening, the strain hardening exponent decreases. As shown in Figure 3.24, as the strain hardening exponent increases, its effect on the crack growth rate increases as well. The strain hardening exponent is a significant source of error because its uncertainty can be as high as +/-0.1. Over the range from 0.2 to 0.4 the crack growth rate changes by nearly a factor of 3.

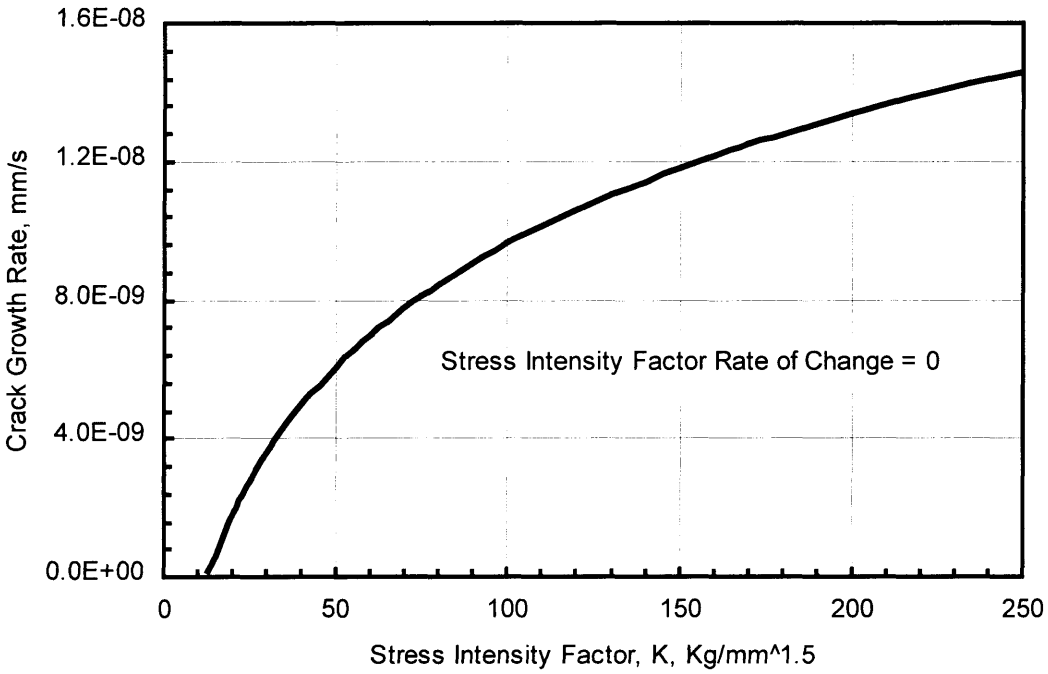

Figure 3.25. Crack growth rate versus stress intensity factor for the case where the stress insety factor is equal to 0.

The stress intensity factor, K, is determined from the far field stress at the crack tip and the crack length. Rather that being calculated, it is usually simply inputted to the model. Therefore, it has high uncertainty. Figure 3.26 indicates the effect of stress intensity factor for cracking when the stress intensity factor rate of change is 0. Here the stress intensity factor only varies by a factor of 2 over the likely range of values. Therefore, despite the high uncertainty of this value, it does not contribute greatly to error in the crack growth rate for high stress intensity factors and high crack growth rates.

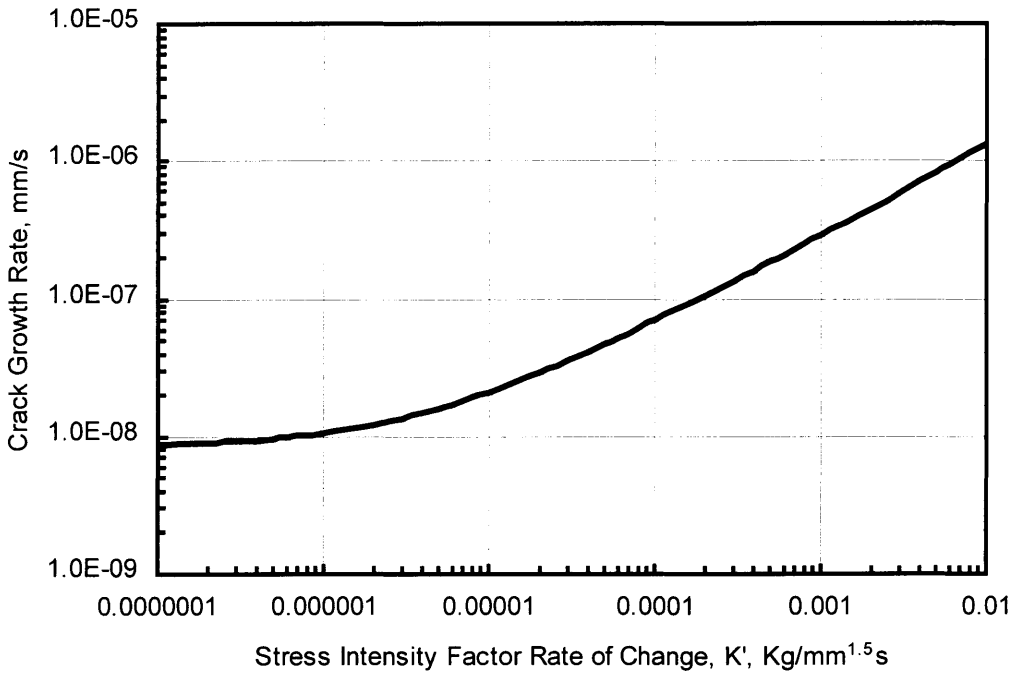

Figure 3.26. Crack growth rate versus stress intensity factor rate of change for the base case parameters.

The stress intensity factor rate of change, K', indicates an increasing stress intensity factor due to increasing crack length and/or tensile stress. The dimensionless slope is between 0.5 and 0.6 for values above 0.0001. Figure 3.26 shows that the slope increases with increasing strain rates. The sensitivity to the crack growth rate is not high. However, K' has high uncertainty; it is likely to be known only within 1 order of magnitude. Therefore, K' contributes significantly but not greatly to the error in the crack growth rate.

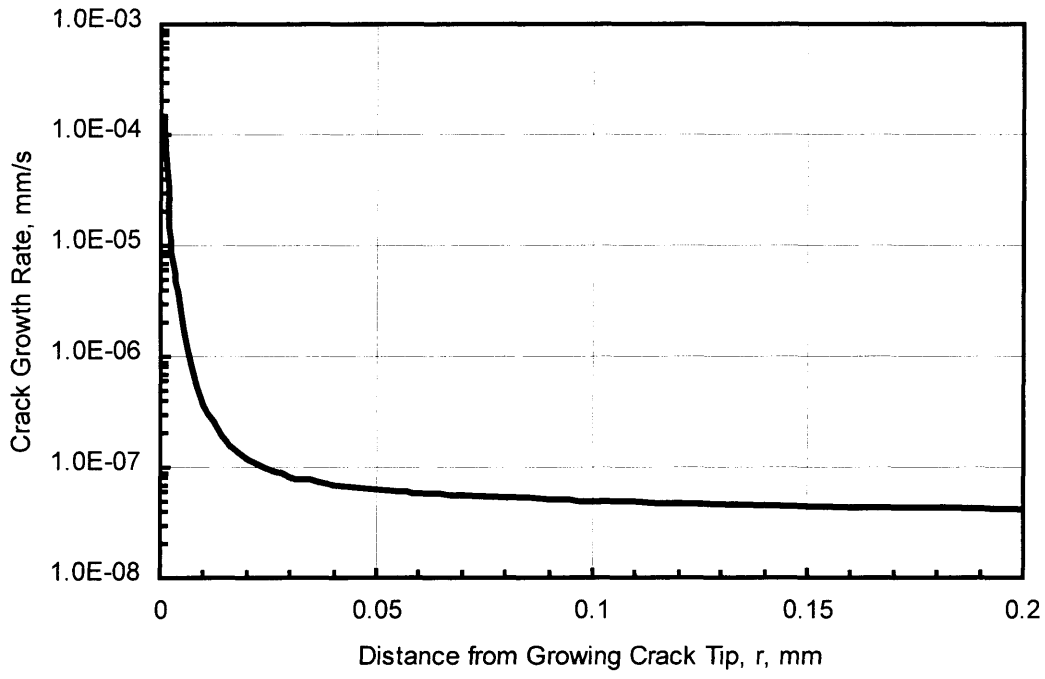

Figure 3.27. Crack growth rate versus distance from the growing crack tip for the base case parameters.

The distance from the growing crack tip, r, represents the position where the crack tip strain is defined and evaluated [3.12]. Figure 3.27 is a plot of the effect of the choice of r on the crack growth rate. The value, r, comes from the analytical strain distribution:

$$\varepsilon_p = \beta \frac{\sigma_{ys}}{E}\left[\ln\left(\frac{R_p}{r}\right)\right]^{\frac{1}{1-n}}$$

Here the strain varies with r. Following the derivation of the crack tip strain expression, r must be selected to determine the crack tip strain rate. The choice of r determines the magnitude of the crack tip strain. A value for r is chosen such that results for the crack growth rate are accurate. Combining the high uncertainty and the variation of crack growth rate with r results in a large contribution to error of the model. The

plateau beyond 0.05 mm is misleading because this plateau will occur beyond the appropriate value for r.

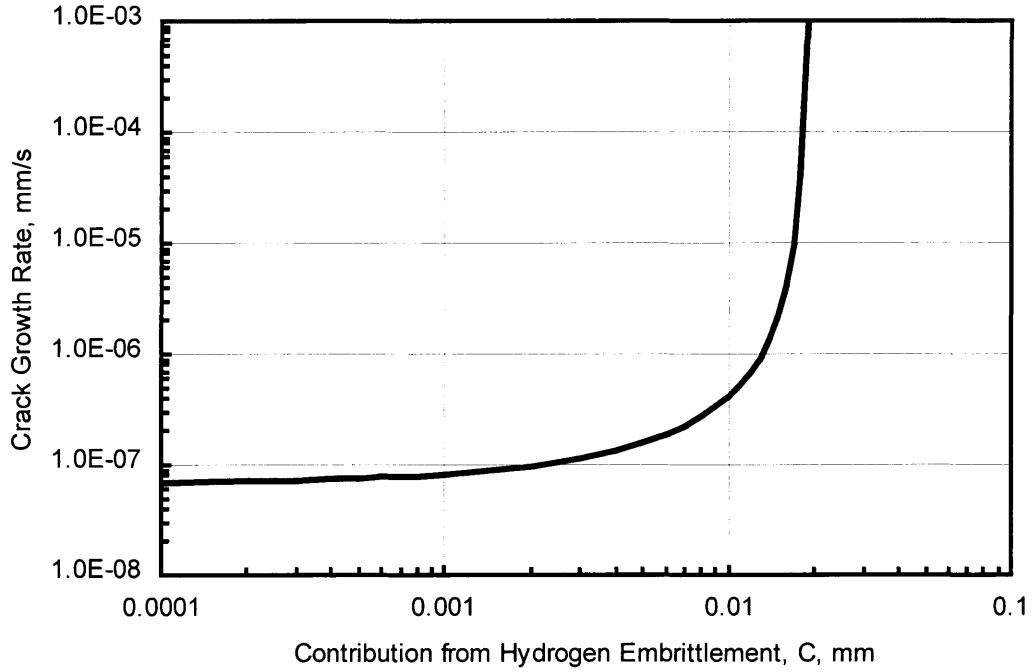

Figure 3.28. Crack growth rate versus contribution from hydrogen embrittlement for the base case parameters.

Figure 3.28, indicates the effect of C on the base case. The crack growth rate does not converge for $C \geq 0.02$ for this case. The shape of this curve is determined by the nature of the C term. C is added to the crack advance due to anodic dissolution. In this case, the anodic dissolution term dominates the equation when C is less than 0.001. When C is greater that 0.01, the hydrogen embrittlement contribution becomes significant. At $C = 0.02$ the iterative combination of the crack growth rate and the stress intensity factor will not converge. This indicates high uncertainty due to the hydrogen embrittlement contribution factor. Additionally the necessity of this value being

"reasonable" is indicated. It is important that this value not grow without bound as the concentration of hydrogen provided to the crack tip is increased.

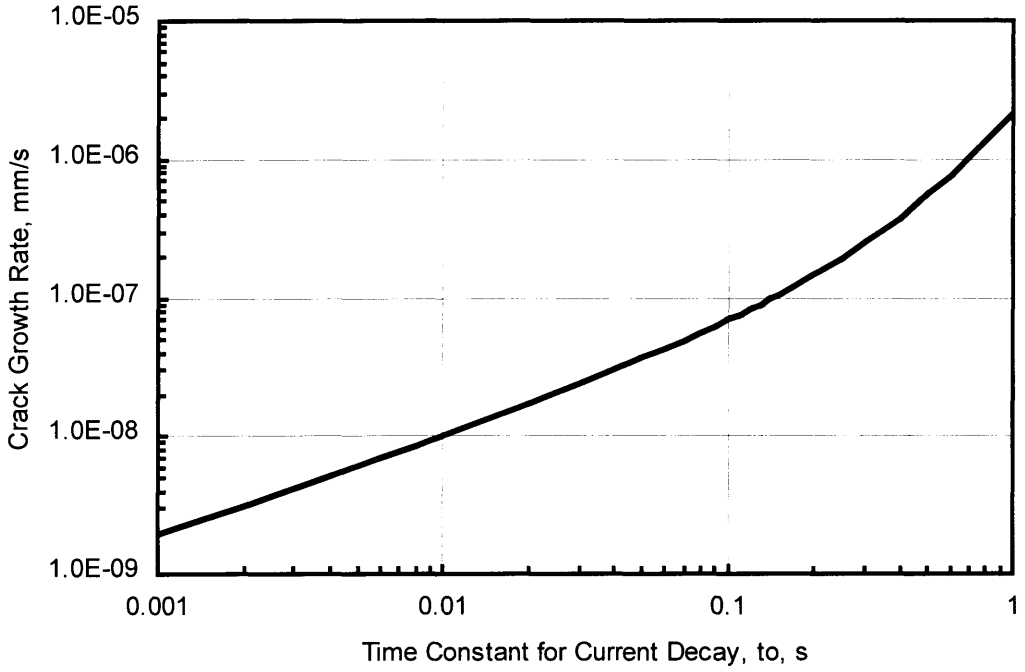

Figure 3.29. Crack growth rate versus current decay time constant for the base case parameters.

The time at which the passive film begins to form following rupture at the crack tip surface is another parameter determined experimentally from the current decay curve. Figure 3.29 shows the significance of the choice of t_o. The crack growth rate increases with increasing time constant because the dissolution at the crack tip occurs at the maximum density for a longer period. This formation of the passive film begins after about 0.1 seconds in most of the experiments on stainless steels in pure water at 288°C. However, on some current decay curves the time constant appears to be lower. The difference in crack growth rate between $t_o = 0.1$ and 0.01 is less than an order of

magnitude. Therefore, the contribution to the error from uncertainty in the time constant is medium relative to other contributions of error.

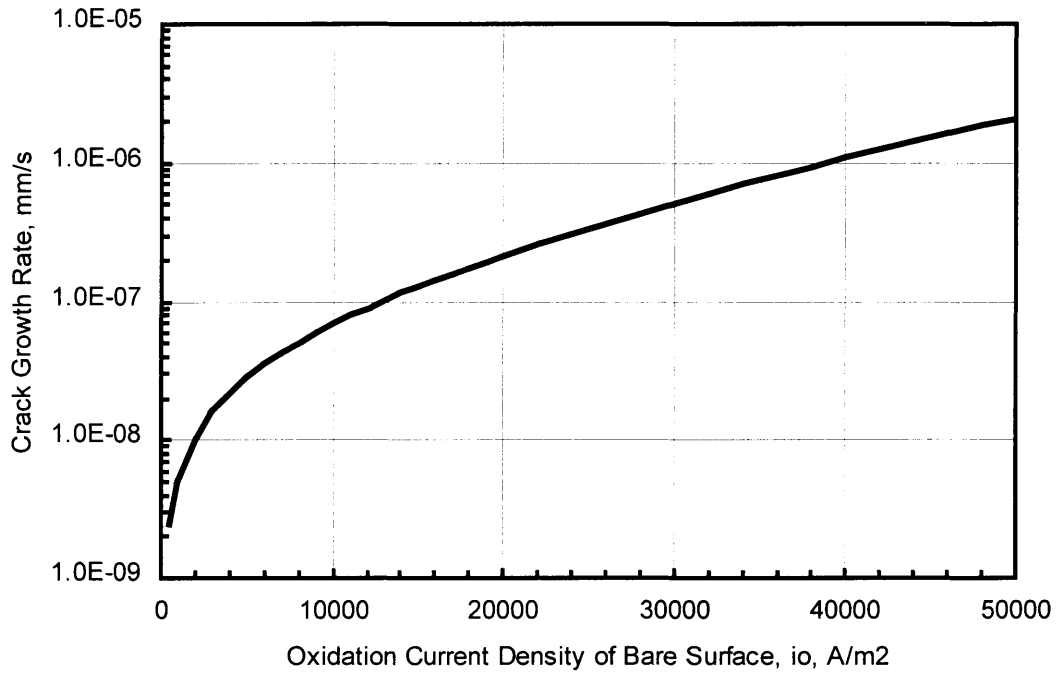

Figure 3.30. Crack growth rate versus oxidation current density of the bare surface for the base case parameters.

The oxidation current density of the bare surface is the maximum rate at which dissolution will occur following film rupture at the crack tip. As shown in Figure 3.30, the crack growth rate increases with increasing bare surface current density. Due to high uncertainty in the ratio of crack tip area to crack wall and outer surface area (anode/cathode ratio), the current density is not known with great certainty. High error may result from this uncertainty.

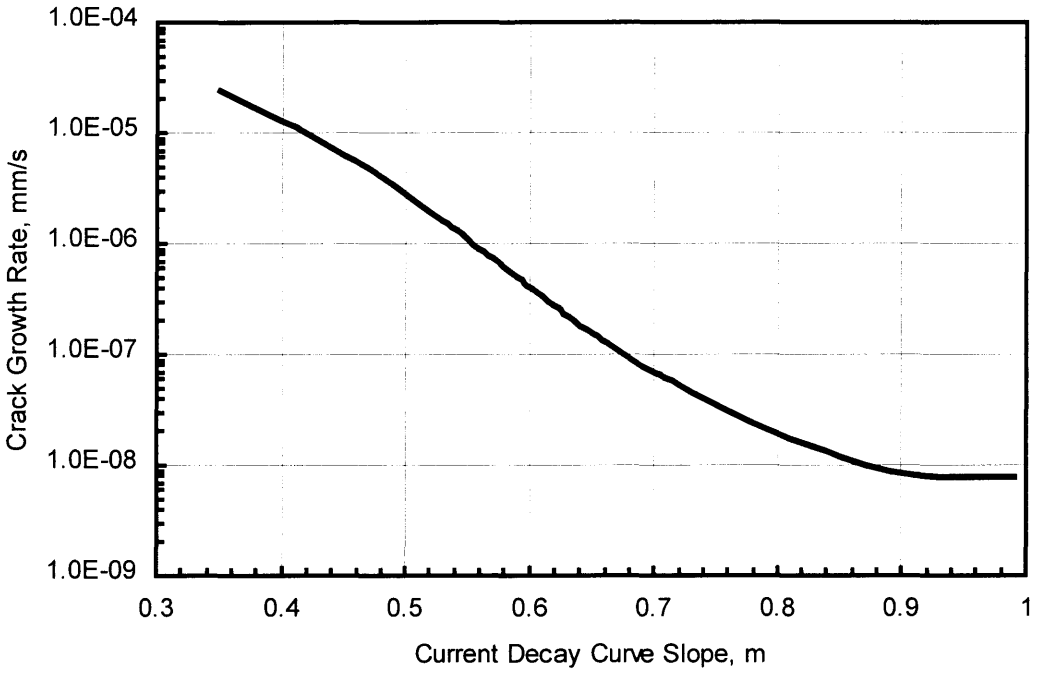

Figure 3.31. Crack growth rate versus current decay curve slope for the base case parameters.

The crack growth rate decreases with increasing current decay curve slope. As Figure 3.31 indicates, the effect of the current decay curve slope is extremely high. The dimensionless slope reaches a peak of -14 at 0.6. The current decay curve slope is determined from an empirical correlation, in which error will doubtless be present. Therefore, even with a small (and likely) 10% error in the current decay curve slope, the crack growth rate will vary significantly. Therefore, the current decay curve slope represents a large source of error in the crack growth rate.

In the base case, the current decay curve slope, m, equals 0.7. The current decay curve slope is found by the current decay curve correlation using the bulk conductivity at 25°C, the electrochemical potential, and the EPR value. Values for these which result in m = 0.7 might be conductivity = 0.3 μS/cm, ECP = 10 mV SHE, EPR = 15 C/cm^2. These

are reasonable values for a reactor with sensitized stainless steel, normal water chemistry, and somewhat high (but not out of spec.) conductivity. The same current decay curve will result with conductivity = 0.2 μS/cm, ECP = 105 mV SHE, and EPR = 15 C/cm^2. These are conditions where stress corrosion cracking is known to be a problem. The following plots bring the current decay curve into the sensitivity analysis by adding these values to the base case.

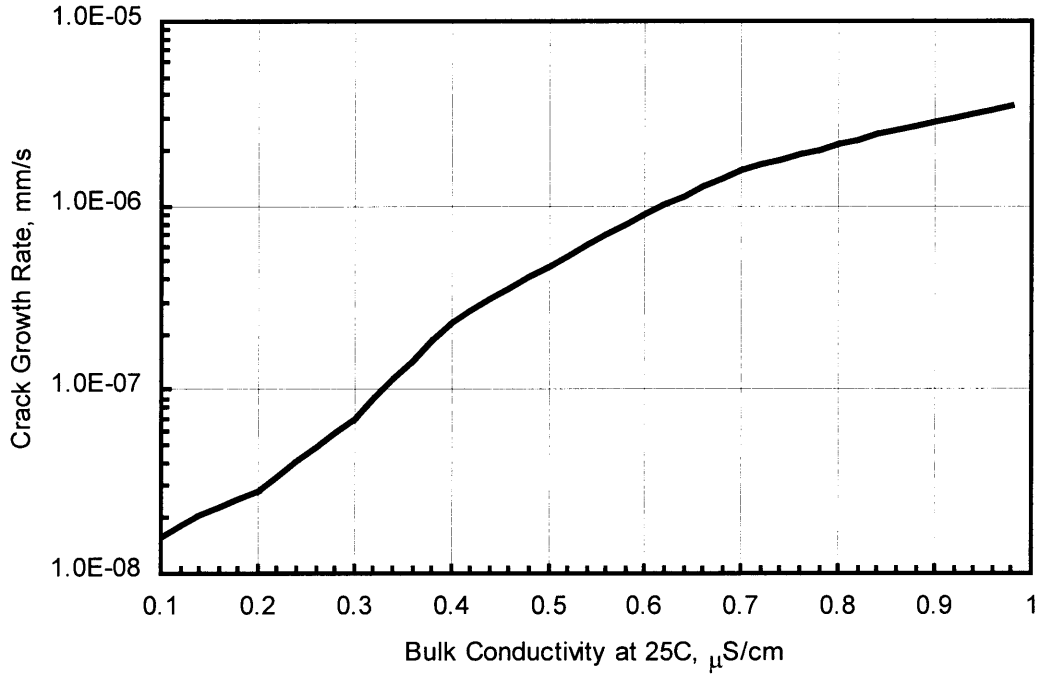

Figure 3.32. Crack growth rate versus bulk conductivity for the base case parameters, EPR = 15 C/cm^2, and ECP = 10 mV SHE.

Figure 3.32 indicates the effect of conductivity on cracking. The crack growth rate increases with conductivity. The conductivity at 25°C can usually be measured or predicted accurately within 0.1 μS/cm. Therefore, the effect of error in the conductivity on the crack growth rate is significant but not high.

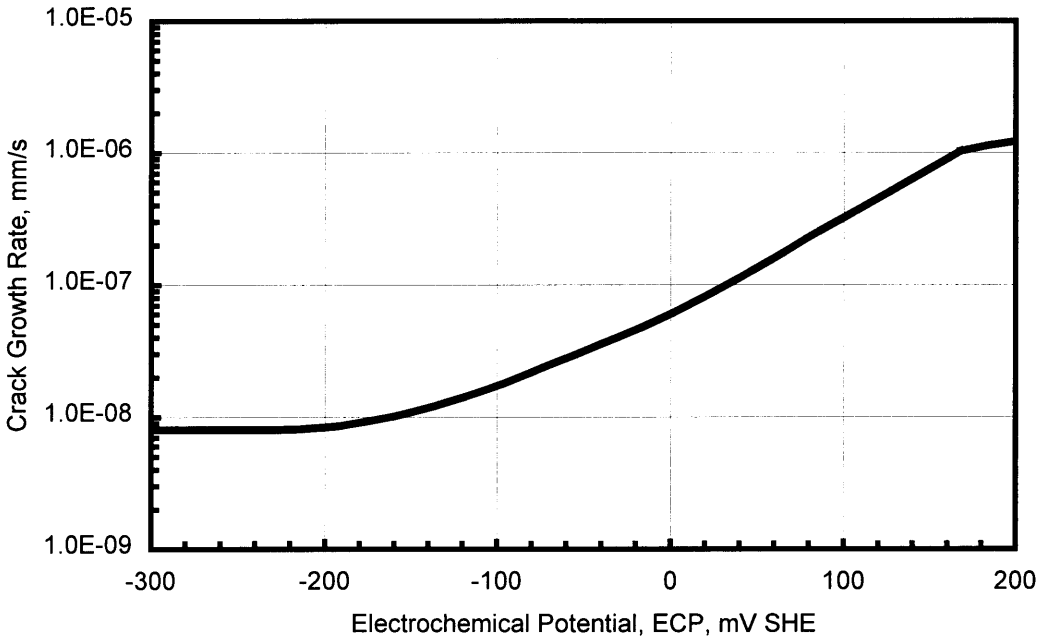

Figure 3.33. Crack growth rate versus electrochemical potential for the base case parameters, EPR = 15 C/cm^2, and conductivity = 0.3 μS/cm.

The effect of ECP on crack growth rate is shown in Figure 3.33. The crack growth rate increases with conductivity throughout the range of conductivities likely to be found a BWR. The error in the conductivity is likely to be less than 100 mV SHE. This error is high due to uncertainty in the effect of flowrate on ECP [3.40] as well as other sources of inaccuracy in the chemistry modeling. Therefore, the crack growth rate could vary by as much as half an order of magnitude due to error in ECP.

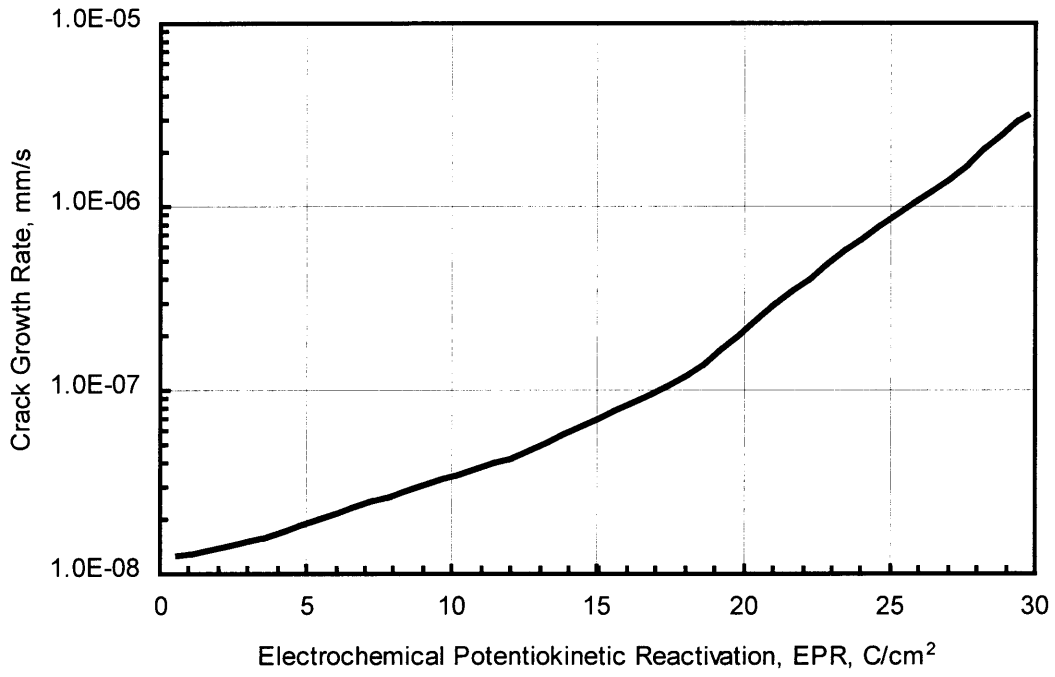

Figure 3.34. Crack growth rate versus EPR value for the base case parameters, ECP = 10 mV SHE, and conductivity = 0.3 μS/cm.

The crack growth rate increases with EPR as indicated in Figure 3.34. While this increase is not extreme, it is significant in light of the high uncertainty in the EPR value. Metals that are thermally sensitized to a low degree, such as those that are weld sensitized, are usually assumed to have EPR values of 15 C/cm^2 [3.11, 3.14]. These values actually might fall between 10 and 20 C/cm^2. The error in this case would be less than half an order of magnitude. Therefore, the EPR, ECP, and conductivity all provide medium sources of error. The combination of these three values to determine the current decay curve slope leads to the high error in that variable, as listed in Table 3.5.

The following table is a summary of the contribution of the error from each variable in the crack growth model. It describes the error as low, medium low, medium high, or high for each variable.

Table 3.5. Contibution level in crack growth rate error.

Variable	Contribution to Error
λ, Plastic zone size constant	Low
β, Analytical strain distribution constant	Low
M, Metal atomic mass	Low
ρ, Metal density	Low
z, Oxidation state of dissolution	Low
ε_f, Passive film rupture strain	Medium High
E, Young's modulus	Low
σ_y, Yield strength	Medium Low
n, Strain hardening exponent	Medium High
K, Stress intensity factor	Medium Low
K`, Stress intensity factor rate of change	Medium High
r, Distance from growing crack tip	High
C, Hydrogen embrittlement cleavage factor	High
t_o, Time constant for current decay	Medium
i_o, Bare surface oxidation current density	High
m, Oxidation current decay curve slope	High

3.6. Graphical User Interface

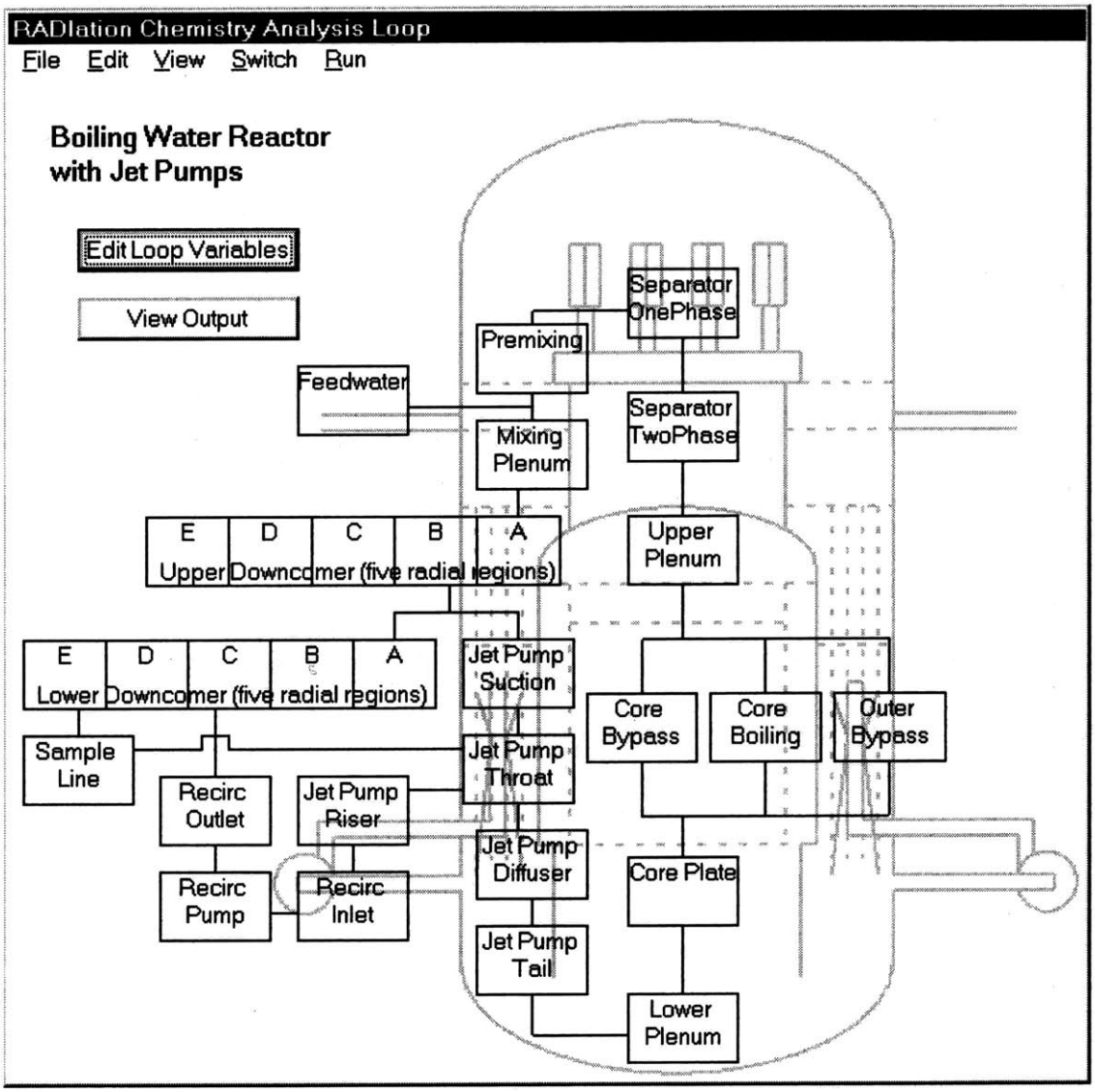

Figure 3.35. Graphical user interface main window displaying nodal flow of BWR3 components (gray and white reversed for clarity).

In order to create a usable program that would be valuable to utilities and future researchers a graphical user interface (GUI) was created to guide the user through the various models that comprise the IEDM. The interface greatly enhances the usability of the model by taking the user through a wizard-like progression where the user chooses which models are relevant to the case being studied. The progression allows the models

to share information such as flux, fluence and metal properties so that data need only be entered once. The user interface allows for two types of plant chemistry models. One modeled after a boiling water reactor (BWR) type III with jet pumps and the other a BWR type I where all the downcomer flow goes through the recirculation pumps. The plant chemistry model is actually highly flexible and has been used in this thesis to model an experimental loop. It is also possible to model pressurized water reactors (PWR) with the plant chemistry model. However, the chemistry information has not been compiled and the GUI does not contain a nodal setup for PWR systems.

When the GUI is opened a nodal model of the primary side of a BWR is produced. This is illustrated in Figure 3.35. After selecting whether to model with jet pumps or direct recirculation, the dimensions of each reactor component are inputted. Additionally the power dissipated and neutron and gamma flux levels are required for each component where they are significant. From this main window, other windows can be opened to view output and to run the radiation induced segregation, radiation hardening, and crack growth models. Figure 3.36 is the main page for the crack growth model. When this window is loaded a choice is made whether to load input values from the plant chemistry model, then a window pops up asking whether the radiation induced segregation model should be run. From the crack growth model window, the hardening model and the current decay curve correlation can be run.

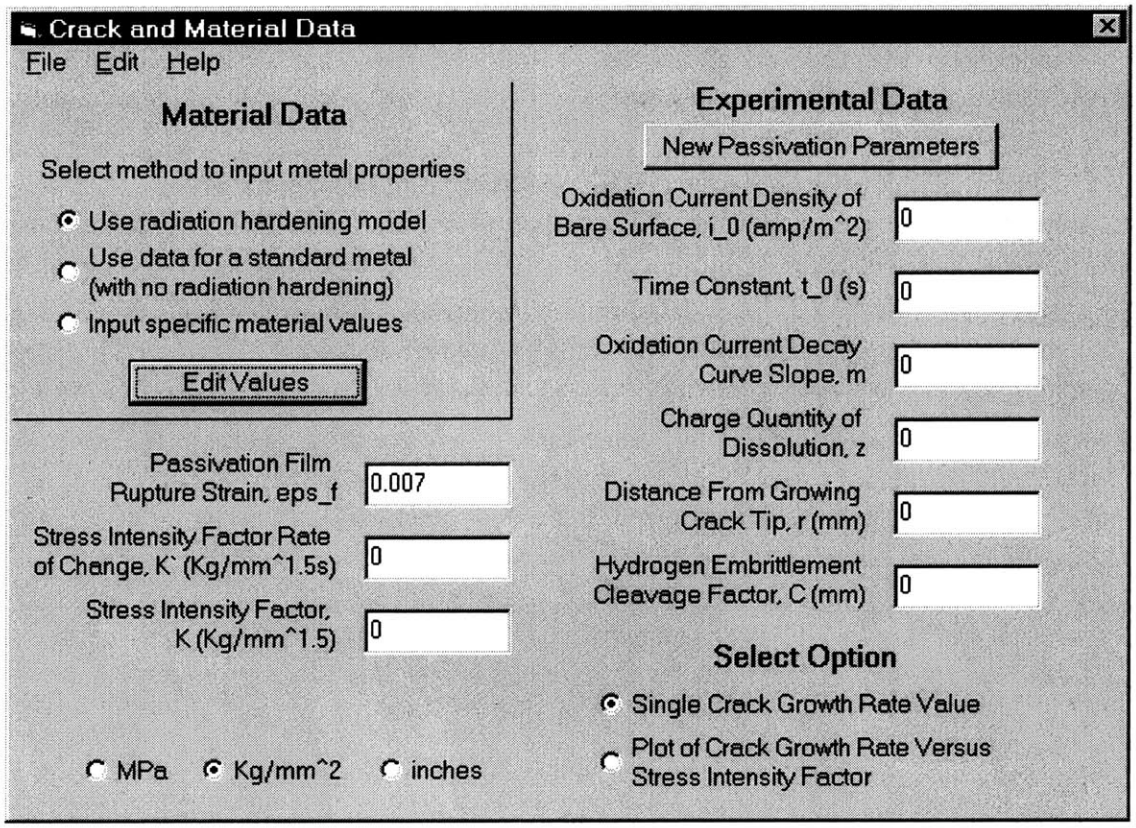

Figure 3.36. Crack growth model physical and mechanical input parameter window from GUI.

The GUI provides a framework in which an inexperienced user can quickly learn to us the IEDM to characterize the effect of irradiation on the long term cracking of boiling water nuclear power plant components. This allows the models developed here as well as those developed previously to come out of the lab and be used as tools to advance the understanding of flux and fluence effects on life prediction.

3.7. References

[3.1] Gerberich W. W. and Chen, S., Environmentally-Induced Cracking of Metals, Fundamental Processes: Micromechanics, Environmentally-Induced Cracking of Metals, NACE 10, (Oct. 1988) p. 167.

[3.2] Gerberich W. W., Davidson D. L., and Kaczorowski, M., Experimental and Theoretical Strain Distributions for Stationary and Growing Cracks, Journal of Mechanical Physics of Solids, V. 23, N. 1 (1990) pp. 87-113.

[3.3] Gao, Y.-C., Hwang, K.-C., "Elastic Plastic Fields in Steady Crack Growth in a Strain-Hardening Material." Advances in Fracture Research, Pergamon Press (1981) pp 669-682.

[3.4] Shoji, T., Suzuki, S., Ballinger, R., Theoretical Prediction of SCC Growth Behavior, Threshold and Plateau Growth Rate. 7th International Symposium on Environmental Degradation of Materials in Nuclear Power Plant-Water Reactors V. 1 (Aug. 1995) pp. 881-891.

[3.5] Ford F. P., The Crack-Tip System and Its Relevence to the Prediction of Cracking in Aqueous Environments, Environmentally-Induced Cracking of Metals, NACE 10, (Oct. 1988) p. 139.

[3.6] Dean, R. and Hutchinson, J. W., Fracture Mechanics, 12th ASTM Conference p.383.

[3.7] Lan, P. S., McMeeking, R. M., Journal of the Mechanical Physics of Solids Vol. 32. (1984) p. 395.

[3.8] Ma, B. M. "Nuclear Reactor Materials and Application," Van Nostrand Reinhold Company (1983).

[3.9] Andresen, P. L., Fracture Mechanics Data and Modeling of Environmental Cracking of Nickel-Base Alloys in High-Temperature Water. Corrosion V. 47 (Dec. 1991) pp. 917-38.

[3.10] Andresen, P. L., Ford, F. P., Modeling & Prediction of Irradiation Assisted Stress Corrosion Cracking. 7th International Symposium on Environmental Degradation of Materials in Nuclear Power Plant-Water Reactors V. 2 (Aug. 1995) pp. 893-908.

[3.11] Ford, F. P., Taylor, D. F., Andresen, P. L., Ballinger, R. G. "Corrosion-Assisted Cracking of Stainless and Low-Alloy Steels in LWR Environments", EPRI, NP-5064M, (1987).

[3.12] Satoh, T., Nakazato, T., Moriya, S., Suzuki, S., Shoji, T., Quantitative Predication of Environmentally Assisted Cracking Based on a Theoretical Model and Computer Simulation. Journal of Nuclear Materials Proceeding of the 1997 8th International Conference on Fusion Reactor Materials (1997) pp. 258-263.

[3.13] Ford, F. P., Quantitative Prediction of Environmentally Assisted Cracking. Corrosion. V. 52, N. 5 (1996) pp. 375.

[3.14] Ford F. Peter, Andresen Peter L., Development and Use of a Predictive Model of Crack Propagation in 304/316L, A533/A508 and Inconel 600/182 Alloys in 288 C Water, Environmental Degradation of Materials in Nuclear Power Systems,(1988) p. 789-800.

[3.15] Angeliu, T. M., Andresen, P. L., Effect of Zinc Additions on Oxide Rupture Strain and Repassivation Kinetics of Iron-Based Alloys in 288(Degree)C Water. Corrosion V. 52 (Jan. 1996) pp.28-35.

[3.16] Jones, Denny A., "Principles and Prevention of Corrosion," Prentice Hall, (1992).

[3.17] Psaila-Dombrowski, M. J., Modeling of Crack and Crevice Chemistry in Light Water Reactor Environments, Ph.D. thesis, Nuclear Engineering Department, Massachusetts, Institute of Technology, 1990.

[3.18] Uhlig, H. H., Revie, R. W., Corrosion and Corrosion Control, John Wiley and Sons, Inc. (1985).

[3.19] Andresen, P. L., Ford, F. P., Use of Fundamental Modeling of Environmental Cracking for Improved Design and Lifetime Evaluation. Journal of Pressure Vessel Technology V. 115 (Nov. 1993) pp. 353-8.

[3.20] Andresen, P. L.; Ford, F. P., Response to "On the Modeling of Stress Corrosion Cracking of Iron and Nickel Base Alloys in High Temperature Aqueous Environments." Corrosion Science. V. 38, N. 6 (1996) pp. 1011.

[3.21] Ford F. P., The Crack-Tip System and Its Relevence to the Prediction of Cracking in Aqueous Environments, Environmentally-Induced Cracking of Metals, NACE 10, (Oct. 1988) p. 139.

[3.22] MacDondald, D.D., Eghan, A. K., Szklarska-Smialowska, Z., "Stress Corrosion Cracking of Sensitized AISI 304 Stainless Steel in Oxygenated High Temperature Chloride Solutions Containing Cupric (Cu^{2+}) and Lead (Pb^{2+}) Ions.", Corrosion, Vol. 41, No. 8, (1985) pp. 474-484.

[3.23] Andresen, P. L., Indig, M. E., "Effects of Impurities and Supportning Electrolytes On SCC of 304 Stainless Steel in High Temperature Aqueous Environments, Corrosion. Vol. 38, No. 10 (1982) pp. 531-541.

[3.24] Lide, D. R. ed., CRC Handbook of Chemistry and Physics (1994).

[3.25] Matsumoto J., Electrochemistry of Intermetallic Phases of Ni-Cr-Fe Alloys in Aqueous Environment, S.M. thesis, Nuclear Engineering Department, Massachusetts, Institute of Technology, 1991.

[3.26] Birnbaum, H. K. Mechanisms of Hydrogen-Related Fracture of Metals, Environmentally-Induced Cracking of Metals, NACE 10, (1988) pp. 21-.29

[3.27] Parkins R. N., Stress Corrosion Cracking, Environmentally-Induced Cracking of Metals, NACE 10, (1988) p. 1.

[3.28] Jani, S. C., Marek, M., Hochman, R. F., and Meletis, E. I., A Model for Transgranular Stress Corrosion Cracking in Austenitic Stainless Steel, Environmentally-Induced Cracking of Metals, NACE 10, (Oct. 1988) p. 541.

[3.29] Gaudett, M.A. and Scully, J.R., Applicability of bond percolation theory to intergranular stress-corrosion cracking of sensitized AISI 304 stainless steel, Metallurgical Transactions A (Physical Metallurgy and Materials Science), Vol. 25A No. 4 (1994) pp. 775-787.

[3.30] Bruemmer, S. M.; Charlot, L. A.; Arey, B. W., Sensitization Development In Austenitic Stainless Steel: Correlation Between Stem-Eds And Epr Measurements, Corrosion Vol. 44 No. 6 (1988) pp. 328-333.

[3.31] Clarke, W.L., Cowan, R.L., and Walker, W.L., Comparative Methods for Measuring Degree of Sesitization in Stainless Steel, Intergranular Corrosion of Stainless Alloys ASTM STP 656, R. F. Steigerwald, Ed., American Society for Testing and Materials, (1978) p.p. 99-132.

[3.32] Bruemmer, S. M.; Charlot, L. A., Development Of Grain Boundary Chromium Depletion In Type 304 And 316 Stainless Steels, Scripta Metallurgica Vol. 20 No. 7 (1986) pp. 1019-1024.

[3.33] Gaudett, M.A. and Scully, J.R., Distributions of Cr depletion levels in sensitized AISI 304 stainless steel and its implications concerning intergranular corrosion phenomena, Journal of the Electrochemical Society Vol. 140 No. 12 (1993) pp. 3425-3435.

[3.34] Ahn, M.-K., Kwon, H.-S., Lee, J.-H., Predicting Susceptibility of Alloy 600 to Intergranular Stress Corrosion Cracking Using a Modified Electrochemical Potentiokinetic Reactivation Text. Corrosion, Vol. 51 No. 6 (1995) pp. 441-449.

[3.35] Katsura, R., Kodama, M., and Nishimura, S., DL-EPR study of neutron irradiation in type 304 stainless steel, Corrosion Vol. 48 No. 5 (1992) pp. 384-390.

[3.36] Flores, C. D. "Evaluation of Radiation Induced Segregation in Fe-Ni-Cr Alloys," M.S. thesis, Nuclear Engineering Department, Massachusetts, Institute of Technology, 1994.

[3.37] Was, G. S., Rajan, V. B., "On the Relationship Between the EPR Test, Sensitization, and IGSCC Susceptibility," Corrosion, Vol. 43, (1987) pp. 576-579.

[3.38] Was, G. S., "Synergistic Effects of Thermal Treatment and Cathodic Polarization in the Fatigue Crack Growth Behavior of Inconel 600." Sc.D. thesis, Nuclear Engineering Department, Massachusetts, Institute of Technology, 1980.

[3.39] Jennsen, A., Ljungberg, L. G., "Irradiation Assisted Stress Corrosion Cracking of Stainless Alloys in BWR Normal Water Chemistry and Hydrogen Water Chemistry," Proceedings of the Sixth International Symposium on Environmental Degradation of Materials in Nuclear Power Systems-Water Reactors, (Aug. 1993) pp. 547-553.

[3.40] Grover, D. J., "Modeling Water Chemistry and Electrochemical Corrosion Potentials in Boiling Water Reactors." SM thesis, Nuclear Engineering Department, Massachusetts, Institute of Technology, (1996).

4. Verification

In order to verify the IEDM, a large quantity of data has been collected from the literature. Some of this data represents the effect of various parameters on the crack growth rate. The problem with the crack growth rate data is that incomplete information is given on the parameters of the experiment. Data in the literature is printed with only the information necessary to verify the model or effect being described in the particular paper. Because this model accounts for more effects and requires a wider range of inputs than any other model, none of the data in the literature can be used to verify the IEDM as a whole. There are two solutions to this problem. The first is to verify the each model separately, overlapping where possible.

By verifying each model separately, the accuracy of each model can be verified to discover the sources of error. First, the radiation induced segregation, and radiation hardening models will be verified. Then the verification of the plant chemistry model will be discussed. Finally, a great deal of data will be used to verify the various aspects of the crack growth model. Most of this data will overlap with the current decay correlation and some of the verification data will overlap with other models as well. Data received from the Electric Power Research Institute will be used to verify a significant portion of the IEDM model. However, assumptions are still necessary to compare this data to the IEDM.

The second way to verify the entire model solves the problem above where incomplete information is given. An ideal battery of laboratory experiments for

verification has already been completed. Specifically, the doctoral thesis work of Bruce Hilton as part of the MIT IASCC project includes four experiments in which stress corrosion cracking occurred. Two important elements can be analyzed with this data. The first is the connection between the bulk chemistry model and the crack growth model. An input file was developed for the plant chemistry model (RadiCAL) for the BWR simulation loop used to conduct the IASCC experiments. The second element is difference between the effect of thermal segregation and radiation induced segregation. This verification is at the end of this chapter.

4.1. Radiation induced segregation

The results of the radiation induced segregation model have been compared to several experimentally measured profiles on alloys exposed to neutron irradiation. Agreement with published data is excellent. Of particular importance are the chromium concentrations near the grain boundaries, which are more accurately modeled as compared to previous RIS modeling efforts in the literature [4.1].

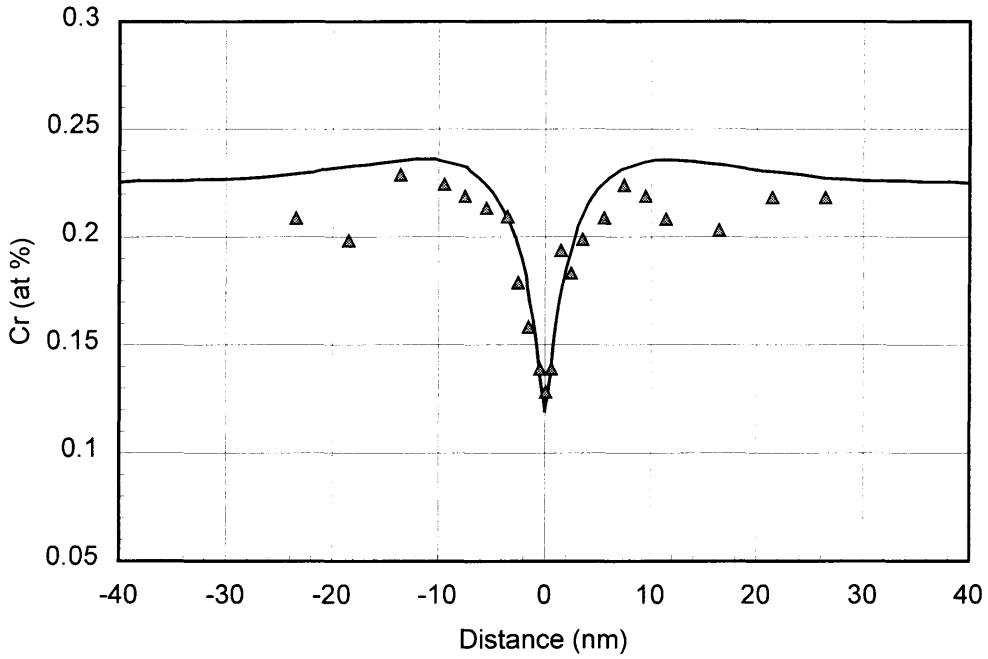

Figure 4.1. Measured chromium profile across a grain boundary and RIS model output. 20Cr-25Ni-Nb irridiated in a SGHWR, 298°C [4.2].

Figure 4.1 [4.2] and Figure 4.2 [4.3] are plots that illustrate the accuracy with which the grain boundary chromium profiles are modeled. The lines on the plots represent the model calculations and the points represent published measured data. In Figure 4.1, the solid line is the results from the RIS model and the triangles are actual data from 20Cr-25Ni-Nb irradiated at 289°C in a steam generating heavy water reactor. In Figure 4.2, the triangles are data from 20Cr-25Ni-Nb irradiated to 1 displacement per atom, at 354°C in an advanced gas-cooled reactor. In addition to looking at chromium profiles, the nickel profiles where solved with equal success by the radiation induced segregation model.

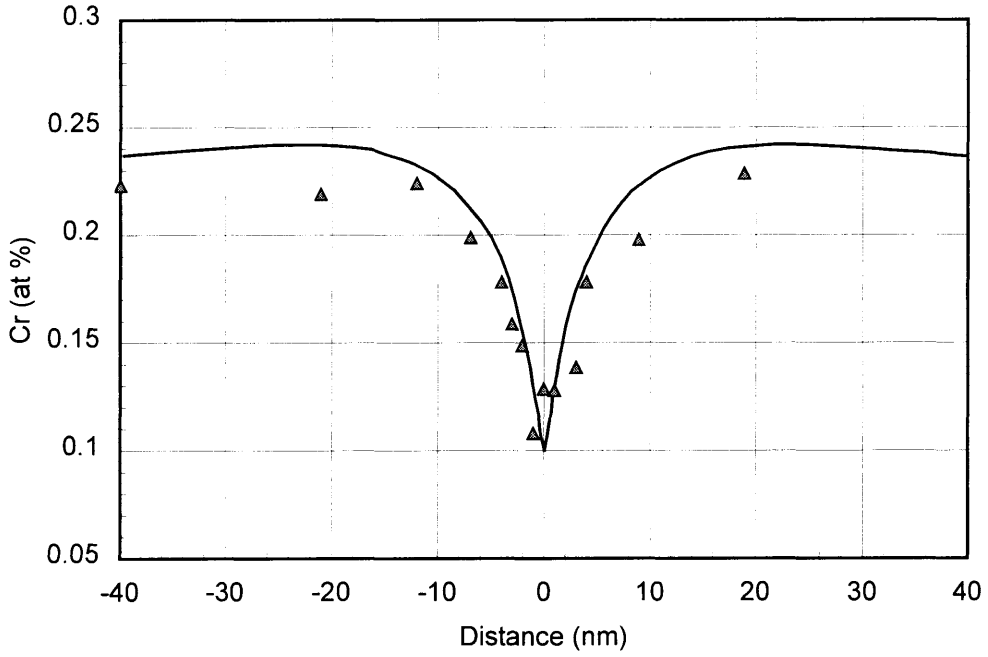

Figure 4.2. Measured chromium profile across a grain boundary and RIS model output. 20Cr-25Ni-Nb irridiated in a AGR, 1 dpa, 354°C [4.3].

4.2. Radiation Hardening

The radiation hardening model was developed from two data sets for radiation hardening of austenitic stainless steel (304 and 316) at reactor coolant temperatures [4.4, 4.5]. Figure 4.3 shows plots of data from the literature used to fit the statistical model (triangles) and data from the model (lines). The scatter in this data represents range of possible values associated with radiation hardening as well as variance in initial hardness, and other experimental parameters.

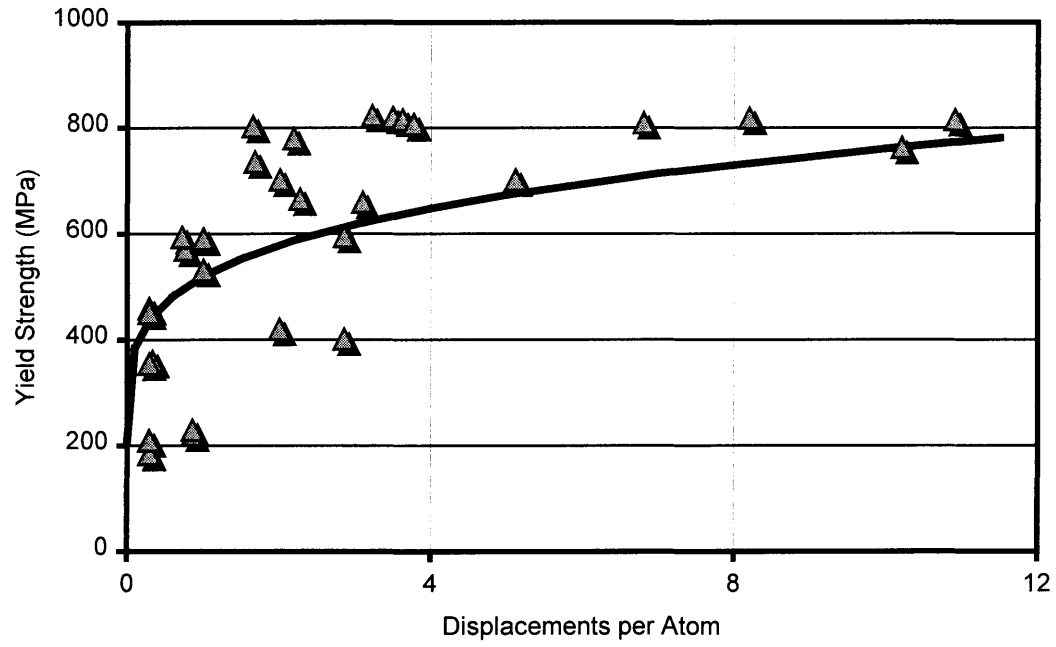

Figure 4.3. Yield Strength versus DPA for annealed stainless steel irradiated at 288°C showing experimental data (triangles)[4.4, 4.5] and model output (lines).

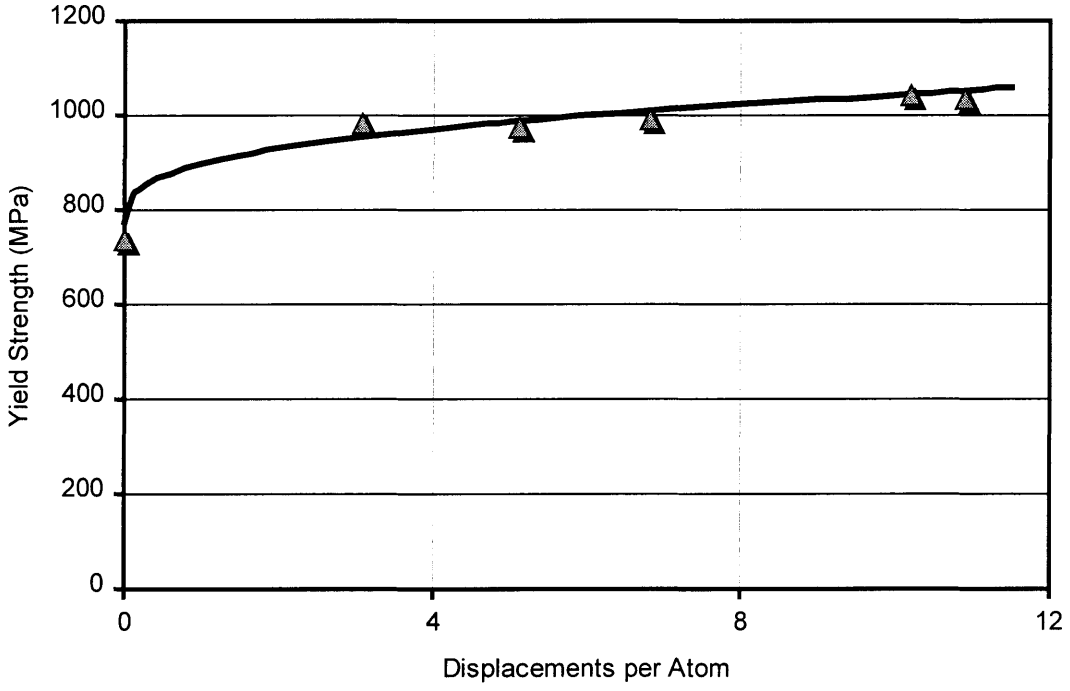

Figure 4.4 Yield Strength versus DPA for cold-worked stainless steel irradiated at 288°C showing experimental data (triangles)[4.4, 4.5] and model output (lines).

Additional plots are presented to verify the data. Rather than containing only data for stainless steel 304 and 316, these plots contain data for a number of Fe-Ni-Cr alloys, including super-alloys developed for fusion application. In addition, because the super-alloy data is from research based on fusion, the samples were irradiated at temperatures outside the optimal range for the statistical model [4.6]. The first verification plot, Figure 4.5, shows measured data for stainless steel 304 and 316 irradiated at 288°C versus model output [4.7]. The model output is shown for initial yield strengths of 200 and 300 MPa.

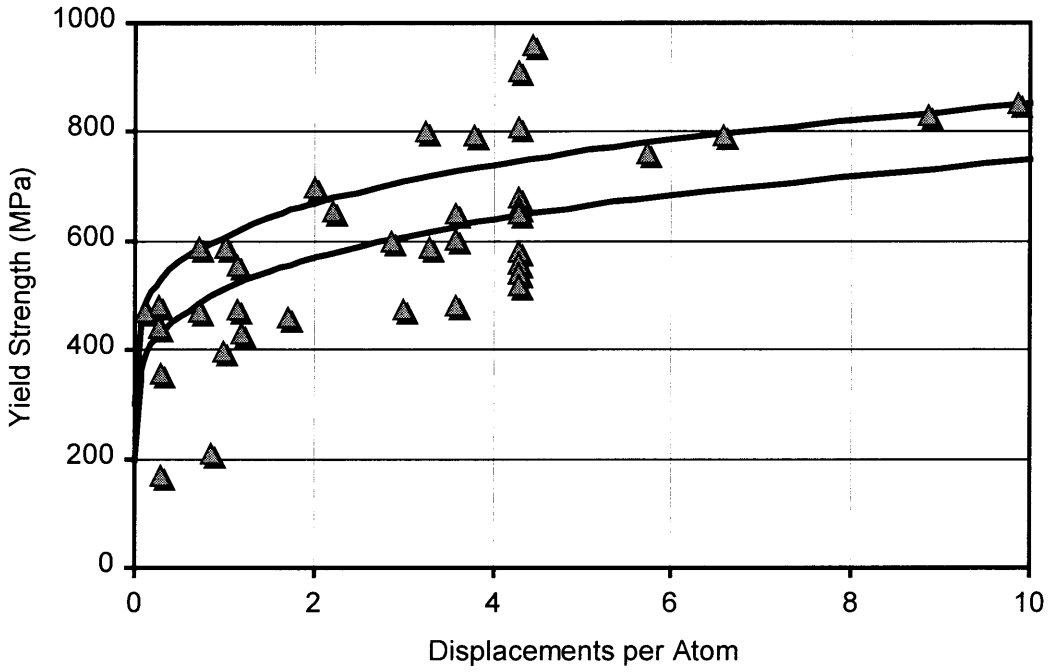

Figure 4.5. Yield Strength versus DPA for annealed stainless steel irradiated at 288°C showing experimental data (triangles)[4.7] and model output (lines).

The second verification plot, Figure 4.6, also represents annealed data. This data is for Fe-Ni-Cr super-alloys irradiated at high temperatures (365, 465, 490, and 600°C) [4.6]. This data is not fitted as well as that irradiated at 288°C because the hardening model contains a very simple relationship for temperature which is not valid well outside

of the operating conditions for light water reactors. Figure 4.6 does indicate that agreement with measured data for the hardening of a wide range of Fe-Ni-Cr alloys is good for the hardening model.

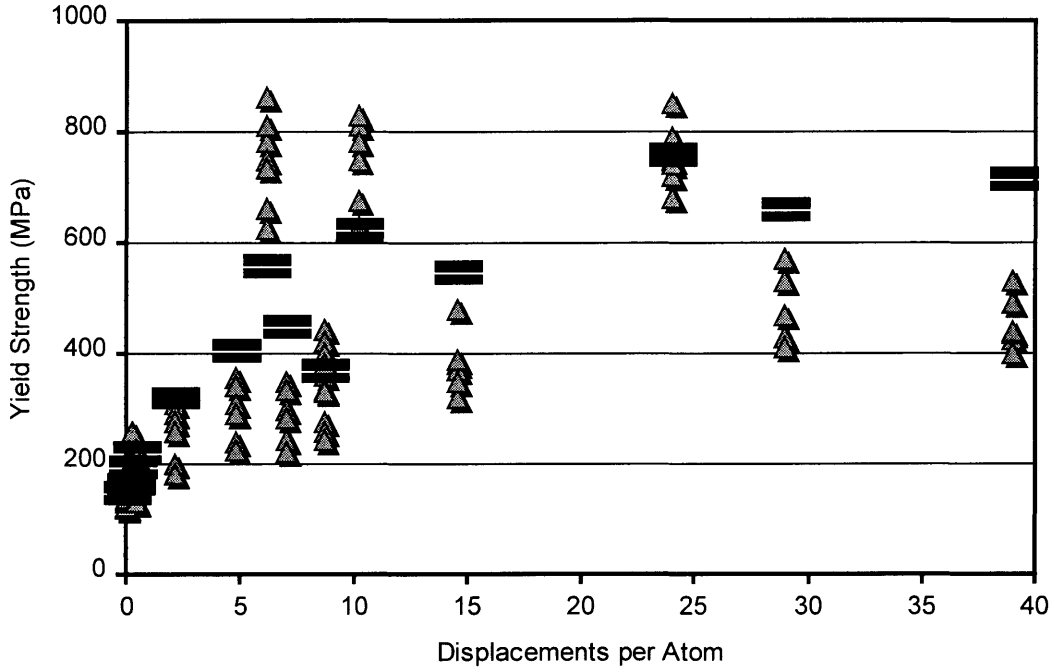

Figure 4.6. Yield Strength versus DPA for annealed Fe-Ni-Cr super-alloys irradiated at high temperatures showing experimental data (triangles)[4.6] and model output (lines).

Figure 4.7 plots irradiation hardening data for cold-worked Fe-Ni-Cr super-alloys against model predictions. This data is from the same high temperature tests as that shown in Figure 4.6. Again there is difficulty fitting the data at the highest temperatures.

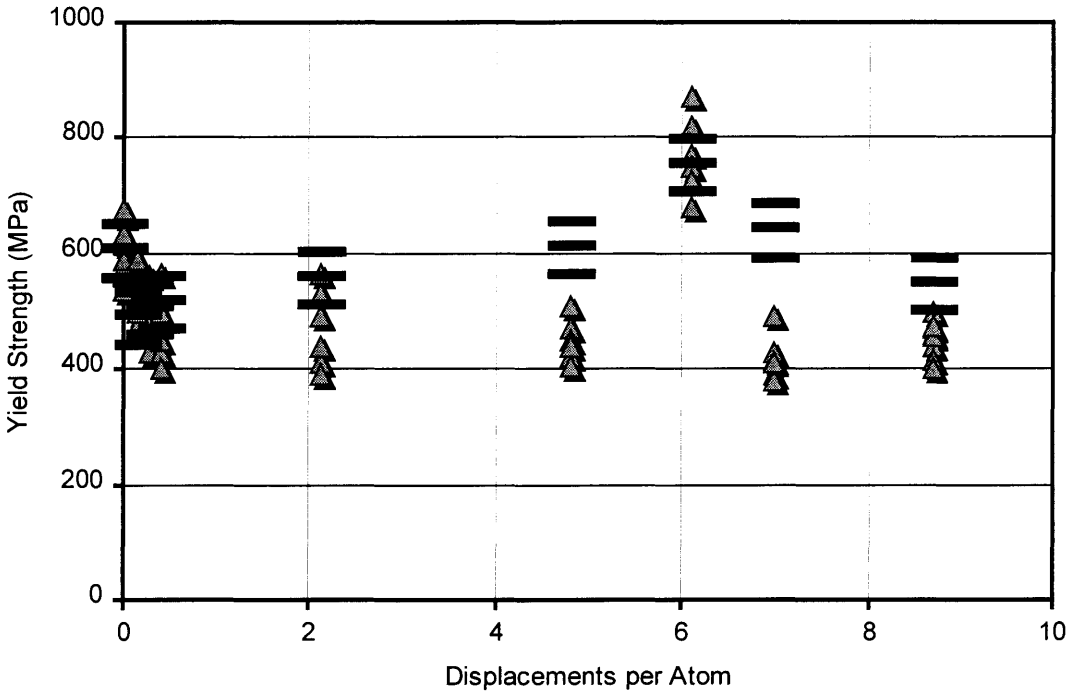

Figure 4.7. Yield Strength versus DPA for cold-worked Fe-Ni-Cr super-alloys irradiated at high temperatures showing experimental data (triangles)[4.6] and model output.

Good agreement with the hardening model for cold-worked is also evidenced in Figure 4.8 for irradiated cold-worked 316 stainless steel. The hardening for these experiments was due to irradiation at 35°C. Therefore, the model output will be somewhat high for low irradiation levels as seen in this data. It might seem that the temperature effect should be adjusted so that it is nonexistent for 0 dpa and increases rapidly up to full strength at 1 dpa. This would also fix the intercept for temperature values other than 288°C. This was not added to the model because it would imply that the model is accurate over a wide range of temperatures, which it is not. It is better to leave the model simple and ensure that it is not used for temperatures outside the range of 200 to 350°C. Because the entire IEDM is based on light water reactor conditions, it is expected that the hardening model be used only in these instances as well.

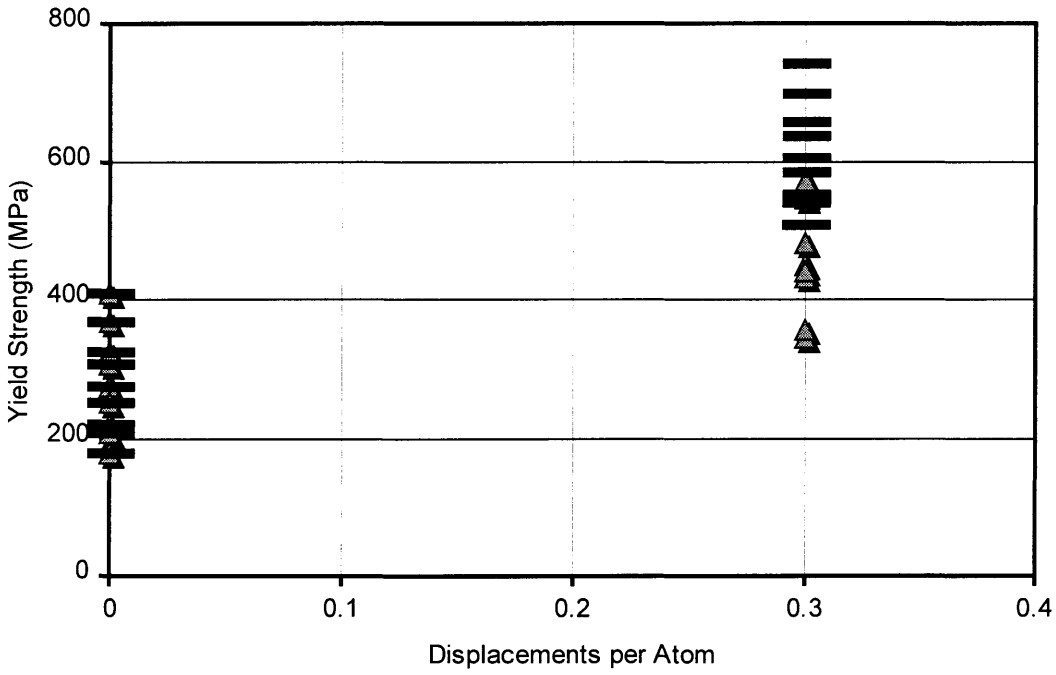

Figure 4.8. Yield Strength versus DPA for cold-worked stainless steel irradiated at 35□C showing experimental data (triangles)[4.8] and model output (lines).

The strain hardening exponent verification is shown in Figure 4.9. However, there is a serious problem with this plot: It is the same data that was used to develop the relationship between yield strength and strain hardening exponent. This was necessary because these two data sets were the only ones at 288°C that were found in an extensive literature search.

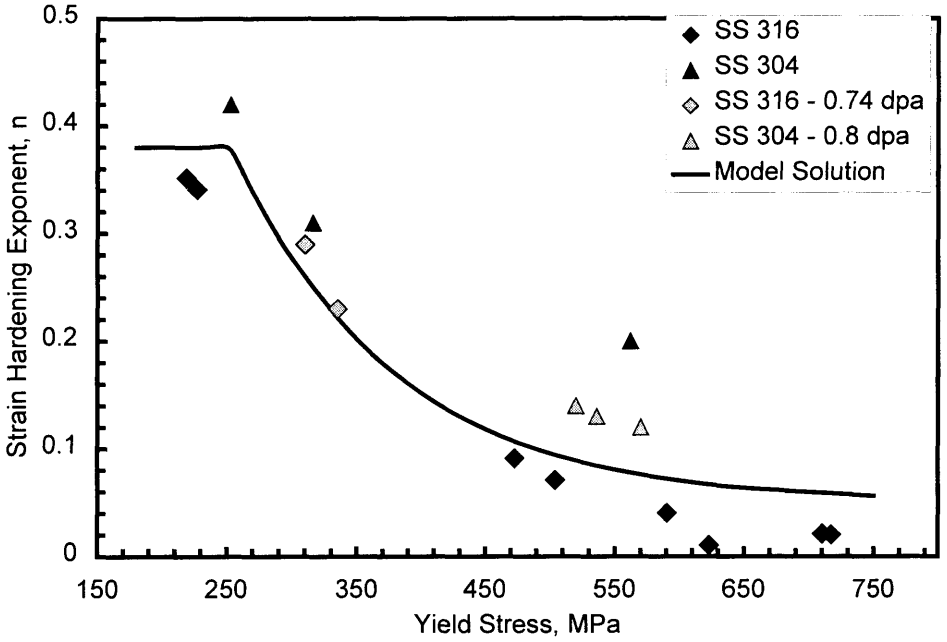

Figure 4.9. Strain hardening exponent versus yield stress data at reactor coolant temperature with model solution line [4.9,4.10].

Another check of any model is whether it is reasonable. It is reasonable that the strain hardening exponent decreases with increasing yield strength. In addition, the range of values from 0.38 to 0.05 is reasonable. The discontinuity at 255 MPa is necessary because 0.38 is the value of the strain hardening exponent used here when no cold work or irradiation hardening has occurred. During radiation hardening the yield stress will initially increase rapidly leading to a decrease in strain hardening exponents.

4.3. Radiation Chemistry Analysis Loop

The RadiCAL model supplies the electrochemical potential (ECP) to the crack growth model. It also determines differences in conductivity due to reactor operation regimes and radiation effects. These two inputs must be accurate if the model is to be used as it is intended to model the entire reactor over a wide range of conditions and operating times. The radiolysis model has been verified in previous work [4.11, 4.12].

Additionally, test cases have been run following each stage of model development to ensure that mistakes are not introduced to the code.

Three main techniques were used to verify the code when the model was initially implemented [4.11]. The first method was to use the Bateman equations, which describe the kinetics of radioactive decay. Because the Bateman equations are analytically solvable, the chemical kinetics routines could be thoroughly verified [4.11].

The second technique was to use an input file for a process that was very well understood. An input file that described the burning of a cesium flare was used to test the model. This method had been used to test previous radiolysis models as well [4.13].

The third technique to verify the radiolysis model is similar to that used to verify the current implementation. The model is compared to previous modeling efforts and errors are eradicated from both models until the results are reasonably similar. When the RadiCAL model was originally coded it was compared to the MITIRAD radiolysis simulator for a simple experimental loop case [4.11]. After several rounds of bug fixing, the codes revealed similar results that were also physically reasonable [4.11].

The empirical model for electrochemical potential (ECP) was added to the RadiCAL model in a significant subsequent revision [4.12]. While accuracy of the concentrations of species and flow velocities in the updated model could be validated by comparison to previous versions of the model, it is extremely important that the ECP model be verified as well. This is especially important in light of the fact that this is the key variable from the plant chemistry model used by the crack growth model in the IEDM.

The ECP model was developed by Lin et. al. [4.14] using data for the effect of O2 and H2O2 on a rotating cylinder electrode in an autoclave containing high purity water at 288°C. The data collected from the experimental setup had high precision and, like any complex empirical model, the model predicted the test data with high accuracy. A real test of the model was to compare it to actual reactor data. However, the only comparison that was made was between the output of the entire plant chemistry model (including the ECP model) and actual reactor data. While this is not the best way to verify the ECP correlation, it does indicate the validity of the entire RadiCAL model. Figure 4.10 and Figure 4.11 compare actual reactor data for the effect of hydrogen water chemistry on ECP in the core bypass region to RadiCAL output.

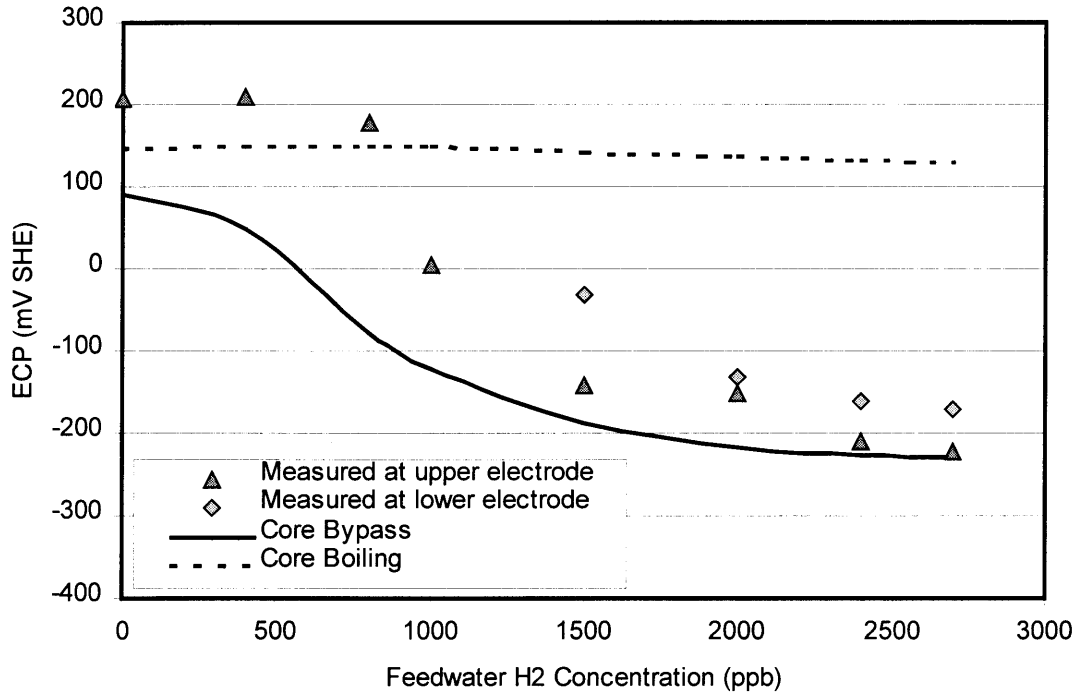

Figure 4.10. Reactor data (symbols) for upper core bypass region and RadiCAL model ECP output using BWR3 input file [4.14].

Figure 4.10 shows reactor data for the core bypass region near the top of the active fuel. Plotted with this data are two curves from the RadiCAL model output using the BWR3 standard input file. The data used is from the next to the last spatial step in the core bypass and core boiling regions. This plot indicates fair agreement between the actual data and the simulation. The simulation results are somewhat low. However, information is not available to determine whether the plant chemistry or the ECP model is the source of the inaccuracy. It is important to note that in the simulation boiling cannot occur in the bypass region, while in the actual reactor a small amount of boiling will occur resulting in decreased hydrogen. The core boiling curve is put on the figure to show the effect of boiling on ECP. The hydrogen added in the feedwater goes into the vapor phase allowing the oxygen produced by radiolysis to lead to a high ECP.

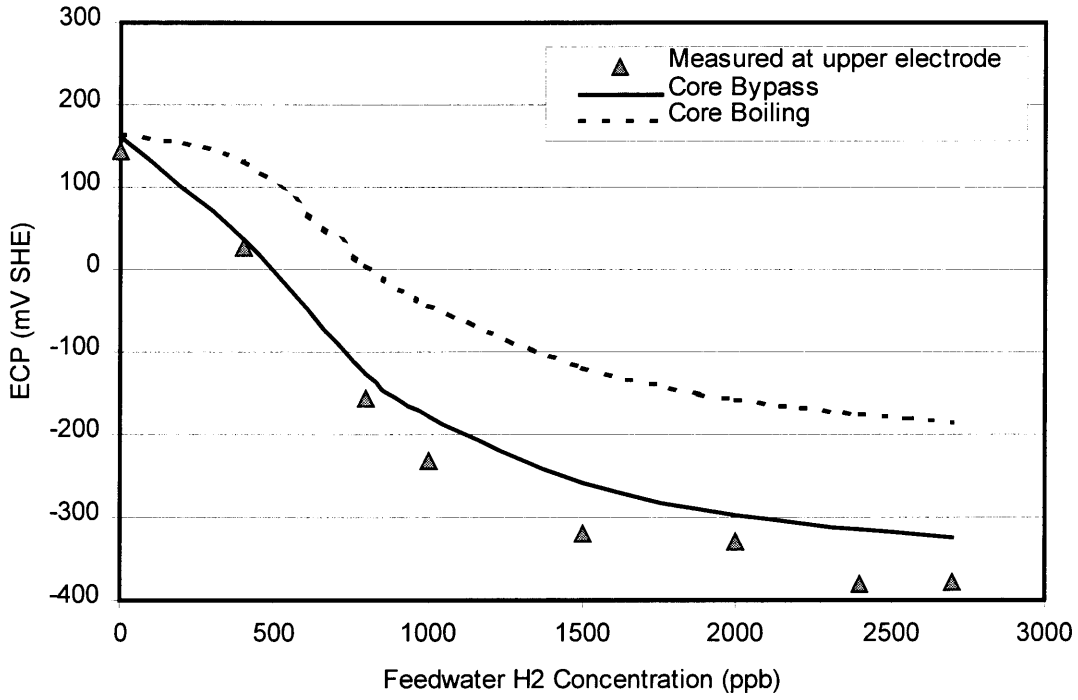

Figure 4.11. Reactor data (symbols) for lower core bypass region and RadiCAL model ECP output using BWR3 input file [4.14].

Figure 4.11 shows reactor data for the core bypass region near the bottom of the active fuel. Plotted with this data are curves from RadiCAL using the BWR3 standard input file. The data used is from the first spatial step in the core bypass and core boiling regions. Agreement between the actual data and the simulation is good. As mentioned above, the simulation data for the core bypass region should be slightly lower than the measured data. Therefore, the combination of the plant chemistry model and the ECP model yields a slightly higher value than measured.

4.4. Crack Growth Model

The crack growth model has been verified using data from the literature. Several sources as well as several different types of experiments have been used [4.15-4.17]. This literature search for crack advance rate data serves two functions. This data both allows the refinement of uncertain parameters and verifies that the model accurately fits both the shape and magnitude of the effect of various parameters on cracking. The problem with using this data to refine uncertain parameters is that in the literature parameters that should be certain are not always given. That is, parameters such as, the distance from the crack tip to the point at which the strain acts, r, are not known and rely on data to find a reasonable value. However, in the literature, the metal yield strength, and crack length are not usually reported. There are more unknown values than equations to solve them. Assumptions must be made over a large number of data sets so that the assumptions can be tested even as the parameters are being determined.

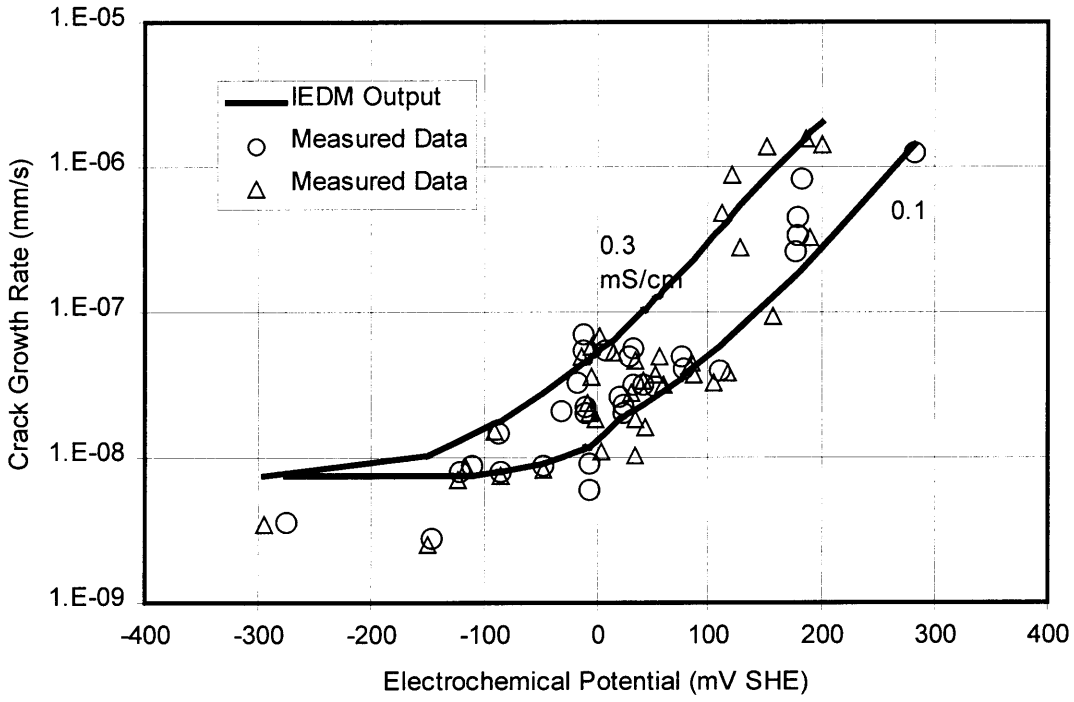

Figure 4.12. Crack growth rate versus ECP for sensitized SS 304 with conductivity = 0.1-0.3 μS/cm and K=88 Kg/mm$^{3/2}$ from Andresen, circles [4.15], trianlges [4.16], with crack growth model predictions.

In theses five figures, the crack growth model is verified independently of the other models. Most of the input parameters used for these five plots are the same. The constants are fixed: $\beta = 5.5$, plastic zone size constant, $\lambda = 1/3\pi$. Since all these plots are for stainless steel 304 and 316 the metal parameters are constant: atomic mass, M = 56 g/mole, density, $\rho = 8000$ kg/m^3, oxidation state, z = 2, Young's modulus, E = 22000 kg/mm^2, yield strength, σ_y –20 kg/mm^2, strain hardening exponent, n= 0.33, passive film rupture strain, $\varepsilon_f = 0.007$. The stress intensity factor, K, was assumed by the authors who published this data to be 88.6 kg/mm$^{3/2}$ (25ksi-in$^{1/2}$). The time constant for current decay, i_o, is 0.1 s and the oxidation current density on bare stainless steel is 10000A/m^2.

Two values were determined by finding the best fit to the data in these five sets and several others that are not published here [4.15-4.17]. The stress intensity factor rate of change, K', is 0.0001 kg/mm$^{3/2}$s and the distance to the growing crack tip is 0.04 mm. Only one parameter is left: the current decay curve slope, m.

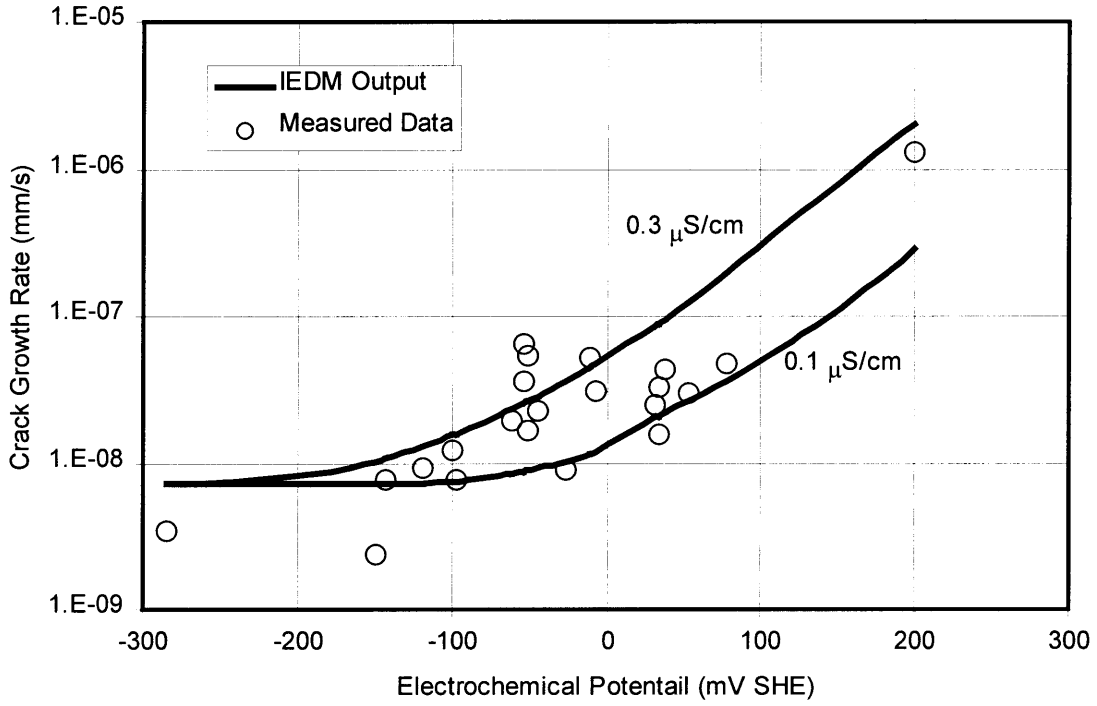

Figure 4.13. Crack growth rate versus ECP for sensitized SS 304 with conductivity = 0.1-0.3 μS/cm and K=88 Kg/mm$^{3/2}$ from Pathania [4.17], with crack growth model predictions.

The current decay curve slope, m, depends on the electrochemical parameters of the coolant solution. Its value is determined by the current decay curve correlation. For Figure 4.12, Figure 4.13, and Figure 4.14 the electrochemical potential (ECP) varies. The data used in the experiments comes from both laboratory and reactor data. The conductivity of the bulk solution at 25°C is given as 0.1 to 0.3 μS/cm. This is the range of conductivity found in an operating BWR. Each of these three plots has two lines from

the crack growth model output for these two extremes of conductivity. The electrochemical potentiokinetic reactivation (EPR) is assumed by the authors who published this data to be 15 C/cm^2 [4.15, 4.16]. This is a standard assumption for thermally sensitized stainless steel, and the current decay curve correlation was created with this assumption in mind.

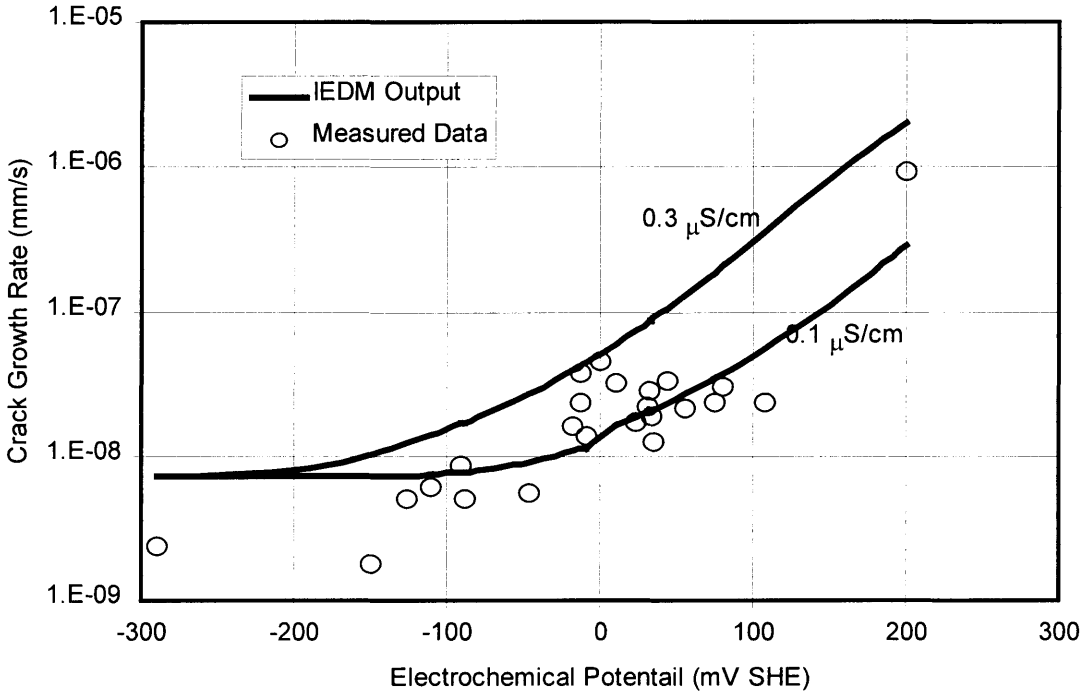

Figure 4.14. Crack growth rate versus ECP for sensitized SS 304 with conductivity = 0.1-0.3 μS/cm and K=88 Kg/mm$^{3/2}$ from Yeh [4.18], with crack growth model predictions.

The scatter in the data on these plots is likely due to the parameters that are not well characterized. As just mentioned, the EPR is not well characterized. The samples in these plots come are furnaced sensitized and simply assumed to have an EPR near 15. Another assumption is that the stress intensity factor equals 88.6 kg/mm3/2. This is an average value because the Stress intensity factor increases as the crack grows.

Additionally, the stress intensity factor is not well characterized for the portion of these experiments that were conducted in reactor.

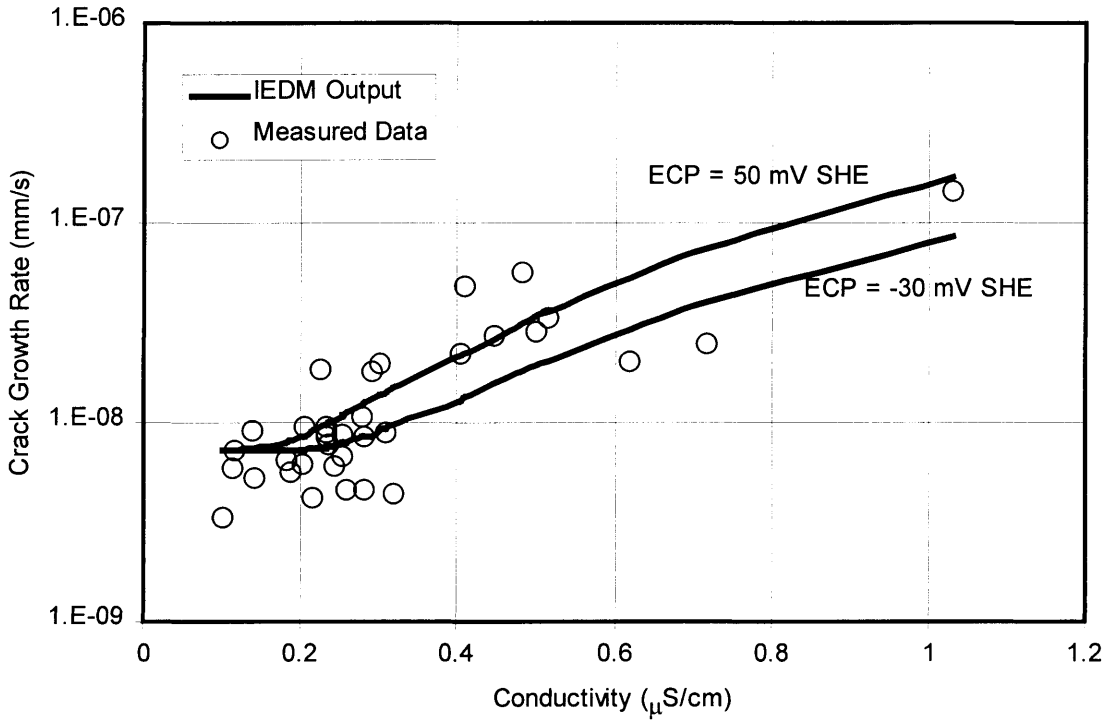

Figure 4.15. Crack growth rate versus solution conductivity for solution annealed SS 316L with potential between -30 and 50 mV SHE and K=88 Kg/mm$^{3/2}$ from Andresen [4.19], with crack growth model predictions.

For the data where the conductivity is varied over the range from 0.1 to 1 (Figure 4.15 and Figure 4.16), the conductivity is not well characterized. The dissolved oxygen content is given with the data as 200 ppb. While the dissolved oxygen is not perfectly constant it is probably maintained within 25% of this value. For the ECP model employed by the plant chemistry portion of IEDM, 200 ppb O_2 leads to an ECP of 15 mV SHE. A reasonable assumption is that the ECP is between -30 and 50 mV SHE for the water in these experiments. The two lines on Figure 4.15 and Figure 4.16 represent these

endpoints.

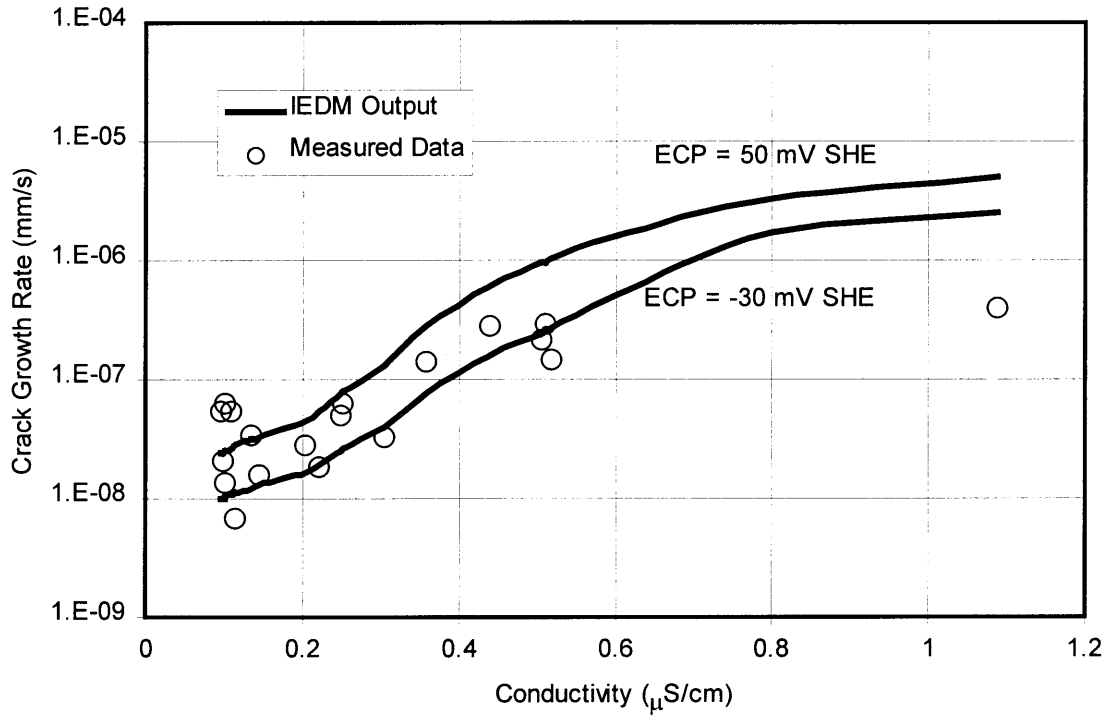

Figure 4.16. Crack growth rate versus solution conductivity for sensitized SS 304 with potential between -30 and 50 mV SHE and K=88 Kg/mm$^{3/2}$ from Andresen [4.19], with crack growth model predictions.

Data for pre-irradiated 304 stainless steel can indicate the validity of the crack growth model in combination with the radiation induced segregation model and the correlation for the equivalent EPR for RIS. Figure 4.17 shows data for samples irradiated to between 1 and 5 dpa.

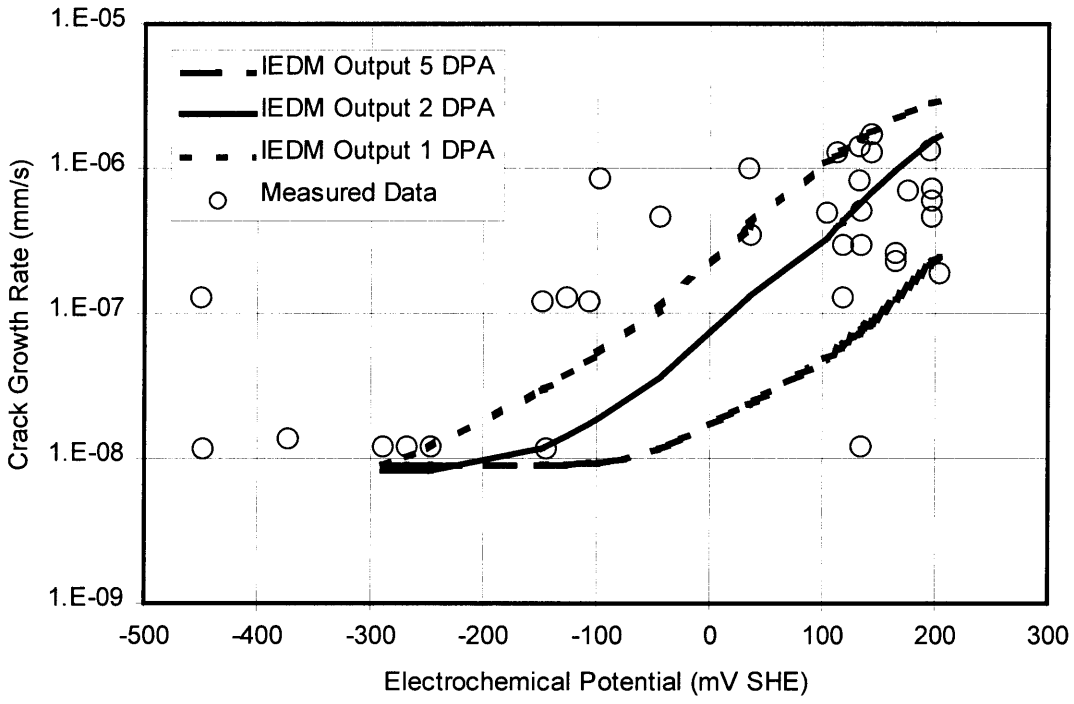

Figure 4.17. Crack growth rate versus ECP for pre-irradiated SS 304 from Andresen [4.16], with crack growth model predictions.

Data has been obtained from the Electric Power Research Instititute (EPRI) in order to access the validity of the entire model. However, inadequate information was provided to test the plant chemistry model with this data. The only plant/operating information given was the reactor, the location of the cracking, the temperature, the ECP, and the conductivity. Therefore, it is most logical to analyze the remainder of the model. Because the total fluence of at the location where the cracks are growing is given, the effects provided by the RIS model and the radiation hardening model can be verified. The name of each reactor is withheld because the data set is EPRI proprietary material. The following table gives the data as received.

Table 4.1. Data for shroud cracking.

Reac-tor	Position	Shroud Thicknes (mm)	Initial Crack Length (mm)	R/t	Temp (°C)	Fluence (N/cm2)	Compari ng Extention (mm)	ECP (mV-SHE)	Cond. (μS/cm	Duration (months)
A	H4 weld	38	10.2	60	288	2.3E+20	1.52	-323	0.12	18
A	H4 weld	38	12.2	60	288	2.3E+20	-2.29	-323	0.12	18
A	H4 weld	38	19.3	60	288	2.3E+20	-1.52	-323	0.12	18
A	H4 weld	38	15.7	60	288	2.3E+20	2.03	-323	0.12	18
A	H4 weld	38	17.5	60	288	2.3E+20	0.25	-323	0.12	18
A	H4 weld	38	16.5	60	288	2.3E+20	0.00	-323	0.12	18
A	H4 weld	38	17.5	60	288	2.3E+20	-2.29	-323	0.12	18
B	H2 weld	51	2.0	52	288	8.0E+18	0.51	200	0.11	16
B	H2 weld	51	17.8	52	288	8.0E+18	0.51	200	0.11	16
B	H3 weld	51	8.6	52	288	1.6E+20	1.02	200	0.11	16
B	H3 weld	51	11.4	52	288	1.6E+20	4.32	200	0.11	16
B	H3 weld	51	17.3	52	288	1.6E+20	7.62	200	0.11	16
B	H3 weld	51	0.3	52	288	1.6E+20	3.30	200	0.11	16
B	H5 weld	51	18.8	52	288	8.0E+16	1.52	200	0.11	16
B	H5 weld	51	21.8	52	288	8.0E+16	1.27	200	0.11	16
B	H5 weld	51	2.0	52	288	8.0E+16	0.51	200	0.11	16
B	H5 weld	51	16.3	52	288	8.0E+16	1.02	200	0.11	16
B	H5 weld	51	0.3	52	288	8.0E+16	2.29	200	0.11	16
B	H5 weld	51	3.0	52	288	8.0E+16	0.00	200	0.11	16
C	H3 weld	31	12.24	49	288	2.5E+20	-1.91	105	0.106	11
C	H3 weld	31	18.34	49	288	8.6E+20	-0.10	105	0.106	11
C	H4 w.(area 1)	31	8.84	49	288	8.6E+20	0.51	150	0.106	11
C	H4 w.(area 1)	31	9.55	49	288	8.6E+20	-0.20	150	0.106	11
C	H4 w.(area 2)	31	9.42	49	288	8.6E+20	4.50	150	0.106	11
C	H4 w.(area 2)	31	16.05	49	288	8.6E+20	-0.41	150	0.106	11
C	H4 w.(area 2)	31	12.14	49	288	8.6E+20	2.31	150	0.106	11

This data being comprised of growing cracks in actual reactors during service the measurement of crack growth rates (comparing extension in table) is difficult. Negative values have been measured for reactor A and C. While it might seem that these values

could be changed to zero noting the fact that the crack can not get shorter, it is more accurate to use an average value with all measurements. Therefore, the comparing extensions are averaged and divided by the total crack length to determine the growth rate at each weld. The following table gives the parameters determined by the model which differ from the base case as well as the measured and simulated crack growth rates.

Table 4.2. Data for shroud cracking.

Reac-tor	Position	Conductivity (μS/cm)	ECP (mV-SHE)	EPR (C/cm2)	m, current decay slope	Yield Stress (kg/mm2)	Strain hardening exponent	IEDM Crack Growth Rate (mm/yr)	Average Measured Crack Growth Rates (mm/yr)
A	H4 weld	0.12	-323	22	0.94	42	0.14	low	-0.22
B	H2 weld	0.11	200	0	0.88	30	0.29	0.32	0.38
B	H3 weld	0.11	200	20	0.57	41	0.15	23	3.5
B	H5 weld	0.11	200	0	0.88	23	0.33	0.32	0.83
C	H4 weld	0.11	150	30+	0.56	52	0.09	30	1.5

This data shows excellent results for the materials that are not predicted to be sensitized. For the sensitized materials the crack growth predictions are high. This is likely to due overprediction of radiation induced segregation effects.

4.5. IASCC Experiments

Recently experiments were conducted at MIT to characterize irradiation assisted stress corrosion cracking (IASCC) in austenitic stainless steels. These experiments are ideal for verifying the IEDM as a complete entity. Slow strain rate (SSR) tests at approximately 4×10^{-7} s^{-1}, were performed on several samples of types 304 and 316L stainless steel in an autoclave situated in the MIT Research Reactor core [4.10]. The

autoclave held 288°C water flowing at 1.3 m/s [4.10]. The water had an electrochemical potential (ECP) for stainless steel of between 0 and 100 mV versus the standard hydrogen electrode and was chemically similar to the coolant in an actual BWR. The neutron and gamma fields at the sample were 5 x 10^{13} n/m^2 and 1 x 10^5 R/s, respectively. The metal samples included solution annealed and furnace sensitized specimens, as well as samples that had been preirradiated up to approximately 0.8 dpa following solution annealing.

Because of the relatively high strain rate only a few of the samples experienced measurable stress corrosion cracking. That is, while many of the samples exhibited enhanced cracking due to factors such as chromium segregation, hardening, and radiolysis, there were only four samples for which crack growth rates could be determined for stress corrosion cracking. These four samples are all stainless steel 304. Two of the samples were irradiated to 0.8 dpa following solution annealing. The other two samples were furnace sensitized with one of them being 30% cold worked prior to sensitization to simulate radiation hardening effects [4.10]. The parameters associated with these four experiments are show in Table 4.3.

Table 4.3. IASCC output for which crack growth rate could be determined from SEM analysis [4.10].

Specimen Number	Heat Treatment	Fluence (x10^{25}n/m^2)	Yield Stress (Mpa)	Hardening Exponent (n)	Tested	Average crack growth rate (mm/s)
2012	SA+CW+Sen	0	632	0.21	out of core	3.07E-06
2003	SA+Sen	0	182	0.26	4.2 MW	3.96E-06
81	SA	0.8	570	0.12	4 MW	5.57E-07
82	SA	0.8	536	0.13	4 MW	6.62E-07

The first step in verifying the model is to create an input file for the plant chemistry model. The graphical user interface does not aid in this task because it is designed for BWR loops. For this experimental loop, an input file was created by hand (text editor). A schematic of the IASCC loop is shown is Figure 4.18.

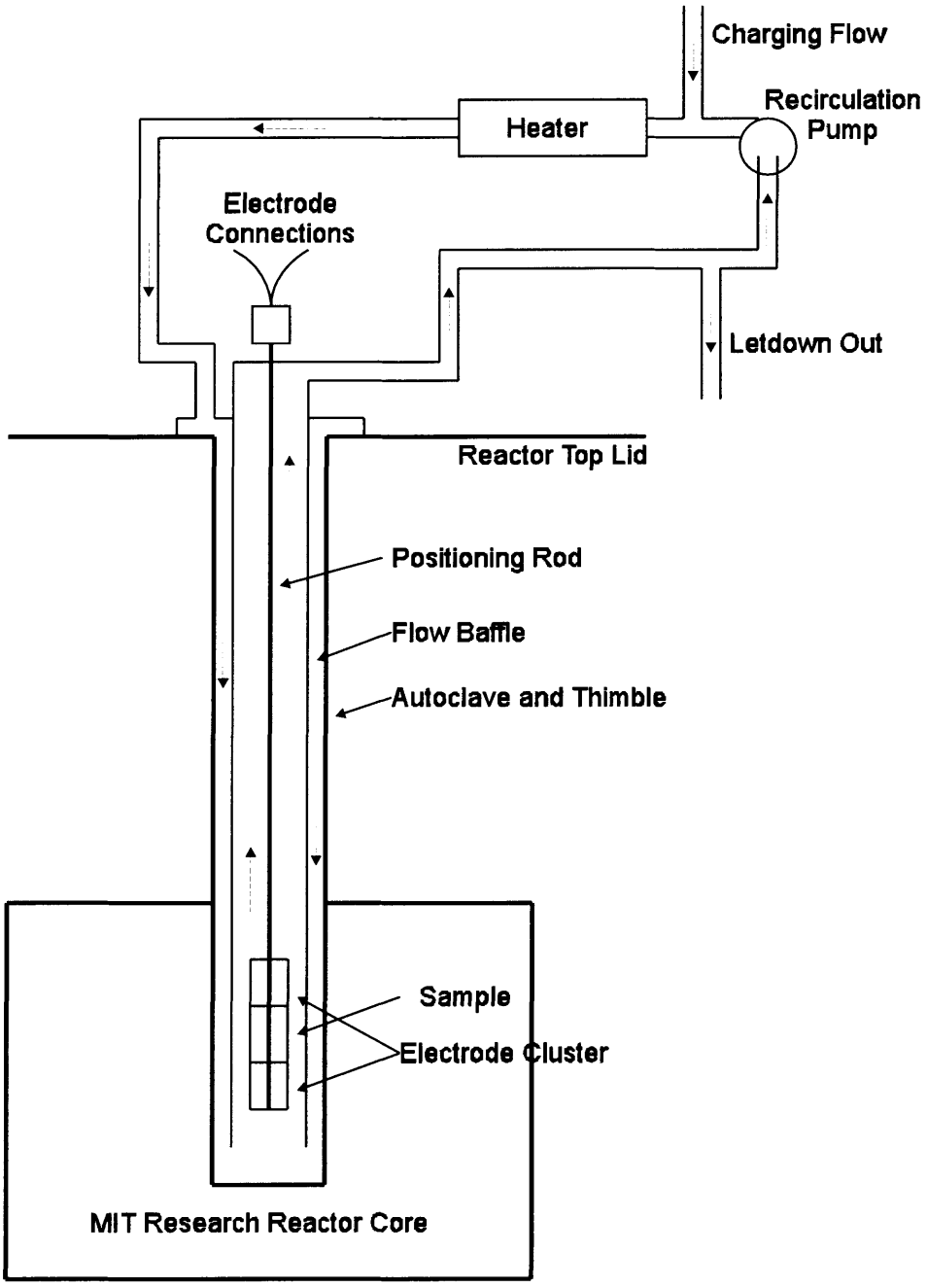

Figure 4.18. Schematic of IASCC testing rig (not to scale) [4.10].

The flow chart in Figure 4.19 is a graphical representation of the radical input file. All of the data in the input file except for the chemistry and radiolysis reaction sets is contained in the flow chart. The reaction sets were the same ones used in the BWR model. The reaction sets and G-values were those deemed appropriate for BWR plant chemistry at the MIT radiolysis workshop in August 1992 [REF].

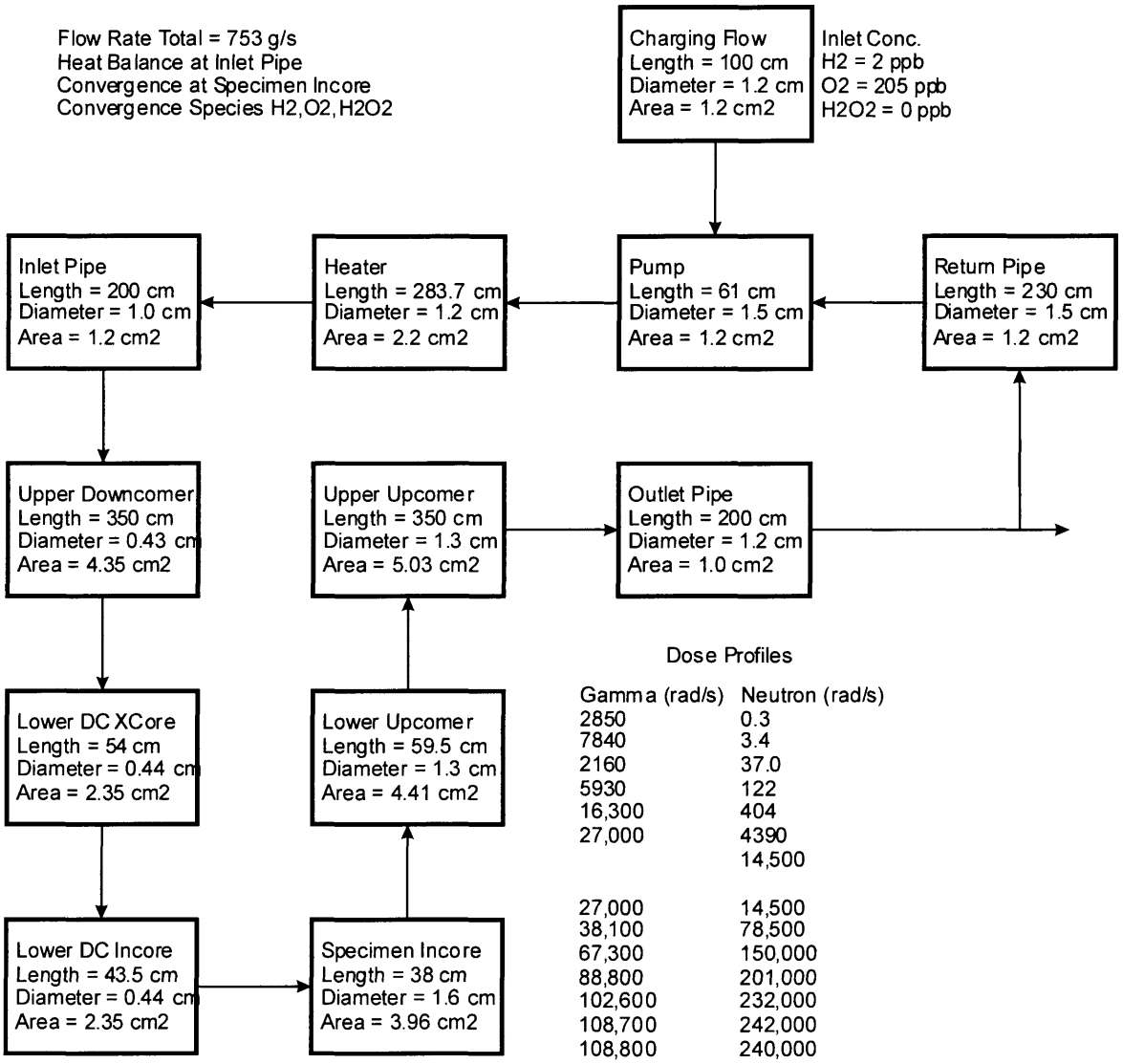

Figure 4.19. Flow diagram of RadiCAL input file for IASCC test loop. Parameters indicate equivalent dimensions of the flow channels and other input information [4.10].

For the IEDM, the important parameters from the plant chemistry model output are the ECP and concentrations of ionic species. The concentrations of ionic species are used to plot the change in conductivity as the water moves through irradiated portions of the coolant loop. The conductivity determined directly from these concentrations is lower than that found in the coolant loop because the plant chemistry model input file does not account for the concentration of impurities. Therefore, the conductivity of neutral coolant at 25°C must be inputted. The baseline conductivity desired for the IASCC experiments was 0.11 μS/cm based on EPRI guidelines for BWRs [4.10]. However, the conductivity of the water exiting the loop measured approximately 0.7 μS/cm. This conductivity did not result form deleterious ions. Their concentrations were determined by ion chromatography to be below the critical values cited in the same reference as the target conductivity [4.10]. It was deemed that the higher conductivities were caused by radiolysis of organic species leached into the test loop. For the IASCC project, it was assumed that while these species contributed to conductivity they did not contribute to cracking [4.10]. I find this assumption questionable as the reason that cracking increases with conductivity is not certain. Additionally, it is not known whether radiolytic organic species contribute to enhanced cracking. To continue using this data, a baseline conductivity of 0.3 μS/cm will be assumed. However, it should be noted that this is a principal source of error in this comparison.

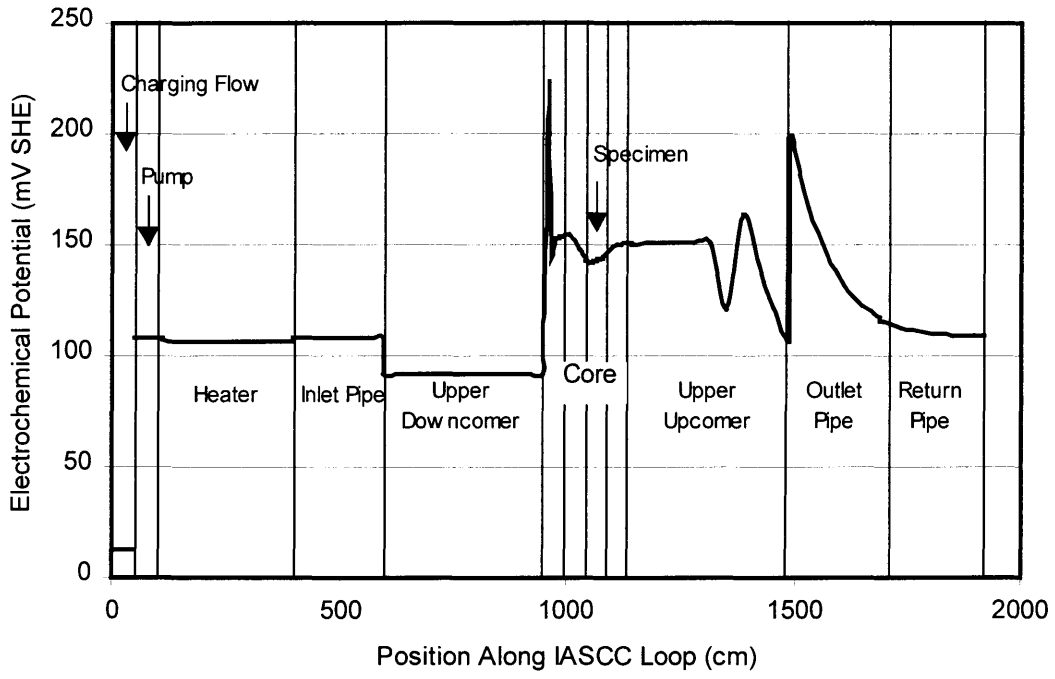

Figure 4.20. ECP throughout IASCC test loop.

The rapid (discontinuous) increases and decreases in ECP seen in Figure 4.20 are due to changes in flow velocity. Gradual changes are due to the production of O_2, H_2, and H_2O_2 by radiolysis as well as the recombination of these species. The output from the plant chemistry model gives the ECP at the specimen region as 140 mV SHE. The ECP was measured in the coolant loop with the reactor operating at 4 MWt at the specimen. For platinum electrodes the ECP was 150 mV SHE at the core midplane, 235 and 73 mV SHE (different times) 23 cm higher, and 290 mV SHE 46 cm above the core midplane. For silver electrodes the ECP was 86 mV SHE at the core midplane, 70 and 94 mV SHE (different times) 23 cm higher, and 69 mV SHE 46 cm above the core midplane. These values indicate a wide scatter for ECP that may be attributed to several issues. The potentials were measured during two separate experiments with different sample position resulting in slight geometric differences. Additionally a titanium spacer

was added in the second experiment. Regardless of ECP measurement difficulties, the value (140 mV SHE) predicted by the model agrees well with the range of measured data.

The third electrochemical parameter is the EPR. The two samples that were furnaced sensitized were heat treated at 650 C for 10 hours. This results in heavily sensitized material. Data from the literature indicates that this heat treatment results in an EPR of 30 C/cm^2 [4.20,4.21]. The current decay curve correlation implemented in this model is not valid for EPR values greater than 30 C/cm^2. The EPR value might be higher or lower than 30 because only the time and temperature are given to describe the sensitization state of the sample. This is not a problem because the effect of EPR on cracking plateaus around 30 C/cm2. Therefore, this value will be used for the furnace sensitized data as I continue through the model.

For the two preirradiated samples, chromium depletion at the grain boundary results from radiation induced segregation. In the write-up of the MIT IASCC project [4.10] only the total fluence of the irradiation is given. The irradiation rates are not given. This is significant as we have seen in the section describing the functionality of the RIS model. It is assumed that the sample was irradiated at 0.8 dpa per year for 1 year. Figure 4.21, shows the grain boundary profile for a sample irradiated to this degree as predicted by the radiation induced segregation model.

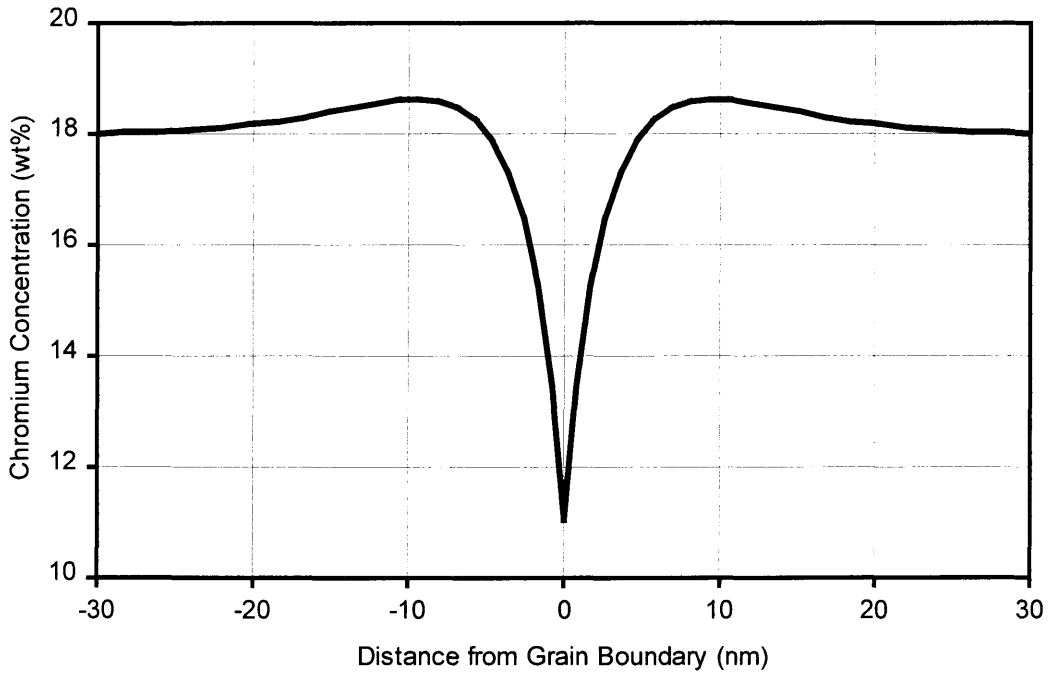

Figure 4.21. Grain Boundary chromium concentration profile for stainless steel 304 irradiated to 0.8 dpa at 288°C.

The equivalent EPR value for this data using the RIS to EPR correlation for stainless steel 304 is 8.

The experimental values for the yield strength and strain hardening exponent were used to determine the crack growth rate for the thermally sensitized materials. For the pre-irradiated samples this data comes form the hardening model. For 0.8 dpa and an initial yield strength of 182 MPa (from the unhardened sample) the final yield strength is 47 kg/mm2 (460 MPa) and the strain hardening exponent is 0.11. This compares favorably with the experimentally determined yield strengths of 536 and 570 MPa and the strain hardening exponent values of 0.12 and 0.13. The radiation hardening model output will be used in the crack growth model.

In order to find the stress intensity factor, it is assumed that the crack opens from the outside to inside of the sample. Additionally the crack is assumed circular around the entire circumference of the specimen. This crack morphology is shown in Figure 4.22 [4.22].

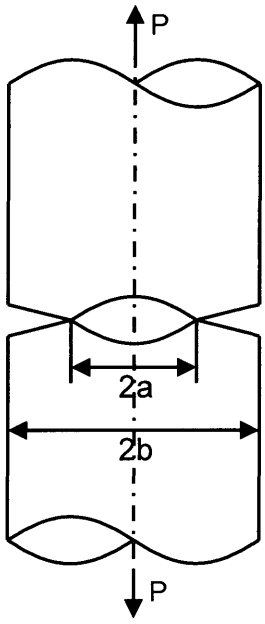

Figure 4.22. Assumed crack morphology in slow strain rate test specimen [4.22].

For this crack morphology the following equation gives the stress intensity factor, K_I, at the crack tip [4.22].

$$K_I = \sigma_{net}\sqrt{\pi \cdot a}\left\{\sqrt{1-\frac{a}{b}}\cdot\frac{1}{2}\left[1+\frac{1}{2}\frac{a}{b}+\frac{3}{8}\left(\frac{a}{b}\right)^2-0.363\left(\frac{a}{b}\right)^3+0.731\left(\frac{a}{b}\right)^4\right]\right\} \quad (4.1)$$

Where a and b are shown on the figure and σ_{net} equals the true stress ($P/\pi a^2$). Figure 4.23 shows how the stress intensity factor changes with crack depth.

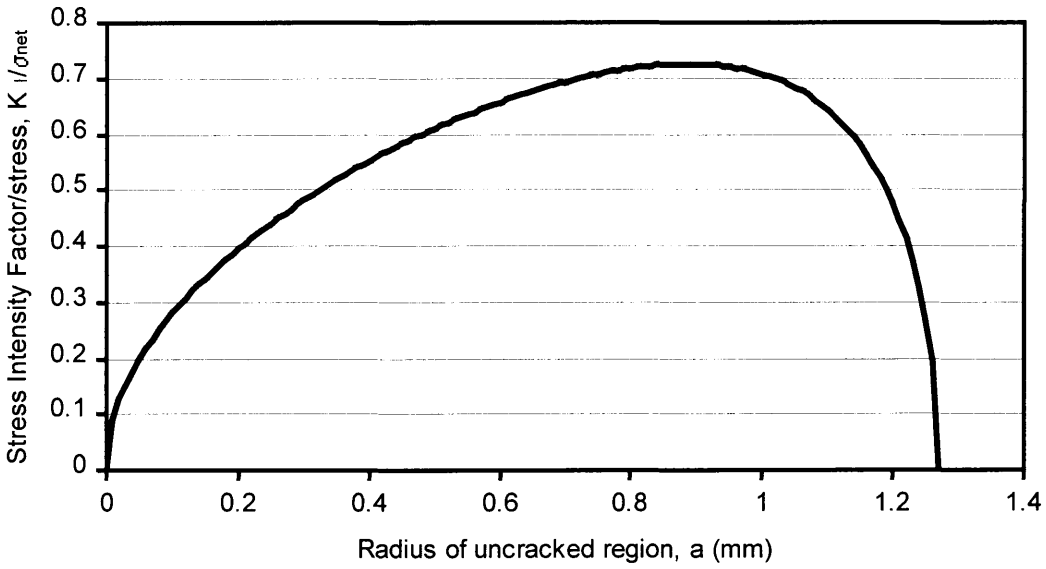

Figure 4.23. Plot of stress intensity factor over stress for all depths of cracking in a 2.54 mm cylinder.

From this plot it is clear that the stress intensity factor for each specimen will be between 0.6 and 0.7 $mm^{1/2}$ times the true stress acting on the specimen. The following table gives the yield stress, the ultimate stress (engineering), the strain over which plastic deformation is observed and the minimum and maximum stress intensity factors. The minimum stress intensity factors are found by multiplying 0.6 $mm^{1/2}$ by the yield stress. The maximum stress intensity factors are found by multiplying 0.73 $mm^{1/2}$ by the ultimate engineering stress.

Table 4.4. Determination of low and maximum stress intensity factors.

Specimen Number	Yield Stress (kg/mm^2)	Ultimate Stress (kg/mm^2)	Strain Range	Low K_I ($kg/mm^{3/2}$)	Maximum K_I ($kg/mm^{3/2}$)	K-rate, K' ($kg/mm^{3/2}s$)
2012	64	90	0.01-0.035	38	65	0.00015
2003	19	35	0.01-0.08	11	25	0.00004
81	47	85	0.02-0.13	28	62	0.00007
82	47	80	0.02-0.13	28	658	0.00006

The last column in this table gives an approximate value for the stress intensity factor rate of change. This value is determined by subtracting the low value from the maximum value for K and dividing by the total time for the experiment. The stress intensity factor could be higher if the actual change in K equals K max. However, the method used here gives the most reasonable approximation of K'. These results for K, are reasonable and agree will with the value chosen for the base case which best fits the crack growth rate data found in the literature. Table 4.5 summarizes the inputs and final outputs of the crack growth model and current decay curve correlation used to find the final output for these four specimens.

Table 4.5. Crack growth model inputs and outputs for IASCC experimental specimens.

Specimen Number	Conductvity (μs/cm)	ECP (mV SHE)	EPR (C/cm^2)	m, current decay slope	Yield strength (kg/mm2)	Hardening exponent, n
2012	0.3	140	30	0.45	64.5	0.21
2003	0.3	140	30	0.45	18.6	0.26
81	0.3	140	8	0.66	47	0.11
82	0.3	140	8	0.66	47	0.11

Specimen Number	K ($kg/mm^{3/2}$)	K-rate, K' ($kg/mm^{3/2}s$)	ε'_{ct}, crack tip strain	Calculated CGR (mm/s)	Measured CGR (mm/s)
2012	65	0.00015	4.5E-6	8.6E-6	3.1E-6
2003	25	0.000044	7.2E-7	3.8E-6	4.0E-6
81	62	0.000073	7.6E-8	1.2E-7	5.6E-7
82	58	0.000058	6.7E-8	1.1E-7	6.6E-7

Agreement between the output of the entire IEDM and the experimental parameters is excellent. The samples sensitized by radiation induced segregation were low by a factor of approximately 5. This is very low considering the many orders of

magnitude over which cracking occurs and the uncertainty in the conductivity value. The two thermally sensitized values are highly accurate.

4.6. References

[4.1] Boerigter, S. T., "An Investigation of Neutron-Irradiation Induced Segregation in Austenitic Stainless Steels," ScD theses, Nuclear Engineering Department, Massachusetts, Institute of Technology, 1992.

[4.2] Norris D.I.R., Baker C., Taylor C., and Titchmarsh, J.M. "Compositional Profiles at Grain Boundaries in SGHWR Irradiated 20 Cr/25Ni/Nb Steel," CEGB Research Report, RD/B/60144/R88 (1988).

[4.3] Norris D.I.R., Baker C., and Titchmarsh, J.M. "A Study of Radiation Induced Segregation in 20Cr/25Ni/Nb Steel by Compositional Profile Measurements at Grain Boundaries," Materials for Nuclear Reactor Core Applications, Vol. 1 (1987).

[4.4] Elen, J. D., Fenici P., "Fast-Neutron Irradiation Hardening Of Austenitic Stainless-Steel At 250°C," Journal of Nuclear Materials, V. 191, (Sep. '92) pp. 766-770.

[4.5] Chung, H. M., Ruther, W. E., Sanecki, J. E., Hins, A. G., and Kassner, T. F., "Stress Corrosion Cracking Susceptibility of Irradiated Type 304 Stainless Steels," Effects of Radiation on Materials: 16th International Symposium, ASTM STP 1175, (Jun. '92) pp. 851-869.

[4.6] Garner, F. A., Hamilton, M. L., Greenwood, L. R., Stubbins, J. F., and Oliver, B. M., "Isotopic Tailoring with 59Ni to Study Helium Generation Rates and Their Effect on Tensile Properties of Neutron-Irradiated Fe-Cr-Ni Alloys," Effects of Radiation Materials: 16th International Symposium, ASTM STP 1175, (Jun. '92) pp. 921-939.

[4.7] Bruemmer, S. M. and Simonen, E. P., "Radiation Hardening and Radiation-Induced Chromium Depletion Effects on Intergranular Stress Corrosion Cracking in Austenitic Stainless Steels," Corrosion, V. 50 (Dec. '94) pp. 940-946.

[4.8] Josefsson, B., and Bergenlid, U., "Tensile, Low-Cycle Fatigue and Fracture-Toughness Behavior of Type-316L Steel Irradiated to 0.3 dpa," Journal of Nuclear Materials, V. 215 (Sep. '94) pp. 525-529.

[4.9] Samuel, K.G., Mannan, S.L., Radhakrichnan, V.M., The Influence of Temperature and Prior Cold Work on the Strain Hardening Parameters of a Type 316 LN Stainless Steel., International Journal of Pressure Vessels and Piping. V. 52, N. 2 (1992) pp.151-157.

[4.10] Hilton, Bruce A., "Irradiation Assisted Stress Corrosion Cracking Susceptibility of Low Fluence Stainless Steels Evaluated by In-Flux Slow Strain Rate Tests." PhD thesis, Nuclear Engineering Department, Massachusetts, Institute of Technology, 1992.

[4.11] Chun, J. H., "Modeling of BWR Water Chemistry." SM thesis, Nuclear Engineering Department, Massachusetts, Institute of Technology, 1990.

[4.12] Grover, D. J., "Modeling Water Chemistry and Electrochemical Corrosion Potentials in Boiling Water Reactors." SM thesis, Nuclear Engineering Department, Massachusetts, Institute of Technology, 1996.

[4.13] Simonson, S.A., "Modeling of Radiation Effects of Nuclear Waste Package Materials," Ph.D. Thesis, Department of Nuclear Engineering, Massachusetts Institute of Technology, Cambridge, MA (September, 1988)

[4.14] Lin, C. C., Kim, Y. J., Niedrach, L. W. Ramp, K. S., "Electrochemical Corrosion Potential Models for Boiling-Water Reactor Applications", Corrosion Vol. 52, No. 8 (1996) pp. 618-625.

[4.15] Andresen, P. L., Fracture Mechanics Data and Modeling of Environmental Cracking of Nickel-Base Alloys in High-Temperature Water. Corrosion V. 47 (Dec. '91) pp. 917-38.

[4.16] Andresen, P. L., Ford, F. P., Modeling & Prediction of Irradiation Assisted Stress Corrosion Cracking. 7th International Symposium on Environmental Degradation of Materials in Nuclear Power Plant-Water Reactors V. 2 (Aug. '95) pp. 893-908.

[4.17] Pathania, Raj, On-Line Prediction of Crack Growth in BWR Piping. EPRI Journal V. 16 (Apr./May '91) pp. 43-45.

[4.18] Yeh, T.-K., Macdonald, D. D., Modeling the Development of Damage in BWR Primary Coolant Circuits. 7th International Symposium on Environmental Degradation of Materials in Nuclear Power Plant-Water Reactors V. 2 (Aug. '95) pp. 909-920.

[4.19] Andresen, P. L., "'Current' Issues in SCC: Where Does Current Flow in Cracks?"

[4.20] Bruemmer, S.M., Quantitative modeling of sensitization development in austenitic stainless steel, Corrosion Vol. 46 No. 7 (1990) pp. 556-562.

[4.21] Bruemmer, S. M.; Charlot, L. A.; Arey, B. W., Sensitization Development In Austenitic Stainless Steel: Correlation Between Stem-Eds And Epr Measurements, Corrosion Vol. 44 No. 6 (1988) pp. 328-333.

[4.22] Tada, H, Paris, P. C., Irwin, G. C., The Stress Analysis of Cracks Handbook, 2nd ed., Paris Products Inc., (1985).

5. Application and Discussion

5.1. Near Weld Cracking

In boiling water reactors, stress corrosion cracking is most significant near welds because welds provide two of the necessary factors for SCC. These factors are a sufficiently sensitized material and high tensile stresses. The material is sensitized near welds due to chromium carbide precipitation described in section 3.3. High tensile stress levels are often present near welds for several reasons. Residual stresses from welding, stresses due to different thermal expansion coefficients due to welding of unlike metals and stress (including fatigue) due to the flow of coolant through the welded pipes are among these reasons.

Specific areas where SCC in weld heat affected zones has occurred in current operating reactors include the control rod drive housings and stub tubes, the jet pump recirculation system, and the core spray piping system. To model these areas, assumptions must be made to define the materials near the welds. The material, which will be considered, is stainless steel 304, a common material in these components. The first assumption is that the electrochemical potentiokinetic reactivation is 15 coulombs per square centimeter. This value expresses the sensitivity of the metal due to grain boundary chromium depletion. Fifteen is the value that is commonly chosen for an average EPR of weld sensitized stainless steel. For the radiation hardening, it is assumed that the reactor has operated for 20 years at 75% utilization. In this time it is likely that

some radiation induced segregation will have occurred. However, the fluence levels at the components listed here are not likely to contribute significantly to the sensitization already caused by the welding process.

The radiation hardening is determined for each area mentioned above. For the control rod drive system, output data from the BWR type one reactor model is used. The flux is between the stub tubes and the core plate varies greatly with the value near the stub tubes being too low to cause significant irradiation hardening effects. For the jet pump recirculation system, output data for the BWR type three reactor must be used. For the components that are within the pressure vessel, (the jet pump riser, throat, and diffuser) the doses vary from 0.00001 dpa/year to 0.0005 dpa/year. The highest fluence at these components is therefore .0075 dpa. It is predicted that a small amount of radiation hardening will occur at this fluence. At the core spray piping system, using the BWR-3 model, the dose rates are significant. At the beginning of the upper plenum (just above the fuel), the flux is 0.008 dpa/year, this value drops to insignificant values on the way to the top. Some of the welded components are in the region of significant flux where the total fluence might be as high as 0.1 dpa.

Table 5.1. Assumptions for model output case

Variable	Base Case Value
λ, Plastic zone size constant	$1/(3\pi)$, 0.106
β, Analytical strain distribution constant	5.5
M, Metal atomic mass	56 g/mole
ρ, Metal density	8000 kg/m^3
z, Oxidation state of dissolution	2
ε_f, Passive film rupture strain	0.007
E, Young's modulus	22000 kg/mm^2

σ_y, Yield strength	Determined from hardening model
n, Strain hardening exponent	Determined from hardening model
K, Stress intensity factor	80 $Kgmm^{1/2}/mm^2$
K', Stress intensity factor rate of change	0.0001 $Kg/mm^{3/2}s$
r, Distance from growing crack tip	0.04 mm
C, Hydrogen embrittlement cleavage factor	0 mm (not significant under NWC)
t_o, Time constant for current decay	0.1 s
i_o, Bare surface oxidation current density	10000 A/m^2 (above -300 mV SHE)
m, Oxidation current decay curve slope	Determined from the following three inputs
EPR, sensitization	15 C/cm^2
ECP, corrosion potential	Determined from plant chemistry
Bulk conductivity at 25C	0.12 μS/cm base value PLUS contribution determined from plant chemistry model

The stress and strain parameters used are those that were assumed in the previous section where the model was verified with actual measurements. Therefore, the stress intensity factor, K, is 80 $Kgmm^{1/2}/mm^2$, the rate of change of K is 0.0001 $Kg/mm^{3/2}s$ and the distance from the growing crack tip, r, is 0.04 mm. The base case values that will be used for most of these results are summarized in Table 5.1.

In the stub tube region, crack growth rates for a reactor operating at full power and flow are predicted to be $1.7x10^{-7}$ mm/s (0.5cm/year). This means that significant cracking will occur once a crack is initiated in weld sensitized material in a reactor operating with normal water chemistry provided that the significant stresses assumed here are acting on the crack. To mitigate cracking either stresses must avoided or the water must be treated (hydrogen water chemistry) to reduce the electrochemical potential. For this data, negligible radiation hardening will have occurred therefore the yield strength is

20 kg/mm^2 and the strain hardening exponent is 0.33. Figure 5.1 shows the effect of power level and coolant flow rate on crack growth rates.

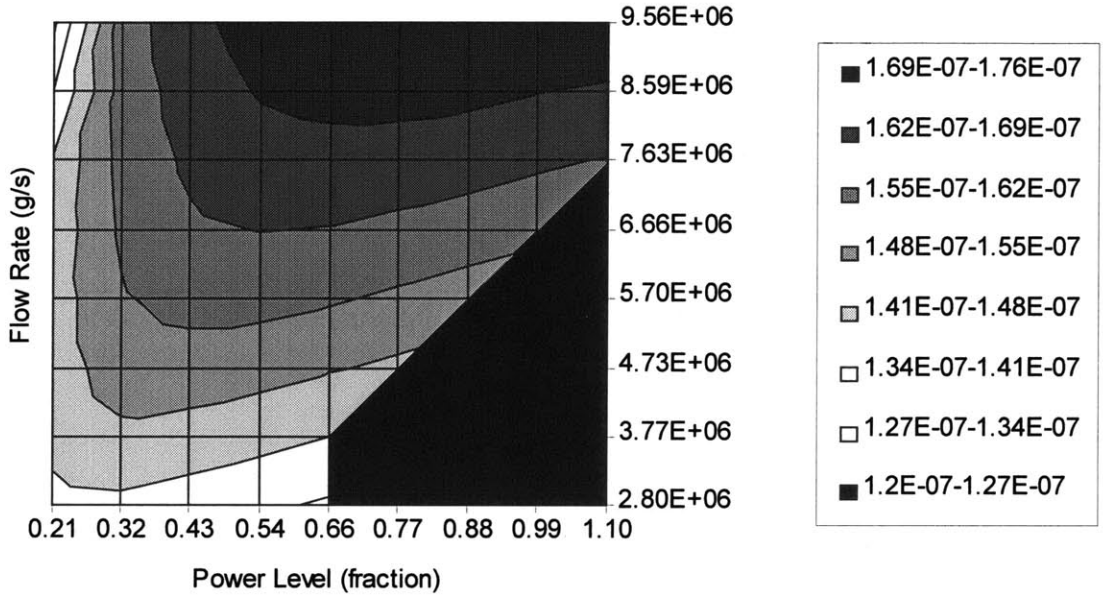

Figure 5.1. Crack growth rate (mm/s) as a function of power level and flow rate for BWR type 1 reactor stub tube region. Darker areas indicate faster cracking.

The black region on Figure 5.1 indicates an area where a reactor cannot operate because the flow is too low to cool the reactor. Figure 5.1 shows that cracking rate generally increases with power level and flow rate. The next zone where weld sensitized materials are significant is the jet pump components that are within the pressure vessel. These components receive significant dose and will have undergone irradiation hardening leading to yield strength of 29 kg/mm^2 and a strain hardening exponent of 0.3. At the top of the jet pump suction (the jet pump intake) the crack growth rate at full power and flow is 2×10^{-7} mm/s (0.6 cm/year). The following plot indicates the effect of power and flow at this point in the reactor.

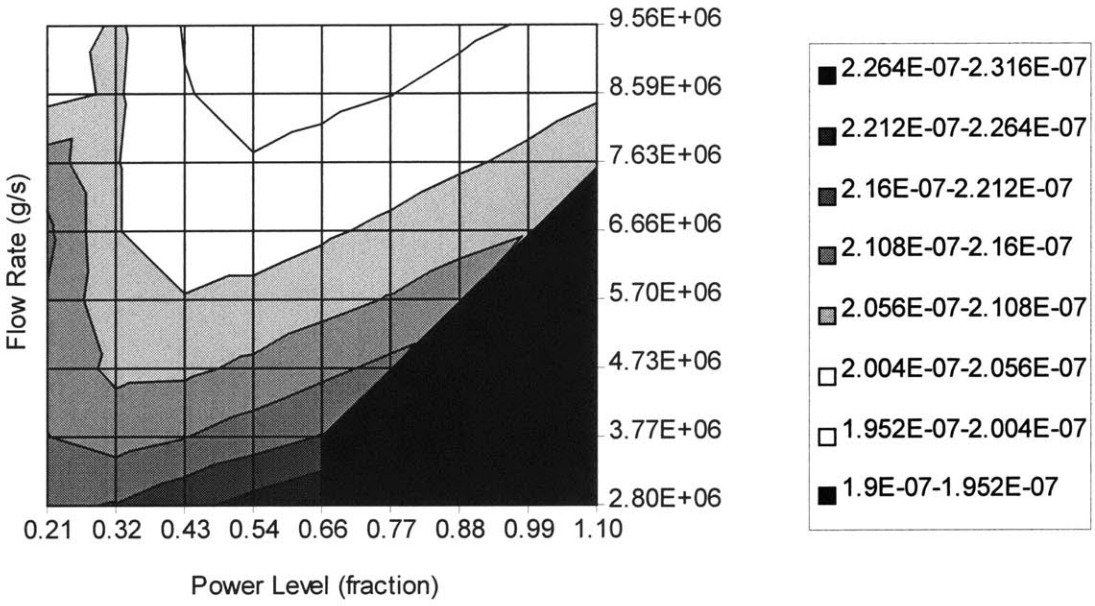

Figure 5.2. Crack growth rate (mm/s) as a function of power level and flow rate for BWR type 3 reactor at the top of the jet pump suction. Darker areas indicate faster cracking.

As Figure 5.2 shows, the crack growth rate decreases with increasing with increasing flow rate. After the coolant flow reenters the reactor from the recirulation pump, it goes up the jet pump riser. At the center of the riser the crack growth rate at full power and flow is 2.5×10^{-7} mm/s (0.8 cm/year). The following plot indicates the effect of power and flow in the jet pump riser.

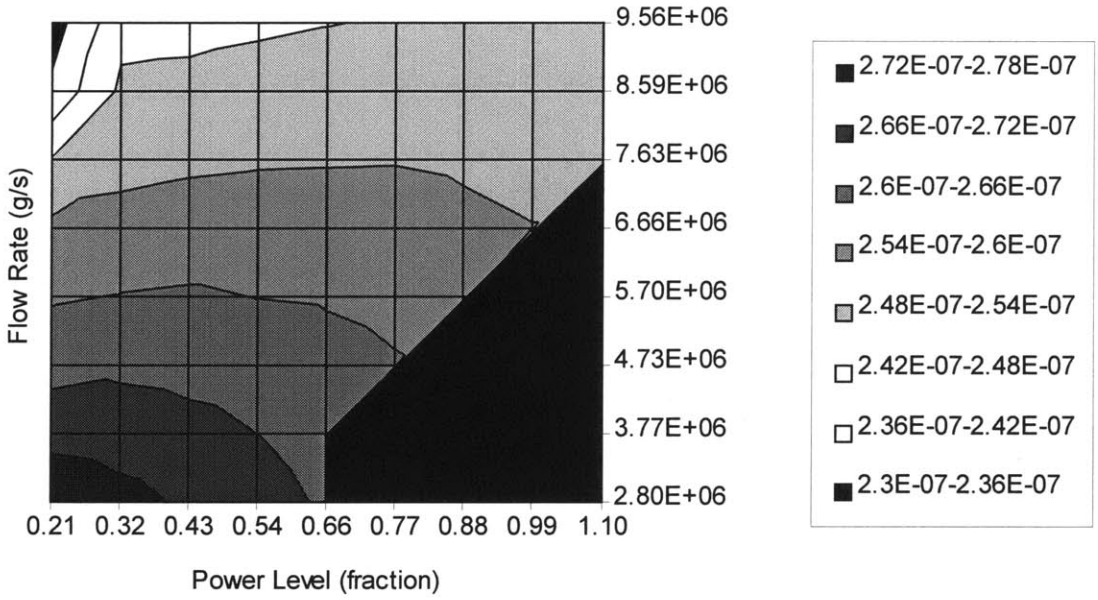

Figure 5.3. Crack growth rate (mm/s) as a function of power level and flow rate for BWR type 3 reactor jet pump riser. Darker areas indicate faster cracking.

Figure 5.3 indicates that the crack growth rate decreases with increasing with increasing flow rate. Following the jet pump riser, the coolant enters the jet pump throat and diffuser. These two components were separated in the input file when the model was adapted to account for changes in the flow area of a component. In the diffuser, the area is increasing to decrease the flowrate of the coolant. The coolant had been previously sped up to provide suction at the top of the jet pump. At the midpoint of the jet pump throat the crack growth rate at full power and flow is 2.3×10^{-7} mm/s (0.7 cm/year). At the midpoint of the jet pump diffuser the crack growth rate at full power and flow is 2.2×10^{-7} mm/s (0.7 cm/year). While these value are very close, the crack growth rate does decrease slightly as the flow rate decreases. The following plots indicate the effect of power and flow in the jet pump throat and diffuser.

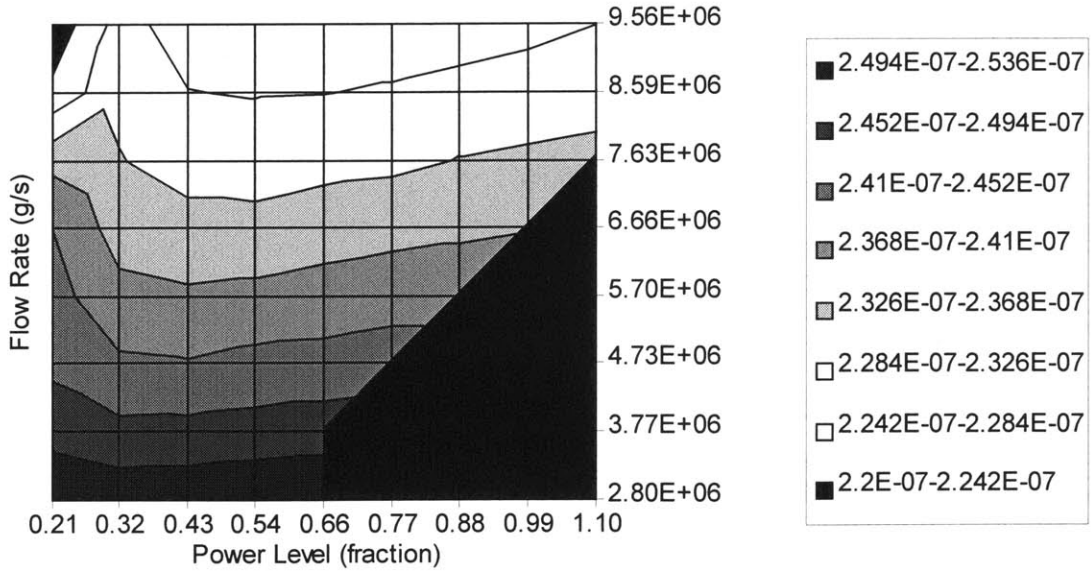

Figure 5.4. Crack growth rate (mm/s) as a function of power level and flow rate for BWR type 3 reactor jet pump throat. Darker areas indicate faster cracking.

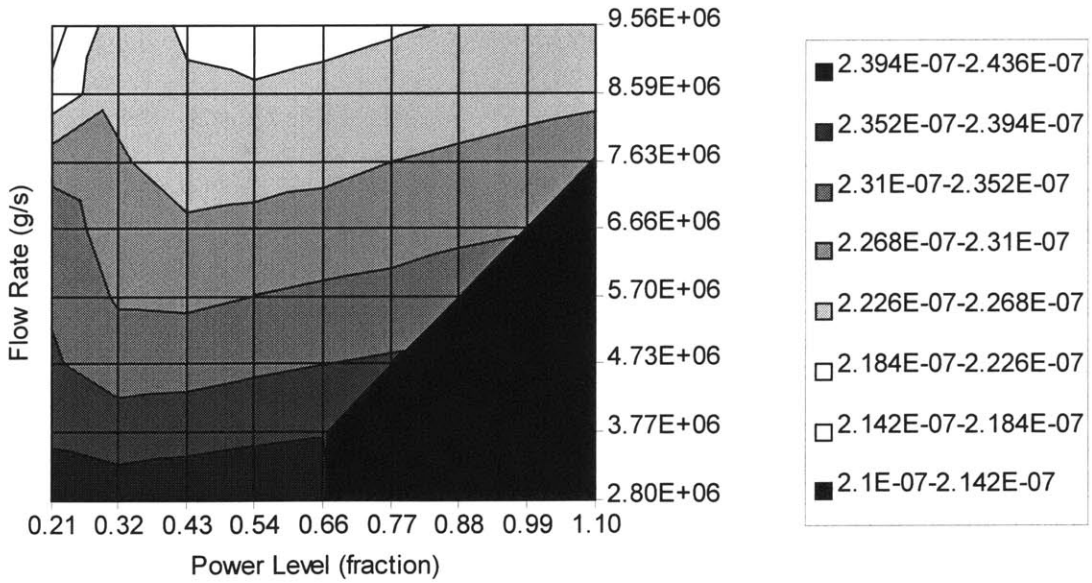

Figure 5.5. Crack growth rate (mm/s) as a function of power level and flow rate for BWR type 3 reactor jet pump diffuser. Darker areas indicate faster cracking.

Figure 5.4 and Figure 5.5 indicate that the cracking rate generally decreases with increasing flow rate. These plots are for the inside of the jet pump system. On the outside of the jet pumps the downcomer is divided into five radial sections for modeling purposes. This is done to allow different dose levels across the downcomer. In reality the coolant in these five zones is able to mix. At full power and flow the crack growth rate at the bottom of the inner layer of the downcomer is 1.6×10^{-7} mm/s (0.5 cm/year). For the outermost layer of the downcomer the crack growth rate at the bottom is 2.3×10^{-7} mm/s (0.7 cm/year). Figure 5.6 and Figure 5.7 show the crack growth rates at the bottom of the innermost and outermost regions of the downcomer.

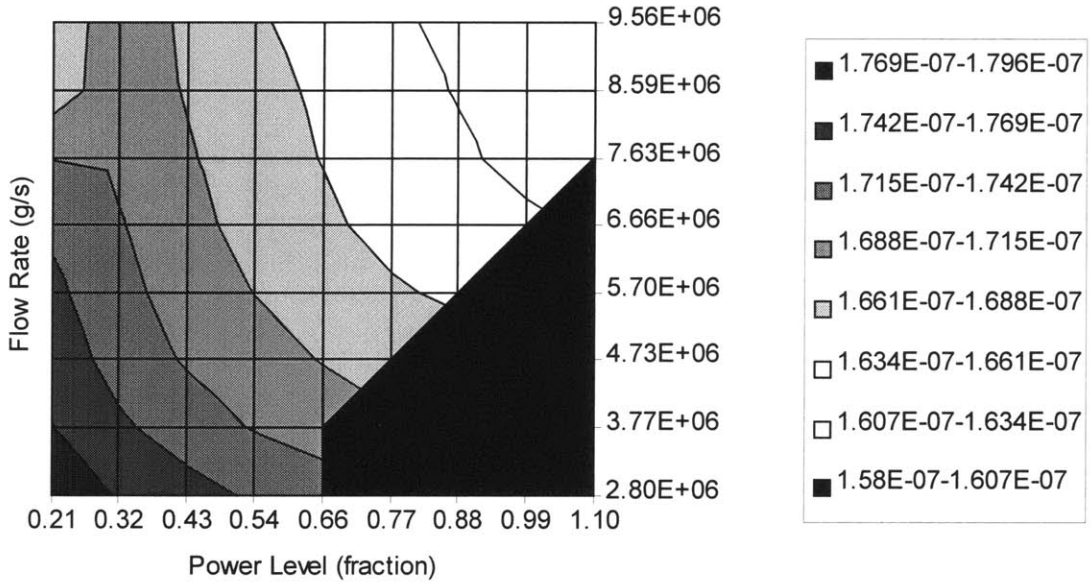

Figure 5.6. Crack growth rate (mm/s) as a function of power level and flow rate for BWR type 3 reactor at the bottom of the downcomer close to the core shroud. Darker areas indicate faster cracking.

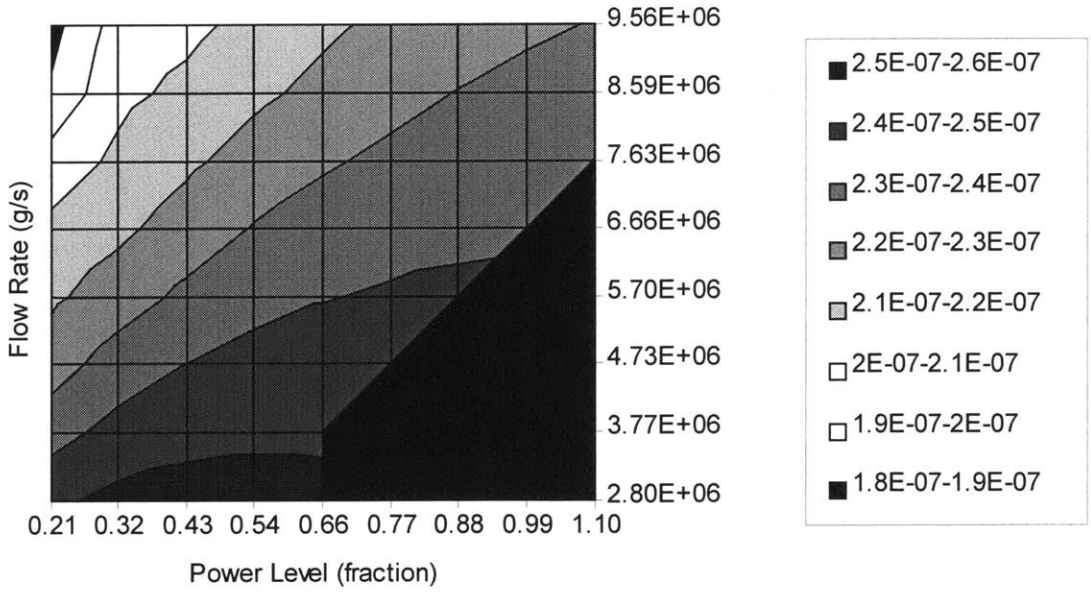

Figure 5.7. Crack growth rate (mm/s) as a function of power level and flow rate for BWR type 3 reactor at the bottom of the downcomer close to the pressure vessel. Darker areas indicate faster cracking.

Another zone where weld sensitized materials are significant is the core spray system. These components receive significant dose and will have undergone irradiation hardening. Following fifteen years of operation at the maximum flux rate in this region of 0.008 dpa/year, the yield strength is 37 kg/mm^2 and the strain hardening exponent is 0.18. At the top of the core (beginning of the upper plenum) the crack growth rate at full power and flow is 1.2×10^{-7} mm/s (0.4 cm/year). Figure 5.8 indicates the effect of power and flow at this point in the reactor.

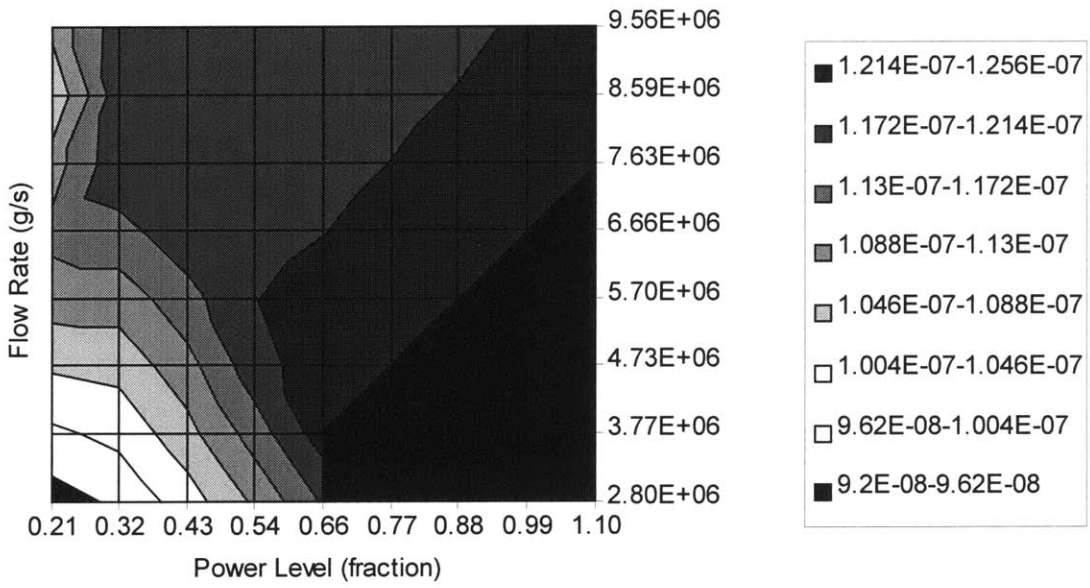

Figure 5.8. Crack growth rate (mm/s) as a function of power level and flow rate for BWR type 3 reactor at the start of the upper plenum (top of fuel). Darker areas indicate faster cracking.

These data not only provide a look at crack growth rates where sensitized materials and high stresses meet under normal water chemistry conditions, they also indicate the effects of transients such as start up and shutdown.

5.2. Effect of Hydrogen Water Chemistry

The results of the previous section indicate that significant cracking will occur under normal water chemistry conditions for sensitized materials under high tensile stresses. Therefore, in order to reduce the cracking rate on weld sensitized materials either the stresses must be reduced, or the coolant must be made less aggressive. The addition of hydrogen to the feedwater decreases the electrochemical potential of the water. The IEDM is ideally suited to directly determine the effect of hydrogen addition on cracking throughout the reactor. The effect of hydrogen on the key areas used in the

previous section will be studied for reactor operation at full power and flow. The same base case variables for stainless steel 304 and high stresses and strain rates is used. The following plot demonstrates the effect of feedwater hydrogen on cracking in the stub tube region of a BWR type 1 reactor.

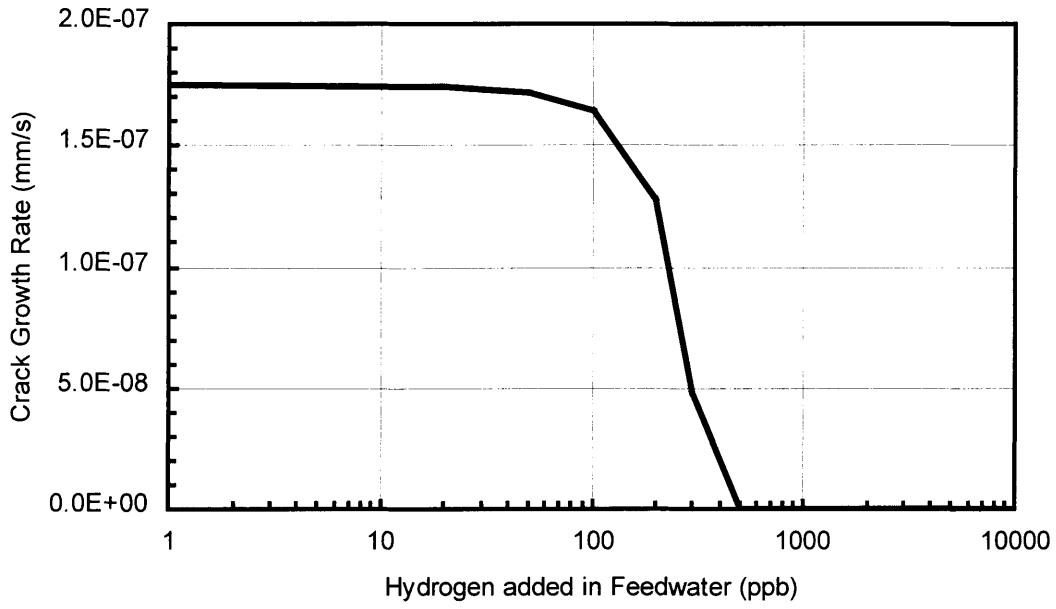

Figure 5.9. Crack growth rate (mm/s) as a function of feedwater hydrogen input for BWR type 1 reactor at center of the reactor stub region.

Figure 5.9 indicates that crack growth rate is below 10^{-9} mm/s when hydrogen addition to the feedwater exceeds 500 ppb. It is important to note that the crack growth rate is plotted linearly. Therefore, the crack growth rate does not go to zero but it is below10^{-9} (the minimum resolution on this plot). This correlates to a crack growth rate of 0.03 mm/year or a millimeter over the lifetime of the plant (no cracking). The next area of interest to weld sensitized is the jet pump system. Because this region is preceded closely by the entry of the feedwater to the system, the hydrogen addition is effective in reducing cracking. However, this is not evidenced in the following plot.

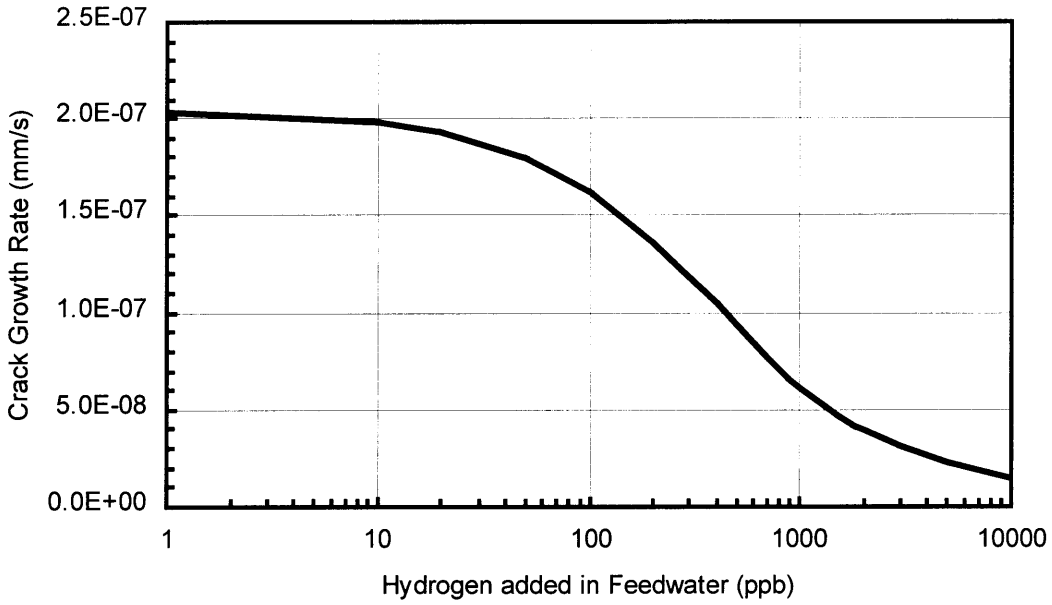

Figure 5.10. Crack growth rate (mm/s) as a function of feedwater hydrogen input for BWR type 3 reactor in the jet pump suction component.

Figure 5.10 shows the effect of hydrogen water chemistry on cracking in the jet pump suction. The reason that cracking is not suppressed by hydrogen additions of 1000 ppb and higher in the jet pump suction component is because the flow rate is extremely high. The electrochemical potential increases with flowrate. However, the correlation used is not valid for flow rates as high as those predicted in the jet pump suction. Therefore, it is likely that these crack growth rates are higher than those actually seen in the jet pump components.

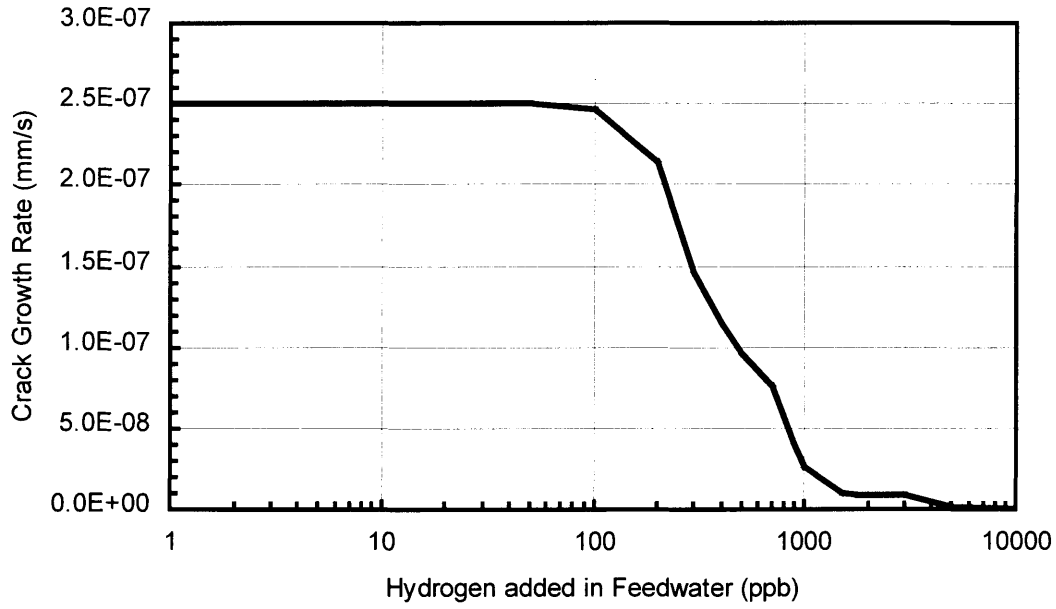

Figure 5.11. Crack growth rate (mm/s) as a function of feedwater hydrogen input for BWR type 3 reactor in the jet pump riser component.

Figure 5.11 plots the crack growth rate in the jet pump riser against the feedwater hydrogen content. In the jet pump riser, the crack growth rates are reduced 10^{-8} mm/s with 1800 ppb hydrogen in the feedwater and 10^{-9} mm/s with 5000 ppb hydrogen.

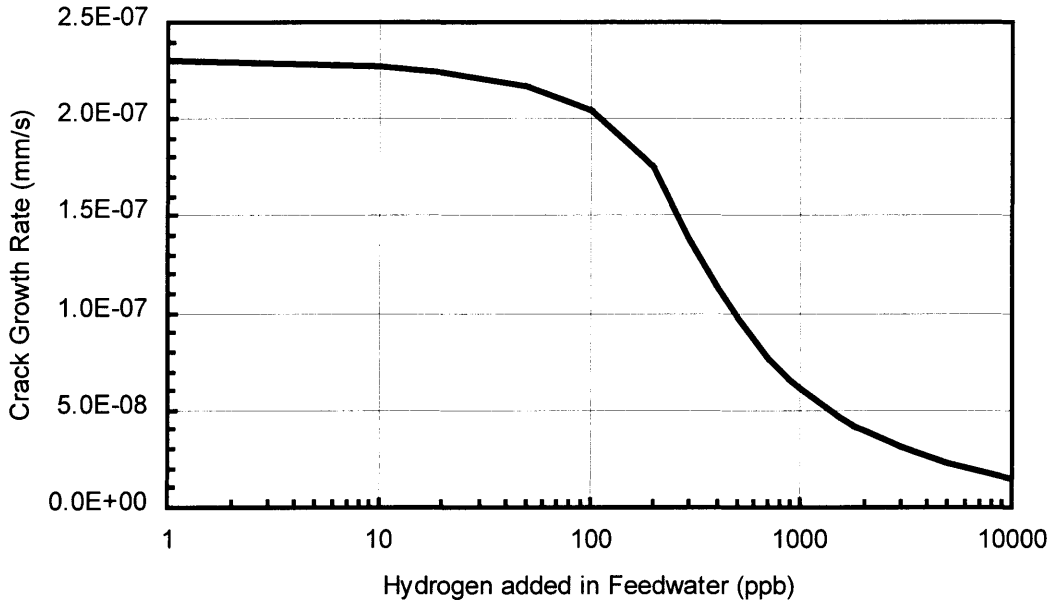

Figure 5.12. Crack growth rate (mm/s) as a function of feedwater hydrogen input for BWR type 3 reactor in the jet pump throat component.

Figure 5.12, indicates that hydrogen water chemistry is not highly effective in the jet pump throat. Like the jet pump suction, the jet pump throat has higher flow rates than are valid for the ECP correlation used in the model.

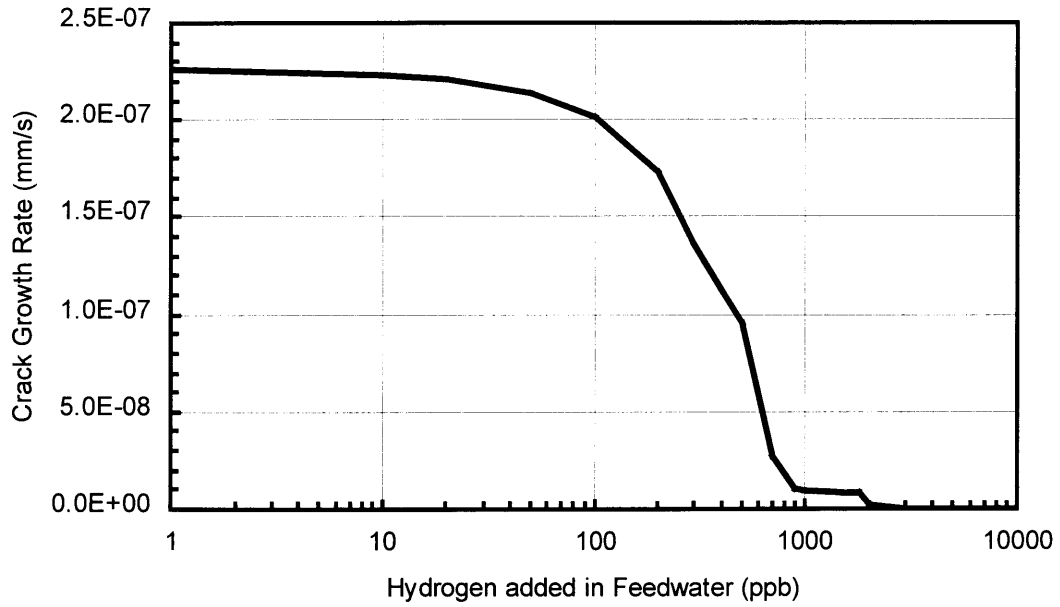

Figure 5.13. Crack growth rate (mm/s) as a function of feedwater hydrogen input for BWR type 3 reactor in the center of the jet pump diffuser component.

In the jet pump diffuser, the crack growth rates are reduced 10^{-8} mm/s with 1000 ppb hydrogen in the feedwater and 10^{-9} mm/s with 2000 ppb hydrogen. Figure 5.13, plot represents a reasonable appraisal of the effect of hydrogen water chemistry on cracking in the jet pump recirculation system, because the flow rates in the diffuser are closer to those for which the ECP correlation is highly accurate. The cracking rates at the bottom of the downcomer region indicate the predicted rates of cracking on the outside of the jet pump components. Two plots have been made for the bottom of the downcomer, one close to the core shroud and one close to the pressure vessel.

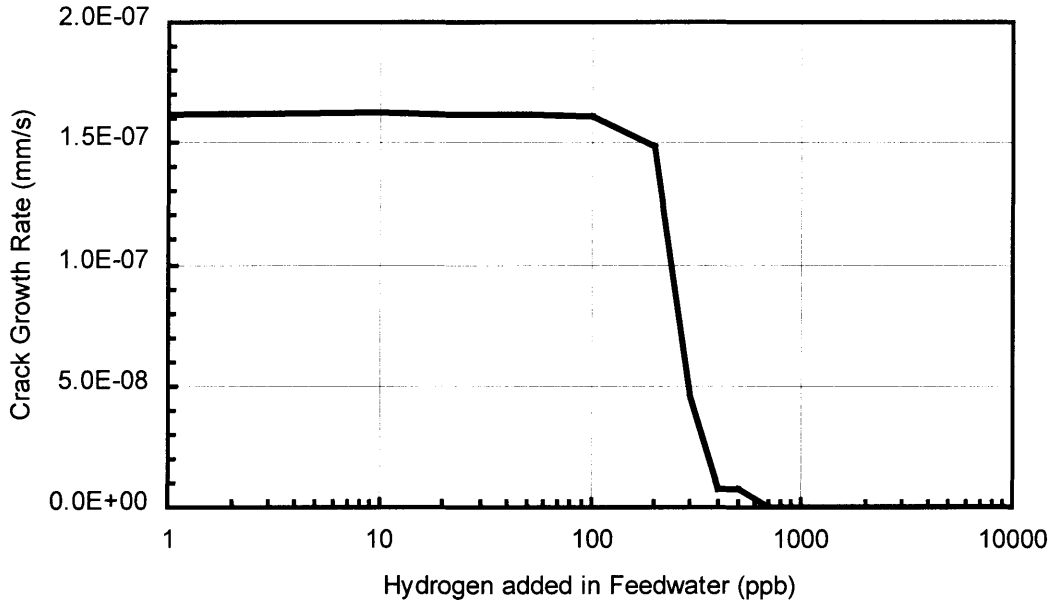

Figure 5.14. Crack growth rate (mm/s) as a function of feedwater hydrogen input for BWR type 3 reactor at the bottom of the downcomer close to the core shroud.

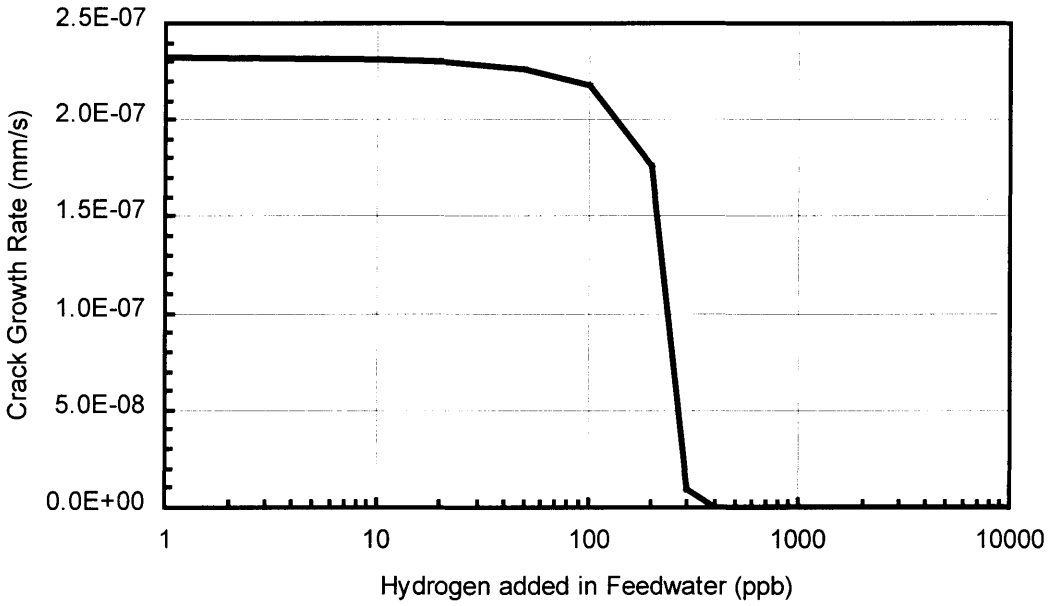

Figure 5.15. Crack growth rate (mm/s) as a function of feedwater hydrogen input for BWR type 3 reactor at the bottom of the downcomer close to the pressure vessel.

Figure 5.14 and Figure 5.15 are plots of the crack growth rate versus hydrogen water chemistry at the bottom of the downcomer. Close to the core shroud, at the bottom of the downcomer, the crack growth rates are reduced 10^{-8} mm/s with 400 ppb hydrogen in the feedwater and 10^{-9} mm/s with 700 ppb hydrogen. At the outer slice of the downcomer near the pressure vessel, the crack growth rate drops below 10^{-9} mm/s at 400 ppb hydrogen. These plots indicate that hydrogen injection effectively mitigates cracking in the downcomer.

An area were hydrogen water chemistry is less affective is above the core. Following passage through the core boiling region of the reactor, the hydrogen concentration is reduced. As the coolant is boiled, the dissolved hydrogen gas passes into the steam and is carried out of the pressure vessel.

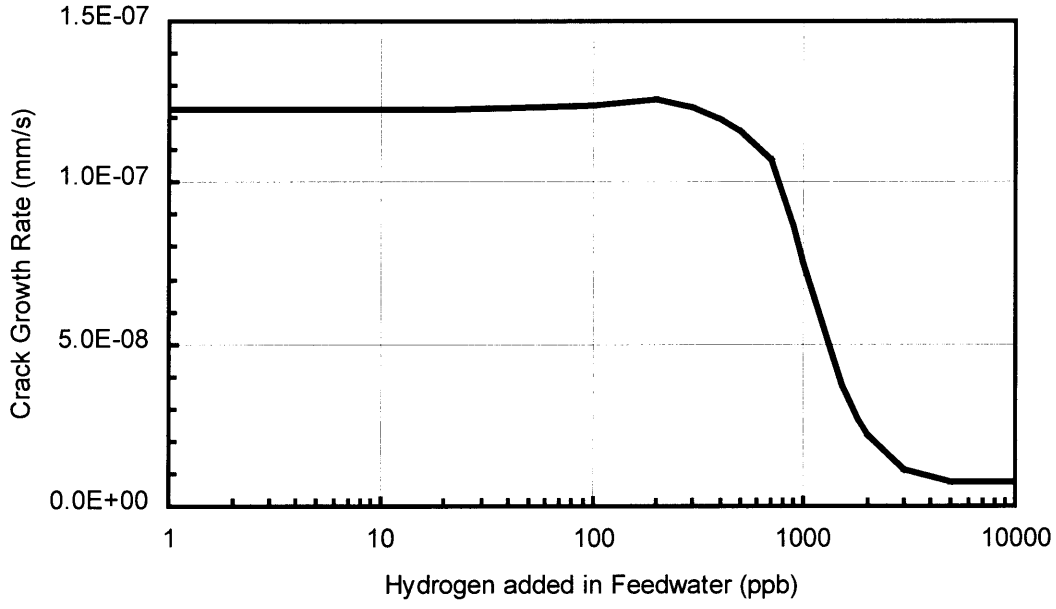

Figure 5.16. Crack growth rate (mm/s) as a function of feedwater hydrogen input for BWR type 3 reactor at the bottom of the upper plenum where the water is exiting the reactor core.

Figure 5.16, indicates the effectiveness of hydrogen water chemistry at the top of the core. At 5000 ppb hydrogen injection, the crack growth rate falls to 10^{-8} mm/s. The effect of hydrogen being carried away by the boiling water is more pronounced at the top of the core boiling region

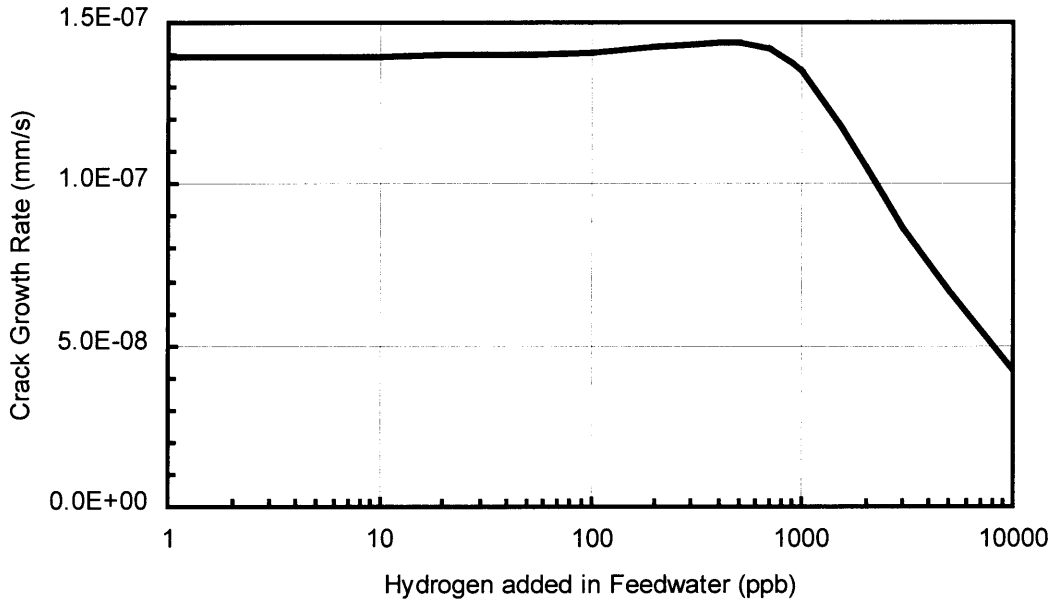

Figure 5.17. Crack growth rate (mm/s) as a function of feedwater hydrogen input for BWR type 3 reactor at the top of the of core boiling component.

Figure 5.17 indicates that the cracking is not mitigated even at 10000 ppb hydrogen injection at the top of the core. This plot indicates cracking rates at the top node of the core boiling region as modeled in the BWR simulation. This plot is based on separating the core into concentric zones, such that boiling occurs only in the center zone. Mixing between these zones in ignored. Therefore, a great deal of boiling has occurred leading to the ineffectiveness of the hydrogen water chemistry. This is the worst case scenario, likely to be seen only near the top and center of the core. In this region of the reactor an aggressive environment cannot be completely mitigated. Additionally, high

fluxes are likely to result in radiation induced segregation causing materials to become susceptible to cracking even if they were not put into service in such a condition. Therefore, in order to prevent cracking of materials within the core, the tensile stresses must be minimized.

5.3. Effect of Age on Cracking Susceptibility

In this section, the metal is considered to begin its life in the annealed condition without thermal sensitization. Because of the high flux rates, the top of the core is an ideal place to look at the effect of age on cracking susceptibility. Figure 5.18, demonstrates the effect of plant age on susceptibility to stress corrosion cracking. It is clear from the figure that the material is not sensitized for the first ten years. The slight decline in the crack growth rates is due to the reduction of the strain hardening exponent due to radiation hardening. Beyond 35 years of service, the crack growth rate is level. This is because while the EPR number is increasing beyond 30 C/cm^2, the susceptibility to cracking increases only slightly.

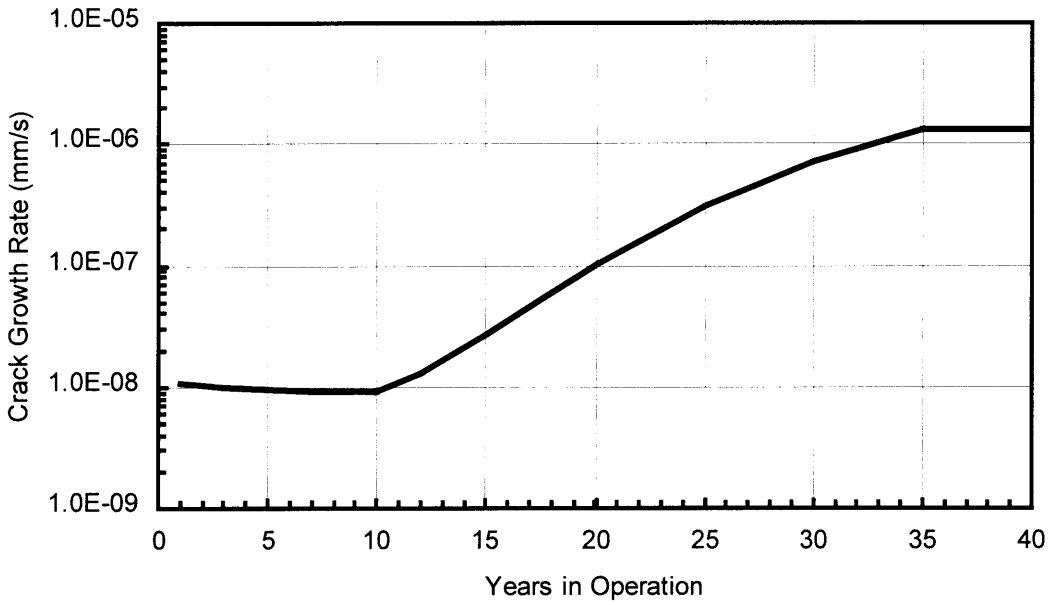

Figure 5.18. Crack growth rate (mm/s) as a function of reactor age for BWR type 3 reactor at the bottom of the upper plenum where the water is exiting the reactor core.

The maximum flux in a BWR is equivalent to 0.1 dpa per year. At this flux susceptibility to cracking can be seen as early as 2 years into the life of the reactor.

5.4. Future Work

While the modeling of nickel based alloys has not been discussed in detail in this thesis, most components of the IEDM have already been implemented with nickel in mind. In order to completely model IASCC in nickel based alloys such as Inconel 600/182, a correlation between the chromium profile determined by the RIS model and the EPR value would have to be developed. Additionally, current decay curve measurements would have to be made to create a nickel based current decay curve correlation. The development of these two correlations requires a large set of experiments which are not found in the current literature. However, if an equivalent EPR can be determined which acts like the EPR value for austenitic stainless steel when used

in the current decay curve correlation, then this EPR can validate that correlation. Put differently, if the current decay curve shape, the ECP, and the conductivity are all known, then an EPR can be backed out of the current decay curve correlation. This EPR can then be used with reasonable accuracy for a range of conductivity and ECP values to determine crack growth rates of nickel based alloys. This method could greatly reduce the battery of experiments necessary to analyze the crack growth rates of nickel based alloys.

6. Conclusions

The development of the IEDM has created the most deterministic and complete crack growth model to date. By starting with an expression for strain near the crack that has been shown to be highly accurate, the crack growth model correctly predicts the crack tip strain rate. This crack tip strain rate relationship includes the effect of crack growth and changing stress intensity factor. Additionally, the Young's modulus, the yield strength, and the strain hardening exponent are accounted for explicitly.

To complete the crack growth model, the crack tip strain rate relationship is combined with a complete derivation of the slip dissolution/film rupture model. This expression was derived in such a manner that the only assumption that is made is that the crack growth rate is not so fast as to negate the electrochemical effects of cracking. Also, a term is added which can account for the effect of hydrogen embrittlement. However, this work focuses on stainless steels for which hydrogen embrittlement is not a significant issue. The slip dissolution/film rupture model accounts for the repeated rupture of the passive film at the crack tip due to the crack tip strain rate. Following each rupture event, corrosion of the underlying metal matrix occurs with current decreasing exponentially along the current decay curve. The current is equated with a crack growth rate using Faraday's law.

An integrated model, the IEDM, was developed around the crack growth model to provide all the models and correlations needed to completely characterize the behavior of IASCC. Short-term effects of radiation dose on cracking are caused by interaction of the radiation with the coolant. When water is irradiated, the water molecule is destroyed

resulting in unstable radicals. These radiolysis products form oxygen, hydrogen peroxide, and hydrogen. The production of oxygen and hydrogen peroxide can increase the electrochemical potential of the water. Additionally, some of the radiolysis products are ions that contribute to the electrical conductivity of the water. The input to the crack growth model that is effected by ECP and conductivity is the current decay curve. Higher conductivity and ECP result in higher corrosion current following rupture of the passive film at the crack tip.

In order to determine the concentration of radiolysis products, a model for the chemistry of an irradiated coolant loop has been integrated into the IEDM. The MIT Radiation Chemistry Analysis Loop (RadiCAL) model requires the plant dimensions, power level, flowrate, and gamma and neutron fluxes as inputs. To allow the ECP and conductivity to be determined directly, chemical reaction parameters are used to completely characterize the chemistry of the reactor coolant. These parameters include reaction rates, activation energies and production rates from the interaction of radiation with water.

In addition to short term effects of radiation on the coolant, long term effects of radiation are seen in the metal. The long term effects of neutron irradiation include hardening and radiation induced segregation. As neutron fluence accumulates, the yield strength of the material is increased due to the build-up of dislocation loops. Along with the increase in yield strength, a decrease occurs in the strain hardening exponent. The rising yield stress and decreasing strain hardening exponent offset one another and therefore hardening has little effect on crack growth rate. An empirical model has been

developed to provide the yield strength and strain hardening exponent to the crack growth model.

The other long term effect, radiation induced segregation, leads to increased susceptibility to cracking along the grain boundary of the metal. RIS begins to contribute to cracking after several years of accumulated fluence when grain boundary chromium levels have been sufficiently decreased. As the grain boundary chromium concentration is further depressed the crack growth rate increases. The IEDM indicates that the increase in crack susceptibility due to RIS does not increase directly with fluence. Cracking susceptibility actually increases with time and to a lesser extent with flux. Therefore, a specimen irradiated to one dpa in one year (1 dpa per year) will be less susceptible to cracking than one irradiated to one dpa in 20 years (0.05 dpa per year).

In order for the crack growth model to utilize information about cracking susceptibility due to radiation induced segregation, the current decay curve must be altered based on the degree of sensitization. A model is used to determine the evolution of the grain boundary chromium concentration profile with time. This profile is then used to compute a volume depletion parameter representing the area of the profile cross section below 14% chromium. An expression has been determined from cracking susceptibility data to convert the volume depletion parameter into an equivalent value for the electrochemical potentiokinetic reaction. The EPR value is then used to determine the shape of the current decay curve that is used by the slip dissolution/film rupture model to determine the rate of crack growth.

An integrated model has been developed to evaluate the effect of reactor flux, fluence, and other operating conditions on crack growth rates in austenitic stainless steels

in boiling water reactor (BWR) environments. The following are the contributions made here and described in this thesis.

- A fully integrated crack growth model which incorporates the effects of irradiation on the physical and chemical properties of both the metal and reactor coolant.
- Accounting for both anodic and cathodic crack tip processes.
- A radiation hardening model for predicting the long-term effect of radiation on performance of austenitic alloys.
- A correlation between the grain boundary chromium profile and the equivalent EPR value for which the cracking susceptibility is equal to a degree of thermal sensitization.
- Use of a complete deterministic derivation of the slip dissolution/ film rupture model originally developed by Ford and Andresen [1.7, 1.13].
- A Visual Basic graphical user interface.